Volume X

May 2021

# JUCER

Journal of Undergraduate Chemical Engineering Research

Chemical & Molecular Engineering

AT STONY BROOK UNIVERSITY

Stony Brook University

Journal of Undergraduate Chemical Engineering Research
(JUCER)
https://you.stonybrook.edu/jucer
Stony Brook University
Department of Materials Science and Chemical Engineering
Engineering 208
Stony Brook, NY 11794
Phone: (631) 632-6269
Miriam.rafailovich@stonybrook.edu

We would like to thank Dr. Wilson Lee (Estee Lauder Co.) for mentoring and support.

JUCER is an annual publication by the Chemical and Molecular Engineering Program at the State University of New York at Stony Brook.

ISSN: 2373-4221

Author Inquiries:
For inquiries relating to the submission of articles, please contact Miriam Rafailovich (Miriam.rafailovich@stonybrook.edu)

JUCER
Journal of Undergraduate Chemical Engineering Research

## Staff

### Editor-in-Chief

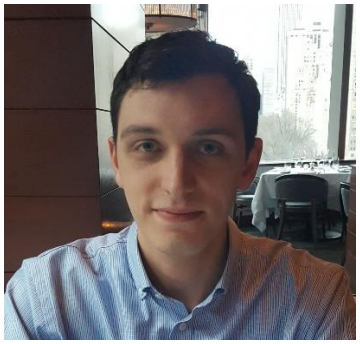

### Nathan Aragon

Nathan Aragon is a senior majoring in Chemical & Molecular Engineering. Nathan is an intern at Koehler Instrument Company, Inc., a mentor in the CEAS Peer Mentoring Program, and a former co-captain of the Stony Brook ChemE Car team.

### Advisors

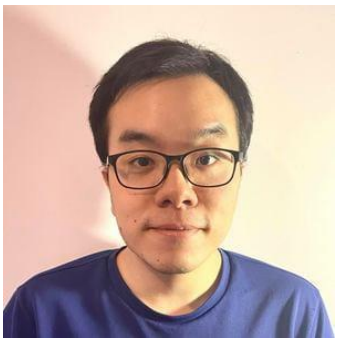

**Yu-Chung Lin**

Graduate Advisor

**Miriam Rafailovich**

Faculty Advisor

**Jessica Hofflich**

Graduate Advisor

JUCER
Journal of Undergraduate Chemical Engineering Research

## A Letter from the Editor-in-Chief

I am very happy to present Volume X of the Journal of Undergraduate Chemical Engineering Research (JUCER), which is a peer-reviewed journal that has been published annually by the Department of Chemical and Molecular Engineering since May 2012. The journal is created to highlight the research efforts of the graduating class in the Chemical and Molecular Engineering program. The current volume includes original research papers from eight different groups among the graduating class.

At the beginning of the senior year, each group chooses an advisor among the faculty of the Chemical Engineering department and pursues a topic that is under investigation by their advisor. In the first semester, each group generates a hypothesis regarding their topic and must defend their thesis proposal in front of a panel of experts, consisting of faculty members and advisors from the Chemical Engineering department. During the second semester, each group conducts research to attempt to confirm their hypothesis and writes a paper to discuss all of their findings. The papers go through a peer-review process where they are reviewed by experts in the field in order to uphold the high-quality standard of the JUCER publication. All of the papers in this publication include original findings from each group, which helps to provide a new and exciting perspective on each topic that is presented. The most exciting thing about senior research is that it is the culmination of all the hard work completed by the members of the graduating class over the last four years and as such, the class puts all of their acquired research and writing skills to the test. I believe the class has done a tremendous job this year and I am very proud to help put together something that all members of the class can take with them as they move on to the next chapter of their lives.

In conclusion, I would like to thank all of the expert reviewers for contributing to the quality of the work published in this volume of JUCER. I would also like to thank our faculty advisor, Dr. Miriam Rafailovich, and our graduate advisors, Jessica Hofflich and Yu-Chung Lin, and the faculty advisors for each group for all of their guidance and support this past year. I also would like to wish every member of the graduating class best of luck in all future endeavors.

Sincerely,

Nathan Aragon

Editor-in-Chief, JUCER

## Table of Contents

# Exploring the applicability of aerogel and CPC in an integrated spray for viral protection and N95 level protection while maintaining breathability of surgical masks

Yuya Baba[a], Rui Chen[a], Andrew Sutjahjo[a], James Yang[a]

[a]*Department of Materials Science and Chemical Engineering, Stony Brook University, Stony Brook, NY 11794, USA*

**Abstract**

The COVID-19 pandemic led to a significant increase in face coverings around the world. Surgical masks have been used widely due to their cost and availability. However, they have a lower filtration performance compared to an N95 respirator's performance. While N95 respirators have high performance, they have reduced breathability, making it harder for people to breath, especially those with respiratory problems. We propose a way for a surgical mask to have both the filtration capability and the protection of an N95 respirator while maintaining the mask's original breathability. We are utilizing a proprietary blend of an aerogel mixture provided by Estée Lauder Inc. As aerogels have pores on the scale of tens of nanometers, they are at a perfect porosity where they allow air to flow freely while acting as a barrier for larger particles such as the novel coronavirus. The aerogel samples were all sprayed onto the outer surfaces of masks. Cryo-scanning electron microscopy (SEM) images showed the porosity of K-1 and W-1 cast films to be between 10 nm and 50 nm in diameter. Air penetrability was tested using a gas permeability instrument containing pressurized air and results showed no discernable difference between the permeability of the control group and the sprayed surgical masks. Tests using cetylpyridinium chloride (CPC) - a chemical compound known to have antiviral properties - integrated mouthwash spray resulted in four orders of magnitude decrease in H1N1 viral concentration, but a deeper penetration of the viral particle than as compared to a control sample. The results indicate a strong possibility for a surgical mask that will have improved filtration performance, while maintaining air flow performance.

*Keywords*: aerogel, COVID-19, CPC, surgical masks, breathability, permeability, filtration, antiviral, N95 respirator

## 1. Introduction

Since the beginning of the COVID-19 pandemic in March 2020, the usage of face coverings has risen exponentially. The SARS-CoV-2 virus is known to spread easily through inhalation of the aerosols, physical contact of contaminated surfaces, or direct deposition of emitted droplets on mucosal surfaces such as the eyes and mouth[1]. To fight this pandemic, many health experts have suggested everyone to wear masks and to practice hand hygiene to mitigate disease transmission[2]. A plethora of research has indicated that masks can help protect individuals from contacting the virus. Wearing masks also prevents infected individuals from transmitting the virus to others around them. Due to their cost and availability, surgical masks have been widely used around the world. These masks have become a standard for daily life and are pivotal for fighting against the pandemic.

While the majority have turned to surgical masks, others went to alternatives such as homemade cloth masks, or N95 respirators. Per Occupational Safety and Health Administration (OSHA) protocol, N95

respirators clear the required 95% filtration performance[3], however, the FDA has warned against the use of N95 respirators for people with respiratory problems because of its limited airflow. The higher the filtration performance, the poorer the breathability. While surgical masks are adequate in day-to-day life, they do not protect against prolonged close contact with someone who is infectious, especially indoors. Furthermore, trapped viral particles can still be dangerous as they can be easily transmitted from the surface of the mask to a person's nose when the mask is touched. Therefore, we hypothesized that the integration of aerogel with CPC - a chemical known to have antiviral properties[4] - will be able to solve both of the aforementioned problems.

Aerogels have been found to have extremely small pore sizes on the scale of 20 nm with low densities[5]. At this scale, these aerogels will be able to perfectly allow oxygen gas through to ensure breathability while keeping out the average aerosol particles that are on the scale of micrometers[6]. We decided to explore CPC and its possibilities in virucidal potentials on a mask surface since they are both effective at killing viruses and nontoxic to the human body for concentrations up 1,000 μg/mL, or less than 0.1%[7]. The usage of aerogels will be able to prevent penetration of unwanted particles while eliminating residual harmful viruses on the surface.

## 2. Materials & Methods

### *2.1 Materials*

Standard surgical masks were mainly used during the experiments. W-1 and K-1 aerogel solutions, which are proprietary solutions, were provided by Estée Lauder Inc.

**Figure 1.** Type II-R CE/FDA approved surgical mask.

### *2.2 Sample Preparation*

The aerogel samples were sprayed from directly above the masks and covered the entire surface. They were air dried in a well-ventilated area for at least 48 hours before being tested and analyzed.

### *2.3 FTIR Data*

FTIR spectrum data were collected using the Nicolet iS50 FTIR spectrometer.

### *2.4 SEM and Confocal Microscopy*

The SEM and confocal microscope were used to understand and analyze the properties of the masks and aerogels on a microscopic level. Samples of the masks were cut to desired sizes using scissors. All SEM images were taken at the ThINC lab at Stony Brook University.

### *2.5 Permeability of Samples*

The permeability of the samples was determined using the gas permeability instrument CSI-135 made by CSI instruments (figure 2). Samples were cut into 51 mm diameter shapes to fit the instrument. With compressed air constantly flowing, the pressure difference was determined by measuring the change in height of methyl ethyl ketone (MEK) fluid rising in a capillary tube.

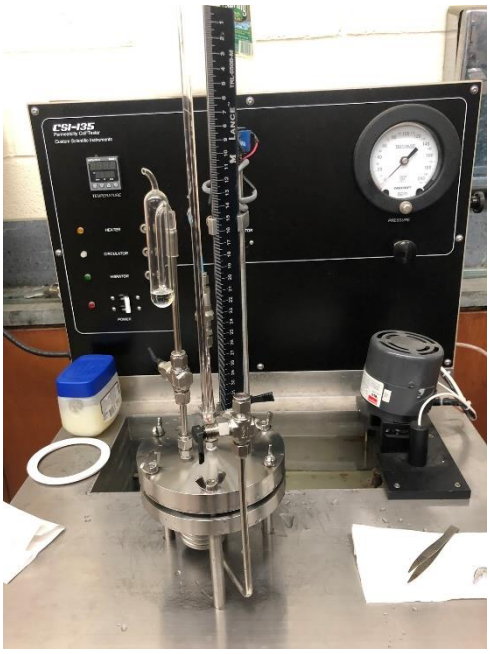


**Figure 2.** Gas permeability instrument CSI-135.

*2.6 Atmospheric Particle Counting*

The condensation particle counter CL 3775 by TSI measured the filtration efficiency of air particles roughly 10-500 µm in diameter through samples. Samples were cut into approximately 20 mm and 40 mm diameter shapes to fit the instrument. Atmospheric air was used for all the tests and tests ran for a total of four minutes.

*2.7 Antiviral Property testing*

*2.7.1 Cell Cultures*

Madin-Darby canine kidney cells (MDCK-2) from the American Type Culture Collection (ATCC CRL-2936) were cultured and grown in OptiPRO™ SFM from Gibco of Thermal Scientific with 1x Glutamax (Gibco), 100 units/ml penicillin, and 100 µg/ml streptomycin. H1N1 PR8 (ATCC VR-95) viruses were cultured in MEM (Gibco) with 0.2% BSA from Sigma Aldrich.

*2.7.2 Virus Infection*

50 µL of the virus solution was put on the mask surface for 45 mins and left to dry at 25°C. Samples were separated to different layers, and the viruses were collected by vortexing each sample with a 5 mL medium. 250 µL of virus solution was added into each well after serial dilution. The well plates were placed on the rocker for 30 mins at room temperature. After rocking, the well plates were placed into an incubator at 37°C and 5% $CO_2$ for 1 hour. The virus solution was replaced with MEM medium with 0.3% tragacanth gum (Sigma) and 0.2% BSA. After 4-day incubation at 33°C and 5% $CO_2$, the samples were stained with 1% crystal violet (Sigma).

*2.8 Contact Angle*

The goniometer KSV CAM 200 Optical Contact Angle Meter was used to measure the contact angle of water droplets on mask surfaces. A sample was taped down to make the surface as flat and level with the platform as possible. A 7 µL droplet of water was placed on the sample, and the computer program, KSV CAM 200, calculated the contact angle which was recorded every 5 min.

*2.9 Aerogel Films*

Cast films of Wilsonite were made by taping a sheet of teflon film on the bottom of a petri dish and pouring the aerogel solution on top. The petri dish was then left on a flat surface in an oven at around 60°F to 70°F for 3 days to dry. A razor blade was used to cut out the cast film out of the petri dish.

## 3. Results & Discussion

*3.1 Material Properties*

Contact angles of water on the mask surfaces and Fourier-Transform Infrared Spectroscopy (FTIR) data were recorded to determine its hydrophobicity and material composition, respectively. Generally, a contact angle less than 90° indicates hydrophilic while anything greater than 90° is considered hydrophobic[8]. Hydrophobicity of the mask is important as otherwise the liquid aerosol particles exhaled from the nose can potentially pass through the filtration layers. As it can be seen in figure 3, the contact angle remained quite consistent over a period of 15 minutes, beginning at approximately 120° and reaching 115° by the end of the test. Since the angle stayed above 90°, it is clear that the mask surface is hydrophobic. The slight decrease in contact angle was most likely due to evaporation of the droplet. Tests done longer than 15 minutes showed a much

sharper decrease in contact angle due to increased evaporation.

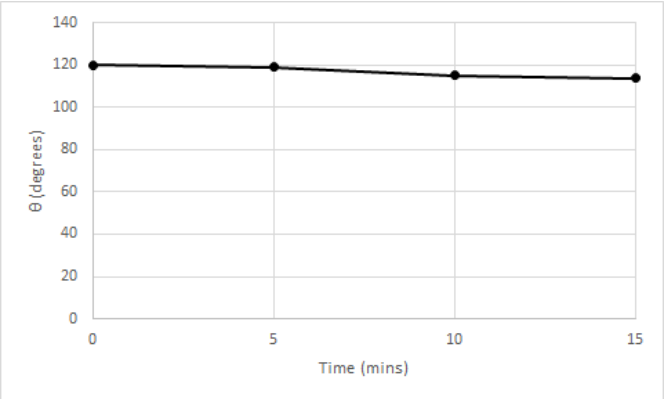


**Figure 3.** Contact angle of water droplet on surgical mask outer layer over 15 minutes.

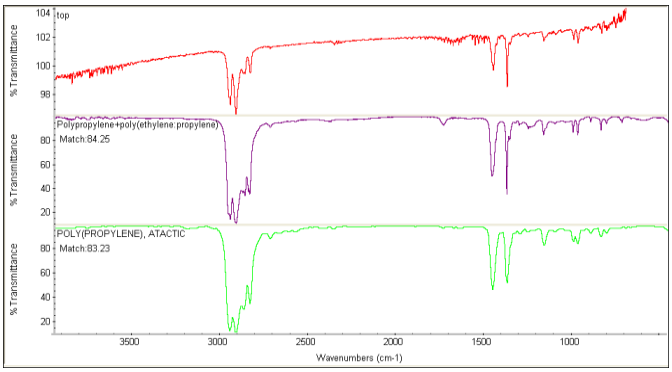


**Figure 4**. FTIR result of the outer layer (red) of the surgical mask matched with database results (purple and green).

Based on the FTIR analysis in figure 4, the outer layer of the surgical mask is composed mainly of polypropylene, which is supported by the contact angle results, and vice versa, as polypropylene is a known hydrophobic material[9]. Analysis (not shown) was also conducted on the middle and inner layer of the mask. The analysis was nearly identical, indicating polypropylene in all three layers.

*3.2 Breathability*

*3.2.1 Porosity and Coated Surface*

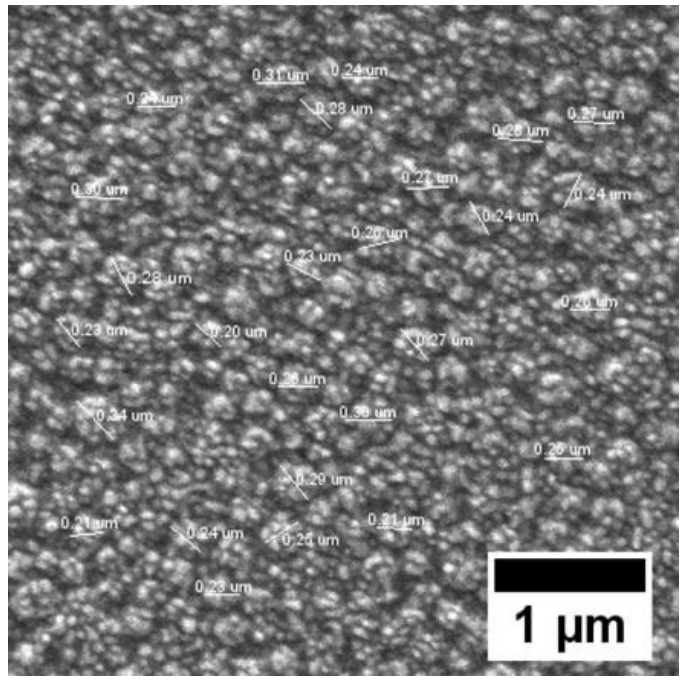


**Figure 5.** Cryo-SEM image of W-1 cast film, the black spots indicating pores on the scale of 10-50 nm (white scales on the congregation of particles indicate their diameter).

Figure 5 shows the cryo-SEM of a W-1 film with a scale bar of 1 µm. The dark areas near the congregations of aerogel particles are nanopores ranging from 10-50 nms. At this size, the pores are capable of letting through air molecules while filtering out viruses. In addition to the material's porosity, the samples also formed a cohesive layer on the first layer of the surgical masks, as shown in figure 6. The sprayed samples (figure 6a) show a properly coated surface with a smooth, non porous surface. Compared to figure 6b, which was before W-1 was sprayed on, the diameter of the crevices is approximately 80 µm, allowing smaller particles, such as aerosols, to flow past the fibers. A study had shown that normal respiratory activities such as breathing produced aerosols smaller than 0.8 µm in diameter while speaking produced aerosols between 3.5 and 5 µm in diameter. While there were variations in the range of particle size - from as low as 0.3 µm to upwards of 20 µm (from activities such as coughing)[6] - they were still smaller than the average diameter of the holes in the fibers.

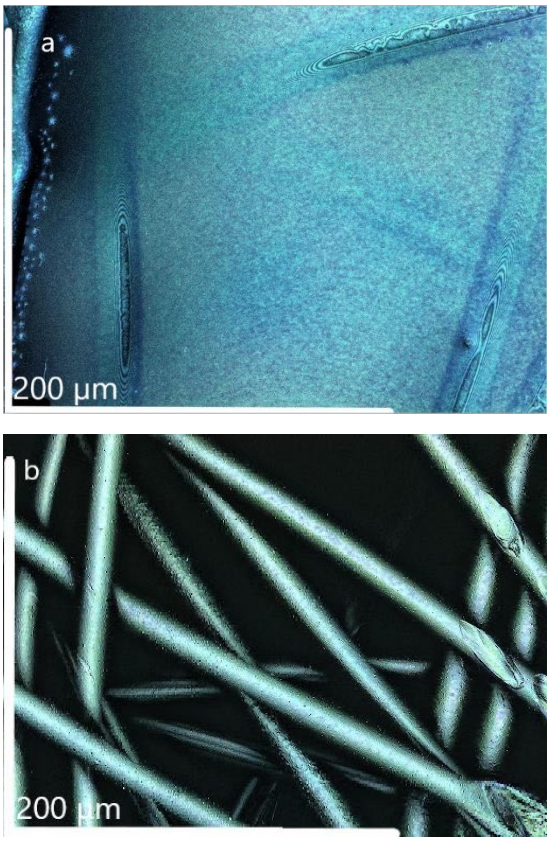


**Figure 6.** Laser confocal image of outer layer of surgical mask with (a) and without (b) W-1 coating.

*3.2.2 Air penetrability*

Data from the CSI-135 instrument showed that there were no discernible differences in the air permeability of surgical masks and a mask with the aerogels sprayed on. Unfortunately, numerical data is not available due to the speed in which the MEK fluid rose in the capillary. Comparing the speeds in which the fluid rose shows that even with the aerogels sprayed on the outer layer of the surgical masks, it does not diminish airflow. These sprayed masks were also personally tested and worn for a period of time, ensuring their breathability. The air permeability of the W-1 cast film was also measured and showed similar results. The W-1 cast film was examined before and after testing to make sure there were not any cuts or punctures that would have affected the results of testing.

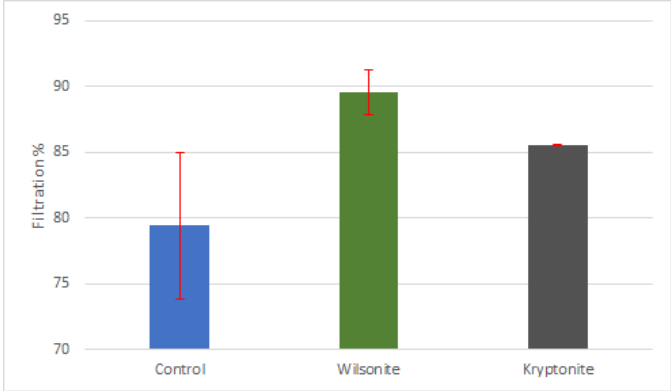


**Figure 7.** Average particle counting filtration efficiency comparison between unsprayed, W-1-sprayed, and K-1-sprayed surgical masks. Error bars indicate a 95% confidence interval.

Particle counting results showed a more detailed result. In figure 7, there are noticeable differences between the unsprayed, W-1 sprayed, and K-1 sprayed surgical masks. The control group had many variations between different samples due to batch-to-batch variations and even within the same batch. The unsprayed surgical average mask filtration efficiency was determined to be 79.41 ± 5.60%, with a 95% confidence interval. In comparison, W-1 and K-1 sprayed had an 89.56 ± 1.74% and 85.51 ± 0.05% filtration efficiency, respectively. Surfaces sprayed with K-1 had the most consistency in terms of percent filtered, but the W-1 sprayed mask showed the best filtration effectiveness overall. These results indicate that the aerogel sprays do indeed improve the filtration efficiency of surgical masks up to the N95 level.

*3.3 Antiviral Property*

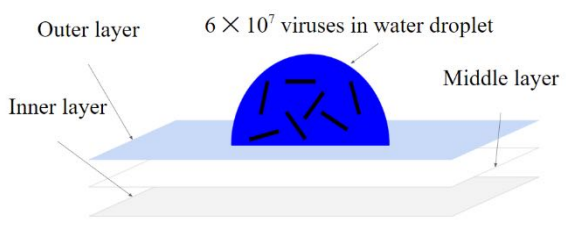


**Figure 8.** Schematic diagram of H1N1 viral droplet on outer layer of surgical mask. Droplet was allowed to rest on the surface for 15 minutes before penetration data was collected and measured.

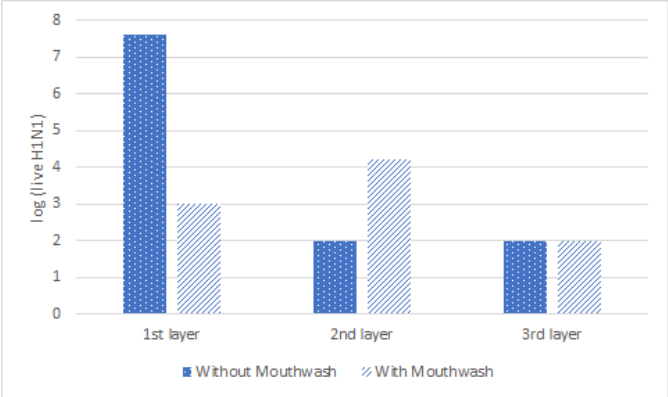


**Figure 9.** Collected data of live H1N1 viral counts after 15 minutes. Viral counts on all three surfaces were recorded with and without mouthwash containing CPC (MCC).

In figure 8, a droplet of water containing about 6 x $10^7$ H1N1 viruses was placed on the outer layer of a surgical mask and observed for 15 minutes in a BSL-2 enclosure. After 15 minutes, the viral load was measured on each layer of the mask and displayed in figure 9. This experiment was done without CPC and with 0.085% CPC. Without MCC, most of the virus stayed alive on the first layer and the viral particles did not penetrate through to the second and third layer. Since the viruses were coated in a water solution and the masks are hydrophobic, the viral particles were trapped on the surface along with the water droplet. With MCC, a majority of the virus died, but the virus did penetrate to the second layer, which contained the highest concentration of virus. However, the third layer saw no difference between the two groups in viral concentration. Overall, the MCC caused the H1N1 viral concentration to be reduced by almost 4 logs.

The contact angle of water with MCC sprayed mask surface is shown in figure 10. The contact angle was at 60° during initial measurement and quickly decreased to almost 40° after just 10 minutes. While evaporation may have played a part in this result, the initial contact angle was already lower than 90 degrees, confirming that the mask is hydrophilic. The MCC contains surfactants and that is what we believe to be the main cause of this change to hydrophobicity. The surfactants are most likely used to ensure a homogeneous mixture of CPC within the mouthwash solution. Although the surfactants allowed the penetration of the viral particles into the second layer, the benefits of the CPC cannot be ignored.

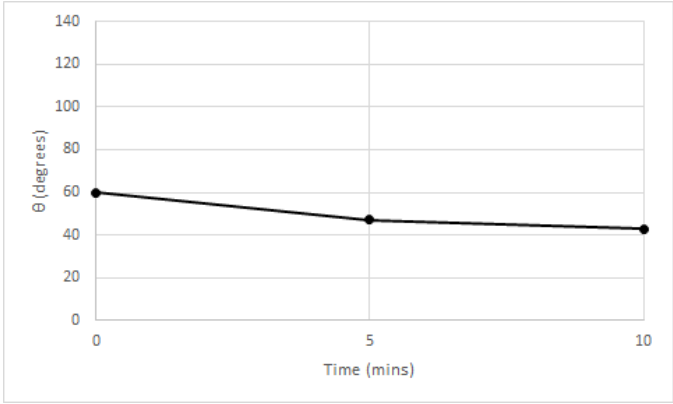


**Figure 10.** Contact angle of water droplet on surgical mask outer layer sprayed with MCC over 10 minutes.

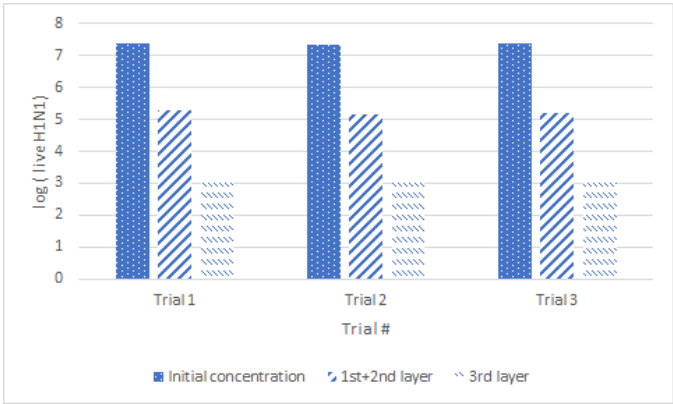


**Figure 11.** Collected data of live H1N1 viral counts after 15 minutes. Surfaces were sprayed with a 0.05% concentration CPC-W-1 mixture.

Another antiviral test was performed with a CPC-W-1 mixture, resulting in a 0.05% concentration of CPC within the solution. This solution was sprayed onto three surgical masks and the results are shown in figure 11. The number of surviving H1N1 viruses have gone up from the previous test, with only a 2-log reduction in viral activity. This result could be due to either the decrease in CPC concentration, the nonuniform distribution of CPC within the solution, or a combination of both. When observing the mixture using the naked eye, clumps of CPC could be observed on the walls of the container, suggesting that certain areas on the mask had higher concentrations of CPC than others.

## 4. Conclusion

These observations demonstrate that the aerogels provided by Estée Lauder can provide a mask that is comparable to an N95 respirator. The gas permeability instrument and particle counter indicate that the breathability of the mask is not compromised by the aerogel. The difference in permeability is not noticeable and the breathability can be considered the same. With the results of the H1N1 experiment, CPC can be used to kill viruses and provide better filtration efficiencies compared to a standard surgical mask.

But due to the effect of surfactants and its effects on decreasing viral filtration efficacy, a proper way to incorporate CPC onto the masks needs to be addressed. Future work includes exploring micro-emulsion technology to load CPC directly into the aerogel, allowing proper mixing and uniform distribution of CPC once sprayed on surgical masks. Through this, we hope to create a proper mixture that can provide both efficient filtration and antiviral properties through effective distribution of the CPC molecules.

## 5. Acknowledgements

We would like to thank Dr. Wilson Lee (Estée Lauder Companies Inc.) for providing us with the aerogel samples, Yiwei Fang for assistance with contact angle and air permeability testing, Dr. Kuan-Che Feng (SBU-CME) for performing the H1N1 assays and antiviral tests, Dr. Daniel Knopf (SBU--Atmospheric Sciences & Chemistry) for assisting us in particle counting tests, Dr. Chung-Chue Chang (SBU-AEC-ThINC) for assistance in taking SEM images, and Aya Sabbah (SBU-SDM-Prosthodontics and Digital Technology) for assistance with laser confocal microscopy. We would also like to mention that this project has been supported with the funding from the SUNY Prepare Innovation and Internship Program Award.

## 6. References

1. Jones, R. M. & Brosseau, L. M. Aerosol transmission of infectious disease. *J. Occup. Environ. Med.* 57, 501–508 (2015).

2. MacIntyre, C. R. & Wang, Q. Physical distancing, face masks, and eye protection for prevention of COVID-19. *The Lancet* 20, 31183 (2020).

3. Qian Y, Willeke K, Grinshpun SA, Donnelly J, Coffey CC. Performance of N95 respirators: filtration efficiency for airborne microbial and inert particles. Am Ind Hyg Assoc J. 1998 Feb;59(2):128-32. doi: 10.1080/15428119891010389. PMID: 9487666.

4. Popkin, Daniel L., et al. "Cetylpyridinium Chloride (CPC) EXHIBITS Potent, RAPID Activity against Influenza Viruses in Vitro and in Vivo." *Pathogens and Immunity*, vol. 2, no. 2, 2017, p. 253., doi:10.20411/pai.v2i2.200.

5. Pan. Y, et al. J Sol-Gel Sci Technol., 2017, 82, 594

6. Morawska, L., et al. "Size Distribution and Sites of Origin of Droplets Expelled from the Human Respiratory Tract during Expiratory Activities." *Journal of Aerosol Science*, vol. 40, no. 3, Mar. 2009, pp. 256–269., doi:10.1016/j.jaerosci.2008.11.002.

7. Alvarez, D. M., Duarte, L. F., Corrales, N., Smith, P. C., & González, P. A. (2020). Cetylpyridinium chloride blocks herpes simplex virus replication in gingival fibroblasts. *Antiviral Research, 179*. doi:10.1016/j.antiviral.2020.104818

8. Law, K. (2014). Definitions for HYDROPHILICITY, Hydrophobicity, and SUPERHYDROPHOBICITY: Getting the basics right. *The Journal of Physical Chemistry Letters, 5*(4), 686-688. doi:10.1021/jz402762h

9. Belmonte, G. K., Charles, G., Strumia, M. C., & Weibel, D. E. (2016). Permanent hydrophilic modification of polypropylene and poly(vinyl alcohol) films by vacuum ultraviolet radiation. *Applied Surface Science, 382*, 93-100. doi:10.1016/j.apsusc.2016.04.091

# Evaluation of Hypochlorous Acid Fogging: An Alternative Disinfection Method

Jason Bocklage[a], Curtis Miller[a], Andrew Salerno[a], John Stocum[a]

[a] *Department of Materials Science and Chemical Engineering, Stony Brook University, Stony Brook, NY 11794, USA*

**Abstract**

The COVID-19 pandemic has led to increased demand for disinfectants to help reduce transmission of the novel virus. Hypochlorous acid (HOCl) has been studied as a liquid disinfectant in the past, but little research exists on its fogged or aerosolized application, which is the primary focus of this work. Three solutions were tested: one purchased commercial solution (EcoLogic Solutions) and two produced using home units (EcoloxTech Eco One and RIPPO Sprayer). Solution was fogged into a desiccator using a Contronics HU-45 Humidifier. Aluminum squares were coated with either 50 µL of *Enterococcus faecalis* (*E. faecalis*) or H1N1 influenza virus solution and oriented vertically in the desiccator. These pathogens, and how they responded to the fogging treatment when compared to a control group, which was left untreated (not fogged), formed the basis for the results and gave evidence as to whether or not the method was effective at disinfecting the surface. The research found that fogging continuously with the EcoLogic solution yielded log reductions in *E. faecalis* and H1N1 of 6.59 and 4.90, respectively, after 5 minutes. Fogging under the same conditions with solutions produced by the Eco One and RIPPO yielded log reductions in *E. faecalis* of 4.21 and 0.91, respectively. The Eco One solution required more time to yield a ≥3-log reduction (≥99.9% reduction) in H1N1 compared to the EcoLogic solution (7.5 min vs 5 min). The RIPPO solution was not effective in all scenarios. These results suggest that hypochlorous acid (purchased or homemade), when applied as a fog, is effective against certain bacterial and viral pathogens, namely *E. faecalis* and H1N1. However, several factors such as the time fogged and pH of the starting solution, which ultimately determines whether chlorine is present as HOCl or $OCl^-$, play a significant role in the level of effectiveness observed.

*Keywords:* COVID-19, disinfection, hypochlorous acid, fogging

## 1. Introduction

With the emergence of Coronavirus Disease 2019 (COVID-19), the demand for disinfectants has been on the rise, causing shortages in many places such as schools, hospitals, and businesses. This has sparked new research on the use of alternative disinfectants. Not only is it important for these disinfectants to be safe and effective, but it is also important for them to be inexpensive and easy to produce. Hypochlorous acid (HOCl) has gained much attention in this regard as it is a green, non-toxic, antibacterial, and antiviral disinfectant that can be produced cheaply from common household materials.

As early as March 2020, HOCl was approved by the Environmental Protection Agency (EPA) as a viable disinfectant in its liquid form on non-porous surfaces against COVID-19 [1]. HOCl has also been proven to be an effective disinfectant against a variety of other pathogens including those

that are known to cause foodborne illnesses like *Escherichia coli*, *Salmonella*, and *Listeria*, as well as viruses such as the human norovirus and avian influenza virus [2-4]. Being that COVID-19 is categorized as a highly infectious and Biosafety Level 3 (BSL-3) disease, access to it is limited and requires a high level of security clearance, which led the authors to instead study the notoriously hard-to-kill strain of bacteria *Enterococcus faecalis* (*E. faecalis*), and the H1N1 influenza virus. These pathogens were chosen because they do not require BSL-3 clearance yet are still very infectious and relevant today.

*E. faecalis* is a gram-positive bacterium that is resistant to many antibiotics and is one of the leading causes of urinary tract infections (UTIs) and infections following root canal procedures [5]. H1N1 influenza virus, on the other hand, is an airborne human respiratory virus and was responsible for the swine flu pandemic in 2009 [6]. The H1N1 influenza virus has a lipid envelope similar to SARS-CoV-2, which gives it some additional relevance to the current pandemic. These viruses both cause respiratory illnesses and transmit in similar ways. The main method of transmission is through exposure to respiratory fluids carrying infectious viral particles. There are three principal pathways in which this transmission can occur: inhalation of the virus, deposition of the virus on exposed mucous membranes such as the eyes, nose, and mouth, and touching mucous membranes with soiled hands contaminated with the virus [7,8]. The goal here is to prevent and help reduce the transmission of the virus via the hand-to-mucous membrane pathway by killing the virus at the source: a frequently-touched surface.

HOCl is a weak acid that is formed by adding chlorine to water. Due to chlorine's considerable solubility in water (7,300 ppm at 20°C and 1 atm), it dissolves easily when administered in controlled amounts [9]. Chlorine is a notorious oxidizing agent in chemical reactions due to its electronic structure. Elemental chlorine, like all halogens, has the tendency to acquire an extra electron from its surroundings to completely fill and stabilize its outer shell with eight electrons. When chlorine gas ($Cl_2$) is dissolved in water, it undergoes the following hydrolysis reaction:

$$Cl_2 + H_2O \rightleftharpoons HOCl + H^+ + Cl^- \quad (1)$$

This reaction has a very high ionization constant of $K=3.3 \times 10^{-8}$ at 20°C [9], and $Cl_2$ essentially fully hydrolyzes in a matter of seconds under standard conditions. Only if the pH of the water is below 3, or if chlorine concentration reaches very high levels (greater than 1,000 ppm), will there be any measurable quantity of $Cl_2$ present in solution [9]. Therefore, it is incorrect to simply refer to disinfection by chlorine, when it is the oxidizing capacity of the chlorine in the hydrolysis product HOCl that provides the major disinfecting action of chlorine solutions [9].

HOCl will undergo a further dissociation reaction in solution with water:

$$HOCl \rightleftharpoons H^+ + OCl^- \quad (2)$$

This process occurs essentially instantaneously and is reversible. One can describe the equilibrium relationship by deriving an expression for the ionization constant:

$$K=[H^+][OCl^-]/[HOCl] \quad (3)$$

which can be rearranged as follows to show that the relative amounts of HOCl and hypochlorite ion ($OCl^-$) present in a solution of "free chlorine" are a function of the hydrogen ion activity, or the pH of the solution [9]:

$$K/[H^+]=[OCl^-]/[HOCl] \quad (4)$$

It was these relations that were used to create and plot the curves shown in Figure 1.

Free available chlorine (FAC) refers to the chlorine present as either undissociated HOCl or $OCl^-$. Despite $OCl^-$ contributing to the total FAC

of a solution, it is a misrepresentation of the solution's overall disinfecting capabilities. Unlike the chlorine atom in a HOCl molecule, the chlorine atom in an $OCl^-$ molecule is tightly bound to the oxygen atom and does not dissociate easily, which is essential for disinfection. HOCl dominates at lower values of pH, while $OCl^-$ dominates at higher values of pH as shown in Figure 1. The level of FAC is highest in pH 5 solutions [10].

HOCl is a powerful oxidizing agent and is estimated to be 80 times more effective than bleach in surface disinfection [11]. It is important to point out that $OCl^-$ is the predominant chlorine species present in bleach. While bleach is a common household cleaner, it can be toxic to humans and has the potential to damage surfaces [12]. For this reason, when hypochlorous acid is made, it is crucial that its pH is in the slightly acidic range, between pH 4 and 6, where the solution is most stable and will best maintain its chlorine concentration and pH, and thus its disinfecting capabilities, over time [13].

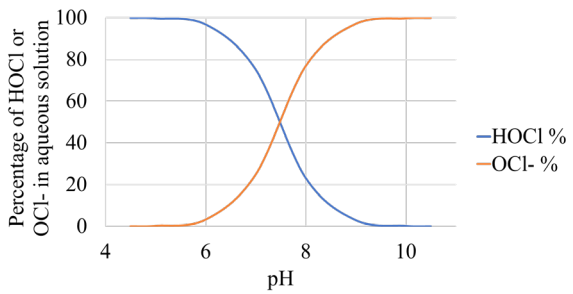


**Figure 1.** Effect of pH on the predominant chlorine species in aqueous solution. $pK_a = 7.5$.

Active chlorine species, like HOCl and $OCl^-$, contribute to the inactivation of microbial cells. However, the ways in which the microbial cells are inactivated are different between HOCl and ionized $OCl^-$, and this is due to the interaction with the chlorine species and the cell walls and membranes [2]. The microbial cells have a lipid bilayer, or a hydrophobic layer of the plasma membrane, and the interactions between the chlorine species and this bilayer explains the differences in the inactivation of the microbial cells. Due to the negative charge of the lipid bilayer, ionized $OCl^-$ is unable to penetrate the cell membrane of the microbial cells (Figure 2). So, $OCl^-$ is only able to act from outside the cell, by inactivating functional proteins that are in the plasma membrane. On the other hand, HOCl can penetrate the lipid bilayer since it is uncharged and has relatively smaller size, which allows it to inactivate microbial cells from inside the cell, by what is believed to be inhibition of enzymes essential for microbial growth as well as damage to the DNA [2]. A major reason why HOCl has better disinfection power compared to $OCl^-$ is because of the differences in where the inactivation of the microbial cells happens: HOCl can inactivate cells from inside the membrane, while $OCl^-$ is only able to inactivate cells from outside the cell.

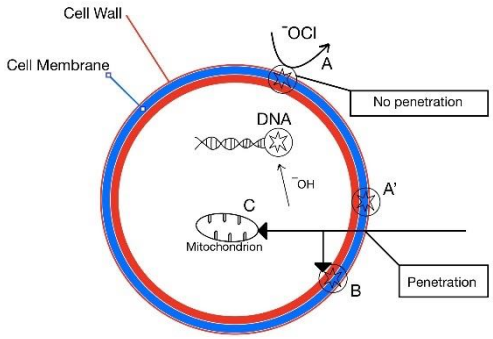


**Figure 2.** Mechanism of HOCl invasion of negatively-charged pathogen membranes [2].

Much of the previous research on HOCl as a disinfectant has focused on its liquid application, where the bacteria or virus is directly immersed in the solution. This research focuses on the fogging of HOCl solution as a means to disinfect a large space in a short amount of time. Fogging involves aerosolizing the liquid, usually through some

device such as an ultrasonic fogger or humidifier, and dispersing the fog throughout an open space. The exact methods and apparatus used will be discussed in further detail in the following sections.

## 2. Experimental Methods

### *2.1. Solution Preparation*

Hypochlorous acid was produced using two home units available to consumers to buy and use: the EcoloxTech Eco One and RIPPO Sprayer. 1 L of solution was generated using the Eco One by combining 1 L of tap water with 2 g of non-ionized salt and 1 teaspoon of 5% distilled white vinegar in the unit and running two consecutive 10-minute cycles, as instructed by the manufacturer. 300 mL of solution was generated using the RIPPO by combining 300 mL of tap water with 22.5 g of non-ionized salt and allowing the unit to run for two consecutive 10-minute cycles, as also instructed by the manufacturer. The solution produced from each unit was stored in separate opaque bottles away from sunlight. The third solution was purchased from EcoLogic Solutions located in Brooklyn, NY. The free available chlorine concentration (FAC) of each solution was measured by titration, and pH was measured using a digital pH meter.

(a) (b)

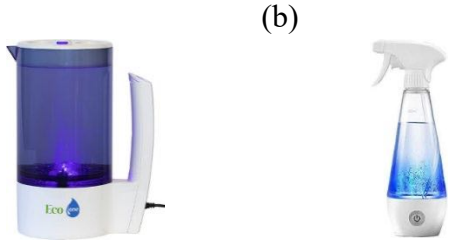

**Figure 3.** (a) Eco One and (b) RIPPO.

### *2.2. Preparing Bacterial Cultures*

*E. faecalis* (ATCC® 19433™) was grown in Brain Heart Infusion Agar (BHI, Difco™) for 24 hours at 37°C. Cells were removed from the plates using a sterile inoculating loop and the bacteria were transferred into a test tube containing 10 mL phosphate-buffered saline (PBS). This tube was vortexed for 30 seconds to ensure all cells were in suspension. A sample of the vortexed bacterial solution was diluted 1:100 and the optical density (OD) of this diluted solution was determined at 600 nm using a spectrophotometer. The bacterial suspension in the original tube was adjusted using more PBS or bacteria until a 1:100 dilution yielded an OD of 0.100, which is approximately 1 x $10^{10}$ cells per mL. Fifty µL of the adjusted concentrated bacterial suspension was spread onto each of three aluminum squares (approximately 1 square inch). The aluminum squares were placed into Petri dishes, without lids, and allowed to dry for approximately 1 hour at 37°C until a dry film was observed on the surfaces of the aluminum squares.

### *2.3. Fogging Procedure*

Two of the three prepared aluminum squares were fogged and compared to a third untreated (not fogged) control. Once fogging began, the control was processed to determine the initial bacteria or virus populations. The samples to be fogged were oriented vertically in a desiccator (VWR Type 250) as shown in Figure 4. Hypochlorous acid was pumped into an ultrasonic fogging machine (Contronics HU-45 Humidifier) and then fogged into the desiccator in continuous streams with an average volumetric flow rate of 0.0556 L/min and particle size between 1 and 3 micron [14].

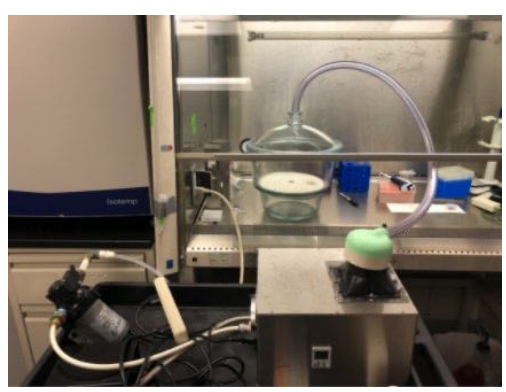

**Figure 4.** Experimental fogging apparatus.

*2.4. Bacteria Quantification (Post-Fogging)*

The fogged samples and un-fogged control were assessed for the number of living, or surviving, bacteria cells. Each sample was immersed individually in a 50 mL test tube containing 5 mL of PBS and vortexed for 5 minutes to suspend all the bacterial cells on the aluminum plate in solution. Then, six 1-in-10 serial dilutions, in PBS, were made and 0.1 mL of each dilution was spread, in triplicate, on BHI plates which were then incubated for 24 hours at 37°C. After incubation, only the dilution plates containing 30 – 300 colony forming units (CFUs) were counted. When taking into consideration the inoculum dilution spread onto counted plates, the average +/- standard deviation of bacterial cells on the control and fogged samples was calculated. The number of surviving fogged bacteria was reported, relative to the untreated control, as the log-reduction of cells caused by the fogging treatment.

*2.5 Cell Culture*

MDCK-2 (ATCC® CRL-2936™) cells were cultured and grown in OptiPRO™ SFM (Gibco) with 1x Glutamax (Gibco) and 100 units/mL penicillin and 100 µg/mL streptomycin. H1N1 PR8 (ATCC® VR-95™) influenza virus were cultured in MEM (Gibco) with 0.2% BSA (Sigma). This step was necessary as viruses need a host cell in order to replicate.

*2.6. Virus Growth and Infection*

50 µL of virus solution was put on the surface of the aluminum samples and dried for 1 hour at 25°C. The samples were fogged according to the same fogging procedure done for the bacteria tests. Post-fogging, the viruses were collected and vortexed with 5 mL of medium. 250 µL of virus solution was added into each well after serial dilution from $10^{-1}$ to $10^{-6}$. The well plates were placed on the rocker for 30 minutes at room temperature. After rocking, the well plates were placed in the incubator at 37°C and 5% $CO_2$ for 1 hour. Then virus solution was replaced with MEM medium with 0.3% tragacanth gum (Sigma) and 0.2% BSA. After 4-day incubation at 33°C and 5% $CO_2$, the samples were stained with 1% crystal violet (Sigma). A plaque assay was used to count the number of infectious viral particles present after fogging compared to the untreated (not fogged) control.

## 3. Results and Discussions

*3.1. Fogging Tests*

Previous experiments conducted by Feng et al. have shown that continuous fogging is more efficient than pulse fogging in terms of the time needed to achieve a ≥5-log reduction in bacteria and ≥3-log reduction in virus, which is required by the EPA in order to claim disinfection [15]. The specific EPA guideline is for these log-reduction targets to be met within less than 10 minutes of contact time. Continuous fogging implies that the sample is fogged once for a set period of time in the beginning and then allowed to rest, whereas pulse fogging implies that bursts of fog are introduced into the desiccator according to set intervals. Furthermore, it was found in these studies that when samples were oriented vertically, the bacteria or virus became harder to kill due to the solution not being able to collect on the surface as easily. For these reasons, the procedure followed here involved testing the most efficient fogging method (continuous fogging) against the more difficult orientation (vertical). Aluminum was used because it is a common metal and surface, and also is hydrophilic, which allowed the bacteria and virus solutions to dry relatively quickly. The exact grade of aluminum is unknown as it was provided as scrap metal from the campus machine shop.

Overall, the commercial solution provided by EcoLogic Solutions was the most effective in killing *E. faecalis* and H1N1 influenza virus, yielding log reductions in these pathogens of 6.59 and 4.90, respectively, after 5 minutes of continuous fogging. Out of the two solutions produced by the home units, the Eco One solution performed better than the RIPPO solution against both pathogens, but still not as well as the EcoLogic solution. However, the Eco One did achieve notable log reductions in *E. faecalis* and H1N1 of 4.21 and 5.36 after 5 and 7.5 minutes of continuous fogging, respectively (Figures 5 and 6). Although the Eco One did not meet the standards set out by the EPA, the log reductions observed were fairly close to the targets of ≥5-log reduction in bacteria and ≥3-log reduction in virus and most likely could have been met with a few more minutes of additional fogging.

Where the EcoLogic and Eco One solutions really differ is in their chlorine concentration. In this pH range of 4-5, HOCl is the predominant chlorine species as shown in Figure 1. Therefore, the difference in efficacy between these two solutions can be attributed to the amount and type of free available chlorine (FAC) that they contain. This is measured through chlorine concentration, and these concentrations are given in the legend of Figure 5. There is almost a 200 ppm difference in chlorine concentration between the EcoLogic and Eco One solutions, which is likely why there is improved performance with the EcoLogic solution. Because the pH of the EcoLogic solution is on the higher end of the 4-5 range, it likely contains some additional FAC in the form of $OCl^-$, which although is known to be less effective than HOCl, does possess some disinfecting properties.

The RIPPO solution possessed comparatively little disinfecting abilities, achieving no more than a 1-log reduction in any of the performed tests. Its high pH (pH 8-9) and chlorine concentration (~750 ppm) is indicative of the fact that the solution contains $OCl^-$, the less effective form of free available chlorine. It is important to note that although less effective, the RIPPO was not designed for a fogging application, rather it was designed to be sprayed directly from the bottle (see Figure 3b). It has been previously found by Feng et al. that fogging can reduce the initial chlorine concentrations by up to 50%. Therefore, it is likely that any disinfecting ability that the RIPPO had in the form of $OCl^-$ was eliminated by the fogging procedure. Furthermore, it should be noted that the base bacteria used for testing by the EPA are different and therefore possess different resistances to such treatments (they use *Staphylococcus aureus* and *Pseudomonas aeruginosa* and do not yet possess a standard procedure for fogging) [15].

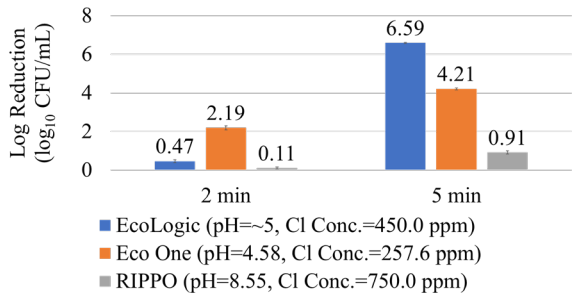


**Figure 5.** Reductions in *E. faecalis* after 2 and 5 minutes of continuous fogging, followed by 5 minutes resting in the desiccator.

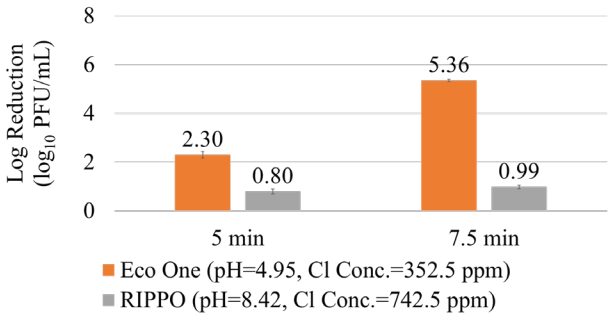


**Figure 6.** Reductions in H1N1 influenza virus after 5 and 7.5 minutes of continuous fogging, followed by 5 minutes resting in the desiccator.

*3.2. Ultraviolet-Visible (UV-Vis) Spectroscopy Characterization Tests*

As mentioned previously in this report, HOCl is approximately 80 times more effective than bleach (known chemically as sodium hypochlorite or NaOCl) in surface disinfection [11]. Due to the difference in efficacy between the three solutions, UV-Vis spectra were taken to characterize and compare the different solutions to bleach. Figure 7 shows the UV-Vis spectra of lab-grade bleach and the RIPPO solution. While not identical, the two spectra show distinct similarities, with a gradual rise and fall in absorbance and a maximum peak around 290 nm. Further comparison of the RIPPO spectra with NaOCl standards published online show even stronger similarities [16]. These results again suggest that the RIPPO unit is producing bleach and therefore may not be suitable for disinfection.

Figure 8, on the other hand, shows the UV-Vis spectra of the EcoLogic and Eco One solutions. The range of wavelength in this graph was reduced to 200-350 nm because outside of this range existed no notable spikes or trends in absorbance. However, the fact that the two spectra follow somewhat similar trends (from right to left) and are clearly different from the spectra in Figure 7, provides evidence that the EcoLogic and Eco One solutions are characterized by something other than bleach, likely hypochlorous acid.

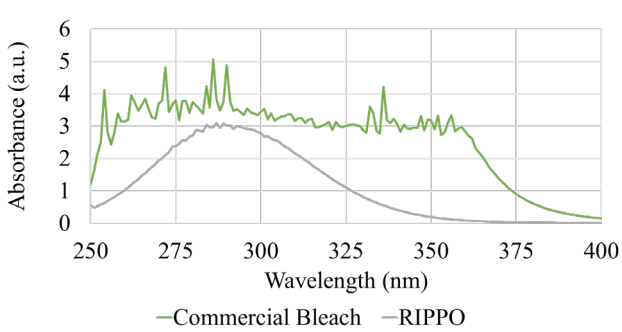


**Figure 7.** Ultraviolet absorption spectra of lab-grade commercial bleach and the RIPPO solution.

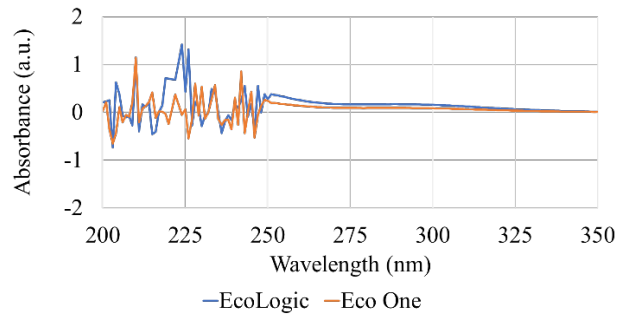


**Figure 8.** Ultraviolet absorption spectra of the EcoLogic and Eco One solutions.

*3.3 Solution Stability Tests*

The stability of the Eco One solution in terms of pH and chlorine concentration was tested to see how it compared with the stability of the EcoLogic solution, which has previously been found by Feng et al. to be very stable (it took a total of 50 days to start seeing significant, defined as >10%, changes in these numbers). Table 1 shows the pH and chlorine concentration (in ppm) of the Eco One solution over a three-week period. The solution was found to be stable, showing only a ~2.4% and ~1.4% decrease in pH and chlorine concentration, respectively, over the 3-week period. These decreases are within reasonable experimental error and likely resulted from the inherent inaccuracies in the pH and titration methods used. This result is important because if this solution is to be used commercially, it should have a long-shelf life.

**Table 1.** Stability of the Eco One solution over a three-week period.

| Time (days) | pH | Cl Conc. (ppm) |
|---|---|---|
| 0 | 4.95 | 352.5 |
| 7 | 4.84 | 350.0 |
| 14 | - | - |
| 21 | 4.83 | 347.5 |

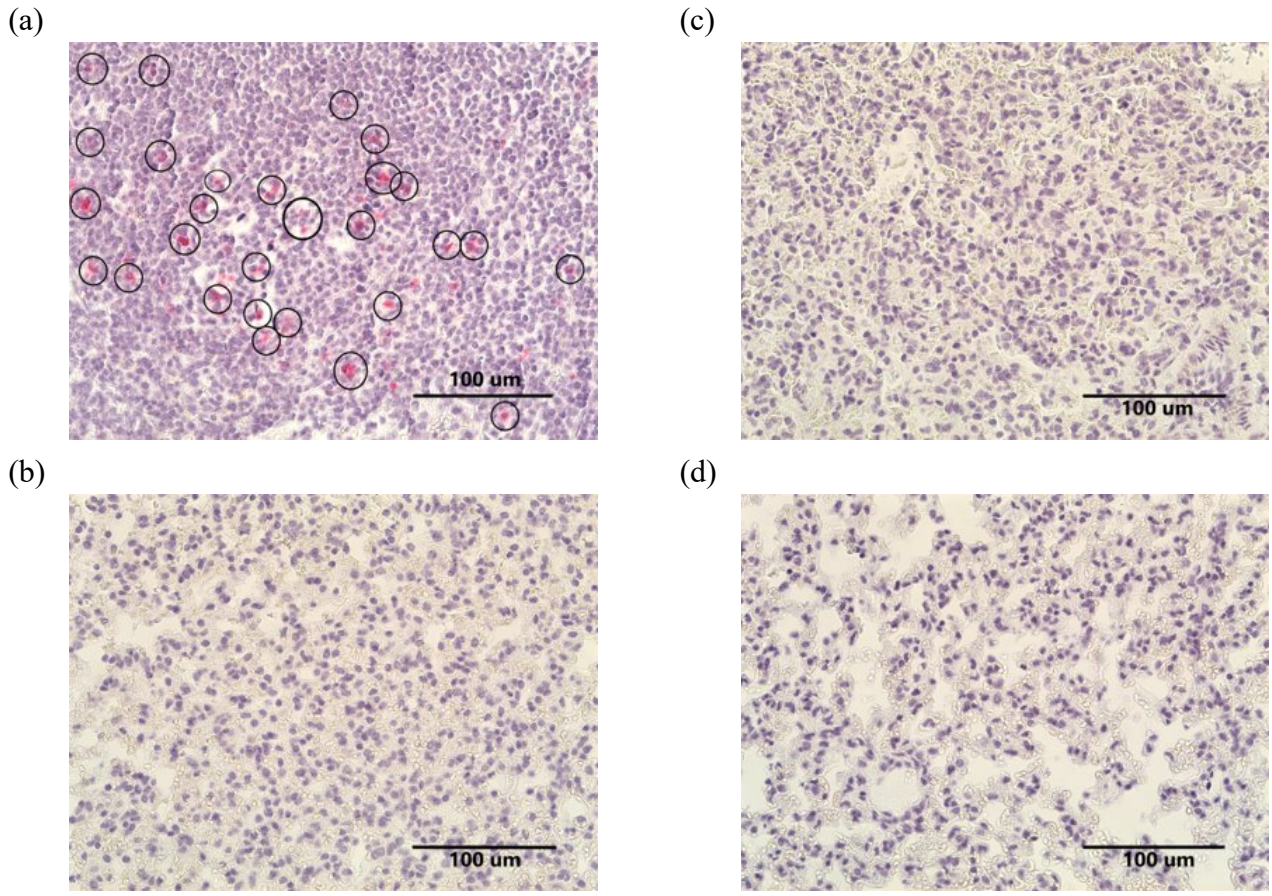


**Figure 9.** Active caspase-3 antibody staining for evidence of apoptosis from the lung tissue of mice. Images taken at 40x magnification. (a) "Positive" control 30% $H_2O_2$. (b) "Negative" control DI water. (c) Eco One solution. (d) RIPPO solution.

*3.4. Cytotoxicity Tests*

According to several safety data sheets (SDSs) published online, HOCl is non-toxic and possesses few safety hazards [17,18]. At high concentrations, HOCl can cause slight irritation to the eyes, skin, and lungs if inhaled. However, in general, none of these hazards are life-threatening and can usually be treated without hospitalization. In fact, HOCl is used in many pools for chlorination and is even safe to use for rinsing fruits and vegetables [2]. The purpose of performing cytotoxicity tests then was to determine if the solution from the RIPPO unit was toxic, as previous results have suggested it is producing bleach (NaOCl), which has the ability to damage living cells. For these tests, 30% hydrogen peroxide ($H_2O_2$) was used as the positive control (will kill the cells), and deionized (DI) water was used as the negative control (will not kill the cells). The two homemade solutions produced by the Eco One and the RIPPO were tested and compared to these two controls to complete the assay.

Lung tissue from already-sacrificed mice were dipped into equivalent amounts of these solutions for 10 seconds and then sent to a pathology lab to be spread and stained for active caspase-3 as evidence of apoptosis. Caspase-3 is a widely-studied apoptotic protein and suitable for a preliminary test like this one. Lung tissue was used

as it is believed that inhalation is the most dangerous form of chlorine exposure, especially if it exists as chlorine gas ($Cl_2$). The bright red spots circled in black in Figure 9a indicate the activation of caspase-3 and initiation of apoptosis after exposure to the positive control. The blue dots, on the other hand, represent intact nuclei, or nuclei that survived the treatment with 30% $H_2O_2$. This was expected, as was the result for the negative control that showed no red spots.

The fact that exposure to the Eco One and RIPPO solutions showed no evidence of apoptosis like the negative control is a promising initial result that the solutions used were non-toxic. However, these results do not fully dismiss the fact that the RIPPO solution could be producing bleach, nor do they claim that these solutions are completely safe. As mentioned previously, chlorine in the form of chlorine gas ($Cl_2$) presents the largest risks to humans and therefore the cytotoxic effects of the fogged solutions should be tested, when there is the greatest likelihood of producing gaseous chlorine.

## 4. Conclusion

Hypochlorous acid, due to its effectiveness against certain pathogens in the past, has been a popular area of research with the ongoing pandemic. One benefit of hypochlorous acid is the ability to produce it from common household materials (water, non-iodized salt, and vinegar). This research tested the effectiveness of a fogged application of both purchased commercial solution and two homemade solutions in their reduction of counts of *E. faecalis* and H1N1. Both the EcoLogic and Eco One solutions were able to achieve ≥99.99% reductions in *E. faecalis* and H1N1 after being fogged continuously for less than 10 minutes of fogging time, the standard disinfection time established by the EPA [15]. However, the RIPPO home unit was not effective, yielding no greater than a 1-log reduction in any of the performed tests. The pH of the RIPPO solution was measured and found to be between 8 and 9, which is likely due to the production of bleach in the unit, suggesting that pH plays a key factor in disinfecting ability. Fogging is a promising method of application because it allows larger areas to be covered in a much shorter amount of time compared to a liquid application, and can be done without sacrificing effectiveness. HOCl is cheap, easy, and safe to use, which makes it a suitable choice for fogging.

## 5. Acknowledgements

The authors would like to respectfully acknowledge Dr. Kuan-Che Feng, Dr. Stephen G. Walker, and Dr. Miriam H. Rafailovich for their time, assistance, and mentorship throughout this research project.

## 6. References

1. Nguyen, Kate, et al. “The Potential Use of Hypochlorous Acid and a Smart Prefabricated Sanitising Chamber to Reduce Occupation-Related COVID-19 Exposure.” *Risk Management and Healthcare Policy*, vol. 14, 22 Jan. 2021, pp. 247–252., doi:10.2147/rmhp.s284897.
2. Rahman, SME, et al. “Electrolyzed Water as a Novel Sanitizer in the Food Industry: Current Trends and Future Perspectives.” *Comprehensive Reviews in Food Science and Food Safety*, vol. 15, no. 3, 25 Feb. 2016, pp. 471–490., doi:10.1111/1541-4337.12200.
3. Park, Geun Woo, et al. “Evaluation of Liquid- and Fog-Based Application of Sterilox Hypochlorous Acid Solution for Surface Inactivation of Human Norovirus.” *Applied and Environmental Microbiology*,

vol. 73, no. 14, 4 May 2007, pp. 4463–4468., doi:10.1128/aem.02839-06.

4. HAKIM, Hakimullah, et al. "Evaluation of Sprayed Hypochlorous Acid Solutions for Their Virucidal Activity against Avian Influenza Virus through *in Vitro* Experiments." *Journal of Veterinary Medical Science*, vol. 77, no. 2, Feb. 2015, pp. 211–215., doi:10.1292/jvms.14-0413.
5. Van Tyne, Daria, et al. "Structure, Function, and Biology of the Enterococcus Faecalis Cytolysin." *Toxins*, vol. 5, no. 5, 2013, pp. 895–911., doi:10.3390/toxins5050895.
6. "2009 H1N1 Pandemic (H1N1pdm09 Virus)." *Centers for Disease Control and Prevention*, Centers for Disease Control and Prevention, 11 June 2019, www.cdc.gov/flu/pandemic-resources/2009-h1n1-pandemic.html.
7. "Scientific Brief: SARS-CoV-2 Transmission." *Centers for Disease Control and Prevention*, Centers for Disease Control and Prevention, May 2021, www.cdc.gov/coronavirus/2019-ncov/science/science-briefs/sars-cov-2-transmission.html.
8. "2009 H1N1 Flu ('Swine Flu') and You." *Centers for Disease Control and Prevention*, Centers for Disease Control and Prevention, Feb. 2010, www.cdc.gov/h1n1flu/qa.htm.
9. Fair, Gordon M., et al. "The Behavior of Chlorine as a Water Disinfectant." *Journal - American Water Works Association*, vol. 40, no. 10, 1 Oct. 1948, pp. 1051–1061., doi:10.1002/j.1551-8833.1948.tb15055.x.
10. *Handbook of Chlorination and Alternative Disinfectants*, by George Clifford White, Wiley, 1999, pp. 153–156.
11. Da Cruz Nizer, Waleska Stephanie, et al. "Surviving Reactive Chlorine Stress: Responses of Gram-Negative Bacteria to Hypochlorous Acid." *Microorganisms*, vol. 8, no. 8, 11 Aug. 2020, p. 1220., doi:10.3390/microorganisms8081220.
12. Benzoni T, Hatcher JD. "Bleach Toxicity." *StatPearls* [Internet]. Treasure Island (FL): StatPearls Publishing, Updated June 2020, https://www.ncbi.nlm.nih.gov/books/NBK441921/
13. Contronics® HU-45 Humidifier User Manual. September 2018.
14. ISHIHARA, MASAYUKI, et al. "Stability of Weakly Acidic Hypochlorous Acid Solution with Microbicidal Activity." *Biocontrol Science*, vol. 22, no. 4, 2017, pp. 223–227., doi:10.4265/bio.22.223.
15. "Interim Guidance - Review for Products Adding Residual Efficacy Claims." *EPA*, Environmental Protection Agency, 28 Apr. 2021, www.epa.gov/pesticide-registration/interim-guidance-review-products-adding-residual-efficacy-claims.
16. Evans, Kieran. "Quantification of Sodium Hypochlorite in Disinfectants." *PerkinElmer*, PerkinElmer, Inc., www.perkinelmer.com/lab-solutions/resources/docs/app_quantification-of-sodium-hypochlorite.pdf.
17. OXCIDE® Hypochlorous Acid Solution Safety Data Sheet. CAS No. 7790-92-3. June 2015.
18. ChlorKing® Hypochlorous Acid Solution Material Safety Data Sheet. CAS No. 7790-92-3. January 2017.

# Swelling and Deweaving of cotton muslin fabric in aqueous NaOH solution

Hang Zhang Cao[a], Yiqian Yao[a], and Taejin Kim[a]

[a] *Department of Materials Science and Chemical Engineering, Stony Brook University, Stony Brook, NY 11794, USA*

**Abstract**

Textile wastes have gained increasing share in the total municipal solid waste generated each year with only ~14% of the textile wastes being recycled. Common methods of textile recycling involves mechanical shredding or chemical dissolution. These methods reduce fiber quality and can be either high energy consuming or hazardous to the environment. This paper investigates a method of textile recycling by combining physical and chemical recycling processes in the form of mechanical spinning in aqueous sodium hydroxide solution. Cotton muslin fabric samples in size of 3 by 3 cm were treated with 1 M aqueous NaOH solution at temperatures of 3 °C, room temperature (~23°C), 35°C, 50 °C, and 70 °C. The goal of the experiment is to deweave the cotton muslin fabric while optimizing the retainment of its physical properties. Fourier-transform infrared spectroscopy, optical microscopy, and tensile strength tests were conducted to evaluate the effect of treatment on the chemical and physical properties of cotton muslin fabric. It was concluded that cotton muslin fabric treated with 1 M aqueous NaOH solution can successfully deweave without inducing chemical structural change. Treatment with 3 °C solution yielded the best result with ~40% retention in modulus, ~78% retention in tensile strength, and ~215% increase in toughness. For cotton muslin fabric treated with temperature between 23-70 °C, physical properties increase with increasing temperature.

*Keywords*: recycling, cotton fabric, mercerization, sodium hydroxide, deweaving, Fourier-transform infrared spectroscopy, tensile strength

## 1. Introduction

The amount of textile waste generated has been increasing over the past years. According to the data from the United States Environmental Protection Agency, nearly 17.03 million tons of textile waste was generated in 2018 [1]. The major recovery methods for textile waste are reuse, recycle, and combustion for energy. Approximately 14.7% (2.51 million tons) of textile waste is recycled and ~18.9% (3.22 million tons) is used for energy recovery [1]. The remaining 66.4% (11.3 million tons) of textile waste had been landfilled. The two popular methods of textile waste recycling are mechanical and chemical recycling [2,3] Unfortunately, the shortcomings of these two methods limit the effectiveness of the recycling result. [4] Mechanical recycling shreds and tears the waste fabric apart into a fibrous state as shown in Figure 1. [5] These fibers are then used to spin into yarn. The shredding process damages the quality of the fabrics heavily, which reduces the length,

strength, and softness significantly. Recycled fiber whose length is shorter than 10 mm is considered as waste. To ensure product quality, virgin cotton fibers are spun together with mechanically recycled fiber, with only less than 30% of the recycled fiber can be used. [6,7] Chemical recycling can be broken down into three steps: pretreatment process such as hydrolysis, dissolving process for the fabric, and a wet-spinning process to regenerate dissolved fibers. [8] The dissolving process requires a highly alkaline, non-derivatizing organic solvents or simple solvent such as sodium hydroxide (NaOH) in high concentration. [9] These solvents can be highly toxic and expensive. The productivity of chemical dissolution and fiber regeneration is limited by the high cost and long process time. [6] Therefore, many researchers develop the chemical recycling process of cotton waste in various treatments and applications such as producing glucose and polyester by enzymatic hydrolysis. [10]

**Figure 1.** Mixture with fibers and yarns produced by mechanical shredding. [4]

A fabric recycling method combining mechanical and chemical strategies through means of deweaving is investigated in this research. Different from the previous studies, the mechanical process used in this research utilizes magnetic stirring. A relatively mild chemical agent of 1 M NaOH is used in this experiment to aid the fabric deweaval in contrast to the highly alkaline solution adapted by the common chemical recycling methods. The target of this research is to increase the recycling yield as well as optimizing the retention of fiber qualities measured by the modulus, tensile strength, and toughness.

Cotton muslin fabric is used for this research due to its huge market and popularity. [3] Cotton is roughly composed of 90% cellulose and 10% noncellulosics substances such as proteins, waxes, prectins, inorganics, and others. [11] Aqueous sodium hydroxide (NaOH) is used as the chemical agent and its effect on fabric deweaval is tested under different conditions. NaOH is one of the most common chemicals to swell or dissolve cellulose. [12-16] The swelling mechanism is caused by the removal of the cellulose carboxyl group and intra-hydrogen bonds by the interaction with Na-ions in NaOH. [17,18] This interfibrillar swelling is represented by a series of ballooning phenomena along the cellulose fiber. NaOH hydrates bind to the cellulose and avoid the aggregation of cellulose macromolecules, which leads to cellulose dissolution [19-21]. The swelling and dissolution efficiency depends on the NaOH temperature. At higher temperatures (> 50 °C), cellulose swells, and at lower temperatures (< 0 °C), cellulose tend to dissolve in combination with swelling. [22] Alkaline solution treatment improves quality (e.g., dyeability and strength) of fabric materials. [19,23]

## 2. Materials and Methodology

### *2.1. Materials*

Cotton muslin samples, which were originally procured from Arthur R. Johnson Co., Inc., Brooklyn, N.Y, were purchased from the Fashion Institute of Technology (New York). Sodium hydroxide (NaOH, reagent grade) was obtained from Sigma-Aldrich and was used as aqueous solution with the addition of deionized water (resistivity: ~20 mΩ/cm).

### *2.2. Deweaving treatment*

A Benchmark scientific hotplate stirrer (H3760-HS) connected with a temperature probe (H3760-TP) was used for the heating solution, stirring process and controlling temperature. 50 mL of 1 M NaOH solution contained in a 250 mL beaker was achieved to room temperature (~23 °C), 35 °C, 50 °C, 70 °C using the hotplate. 3 °C was achieved using an ice bath surrounding the beaker. The temperature probe is placed in the solution to monitor the temperature. A cotton muslin fabric sample with a 3 cm x 3 cm dimension was added into the solution and spun by a magnetic rectangular stirring bar (length: 3.5 cm) at a speed of 300 rpm. Reaction stops after 1 hour of reaction or when the cotton muslin fabric is fully deweaved. After finishing the reaction, the sample was separated from the NaOH solution, rinsed with deionized water, and dried at room temperature then overnight in a temperature controlled oven at 50 °C. The leftover NaOH solution was then discarded in the designated chemical solution container.

*2.3. Recyclability Test*

Four cotton muslin samples were deweaved one after another in the same NaOH solution at 35 °C following the procedure in 2.2. The evaporated NaOH solution (1~2 mL) is replenished with a pipet to maintain a constant concentration. The dissolved cellulose from each sample was let alone accumulating in the solution.

*2.4. Fourier-transform Infrared Spectroscopy*

The Fourier transform Infrared (FTIR) spectroscopy was conducted using a Nicolet™ iS50 FTIR Spectrometer equipped with an diamond attenuated total reflectance (ATR) accessory. The spectra (32 scans/sample, 4 cm-1 resolution) were collected in the range of 400~4000 cm-1 wavenumbers at room temperature by a DTGS detector. Each spectrum was corrected by collecting a background spectrum before collecting the sample spectrum and doing spectra subtraction using the OmnicTM software (Thermo Scientific).

*2.5. Tensile Properties Test*

The tensile strength test method follows the *Standard Test Method for Tensile Strength and Young's Modulus of Fibers* (ASTM C1557 - 14). Five single strands of fiber specimens are picked out randomly from each sample of deweaved muslin fabric. Fiber is mounted and clamped on an Instron 5542 Advanced Material Testing System at a constant cross-head displacement rate of 2.00 mm/min. Fiber failures are checked to be at the center of the fiber and not be around the gripping region.

Stress (MPa) vs. Strain % is plotted on OriginLab software. Young's modulus is calculated from the slope of the linear region. Tensile strength is taken from the maximum value of the y-axis. The toughness is calculated by taking the area under the curve.

The Young's modulus measures the muslin fabric's resistance to elastic deformation under stress, the tensile strength measures the maximum stress of muslin fabric before breakage, and the toughness measures the material's ability to absorb energy and plastically deform without fracture.

*2.6. Optical Microscopy*

Optical images were obtained using Olympus IX51 Inverted Phase Contrast Fluorescence Microscope with 4x magnification.

**3. Results and Discussion**

*3.1. Deweaving result*

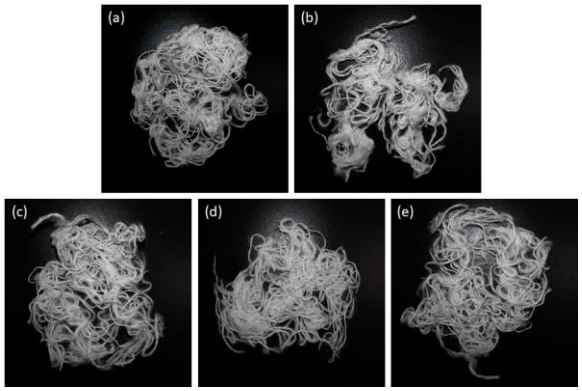


**Figure 2.** Digital camera images of deweaved muslin samples treated with different temperatures. (a) 3 °C (b) 23 °C (c) 35 °C (d) 50 °C (e) 70 °C. Conditions: NaOH concentration (1 M, 50 mL), spinning speed (300 rpm).

Figure 2 shows the digital camera images of deweaved cotton muslin fabric samples treated at different solution temperatures. All of the samples have successfully deweaved with no fabric entanglement. The deweaving time has a negative correlation with temperature. The average deweaving time for 3 °C, 23 °C, 35 °C, 50 °C, and 70 °C are 70 min, 45 min, 30 min, and 20 min, respectively. This relationship conveys that the kinetics from the hot solution may contribute to the deweaval of the muslin fabric. The pH of the solution is measured before and after treatment and no significant change is detected.

*3.2. Temperature variation*

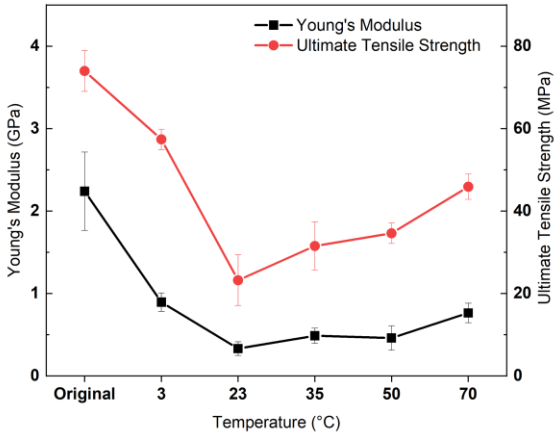


**Figure 3.** Young's Modulus and Tensile strength of muslin fabric treated with 1 M NaOH at different temperatures.

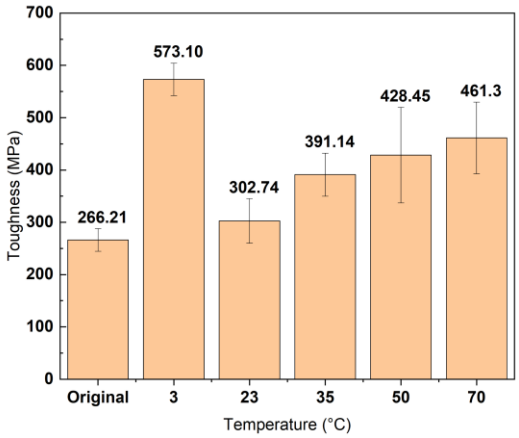


**Figure 4.** Toughness of muslin fabric sample treated with 1 M NaOH at different temperatures.

Figure 3. Shows both the Young's modulus and tensile strength of the original sample (control) and muslin fabric treated with 1 M NaOH at temperatures of 3 °C, 23 °C, 35 °C, 50 °C, and 70 °C. Although many experiments have proved fabric treatment with alkali through means of soaking can improve fabric's physical properties, the data shown in Figure 3 shows otherwise. [24] This may be due to the mechanical spinning of the stirring bar affecting the physical structure of the muslin fabric. Amongst the tested samples, the muslin fabric treated with 3 °C yielded the best result in terms of the Young's modulus and tensile strength. When compared to the original sample, the 3 °C treated muslin fabric exhibits a retention of 39.96 % in modulus and 77.56 % in tensile strength. This is because at a low temperature of 0 °C, the cotton fibers only swell slightly [22]. The swelling of the fiber decreases the interfiber bonding strength and fiber strength [25,26]. This explains why the 23 °C treated sample has the lowest retention in the Young's modulus and tensile strength of 14.82% and 24.56 %, respectively. However, the upward trends in Figure 3 starting from 23 °C to 70 °C suggests that the Young's modulus and tensile strength increases with increasing

temperature. The research by Sameii et al found that hot mercerization increases the tensile strength of cotton fiber[27]. Research also revealed a decrease in the fiber crystallinity at higher temperatures, and the reduction of fiber crystallinity increases tensile strength [28]. However, after 70 °C, the fiber quality will decrease due to excess heat softening the fiber material [27].

Even though the Young's modulus and ultimate tensile strength deteriorated for the treated muslin fibers, the toughness of these fibers improved. The 3 °C treated muslin fabric showed the greatest improvement of 215%. The muslin fabric treated with 23, 35, 50 and 70 °C showed 113.72%, 146.93%, 160.95%, and 173.29% toughness improvement, respectively. Mercerization increases the elongation of the cotton fabric. [24] As elongation increases, the fibers become more elastic, hence can absorb more energy. At higher temperatures, the elongation of the muslin fibers also increases. [27] This explains the positive correlation between the toughness and the solution temperature, as shown in Figure 4. The muslin sample treated with 3 °C solution has the highest toughness mainly due to its high tensile strength retainment and the increase in fiber elongation. From the data shown in Figure 3 and Figure 4, it can be concluded that 3 °C NaOH solution is the optimum condition for this method of fabric recycling.

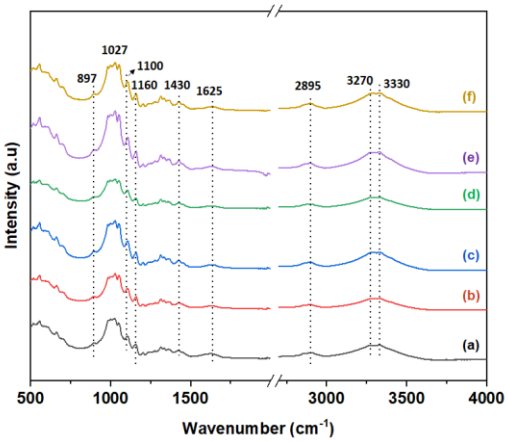


**Figure 5.** Fourier-transform infrared spectra of muslin cotton fabric. (a) original sample (b) 3 °C treated (c) 23 °C treated (d) 35 °C treated (e) 50 °C treated (f) 70 °C treated. Conditions: NaOH concentration (1 M, 50 mL), spinning speed (300 rpm).

Figure 5 shows the FTIR spectra of the untreated muslin fabric and the treated muslin fabric samples. The broad band stretching from ~3270-3330 $cm^{-1}$ is assigned to the OH stretching vibration, which is an indication of the crystalline structure of cellulose Iβ.[29] The peak at ~2895 $cm^{-1}$ is assigned to C-H symmetrical vibration of polysaccharides, and the peak at ~1625 $cm^{-1}$ corresponds to C-H symmetrical vibration of cellulose. [30,31] These peaks are characteristic of cellulose. The peak at ~1430 $cm^{-1}$ is assigned to HOC in plane bending vibration and is another indication of the cellulose I crystallinity. This peak is sensitive to the crystalline changes of cellulose [32,33]. Hence, the crystal structure of the sample can be interpreted to be cellulose I, which is native cellulose. The peak at ~1160 $cm^{-1}$ is assigned to C-O-C asymmetric stretching, the peak at ~1100 $cm^{-1}$ is assigned to the OH group of cellulose, and peak at ~1027 $cm^{-1}$ is assigned to -OH bonds in cellulose. [31,32,34,35]. Finally, the peak at ~897 $cm^{-1}$ is assigned to β-glycosidic bonds of cellulose. [30,36] These peaks are all characteristic of cellulose and since their intensities remain relatively constant and there are no shifts in peaks, it can be concluded that the 1 M NaOH treatment does not alter the chemical composition of the cotton muslin fabric.

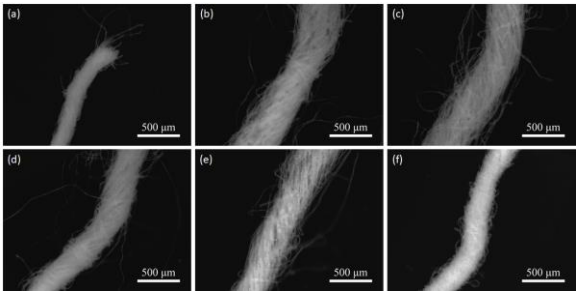


**Figure 6.** Optical microscope images (4 X) of muslin cotton fabric treated with 1 M NaOH at different temperatures. (a) Original sample (b) 0 °C (c) 23 °C (d) 35 °C (e) 50 °C (f) 70 °C. Reaction conditions: NaOH concentration (1M 50 mL), spinning speed (300 rpm).

Figure 6 shows the optical microscope images (× *4*) of a single strand of muslin fabric taken from each sample. In comparison with the original sample, all of the treated muslin samples display an increase in the fiber diameter - an indication of interfibrillar swelling by NaOH. Some interfibers have been broken and start to detach from the edges of the fiber strand. The swelling also resulted in the loosening and untwisting of the interfibers, particularly visible in Figure 6d. Untwisting of the fiber can lead to decrease in the young's modulus and tensile strength [37]. Nevertheless, the fiber strand remains intact since the reaction is carried out with a mild NaOH concentration of 1 M relative to the common chemical dissolution of cellulose using 8 M or higher concentration NaOH. The optical microscopy suggests that our reaction is feasible in terms of deweaving the fabric without dissolving them into microfibers.

*3.3. Determining the feasibility of reusing the same NaOH solution*

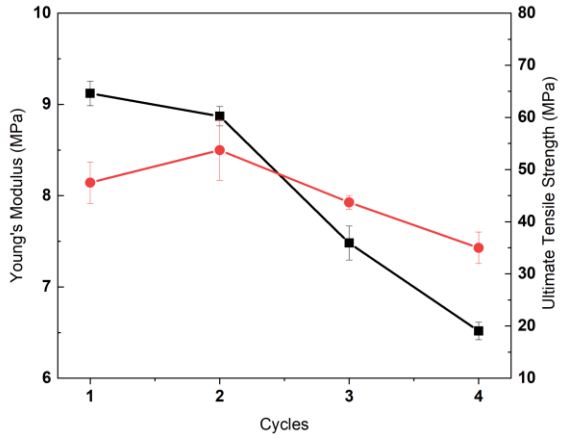


**Figure 7.** Young's Modulus and Tensile strength of muslin fabric samples treated with the same solution at 35 °C. Conditions: NaOH concentration (1 M, 50 mL), temperature (35 °C), spinning speed (300 rpm).

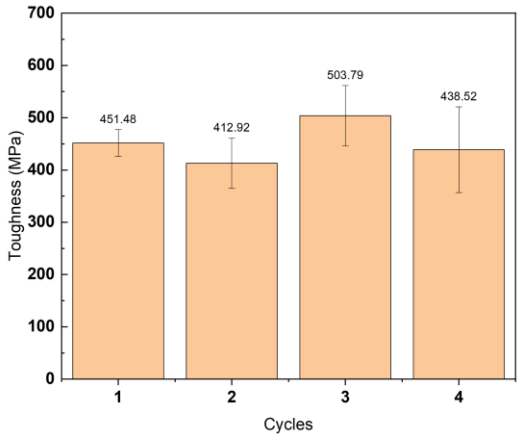


**Figure 8.** Toughness of muslin fabric samples treated with the same solution. Conditions: NaOH concentration (1 M, 50 mL), temperature (35 °C), spinnin speed(300 rpm).

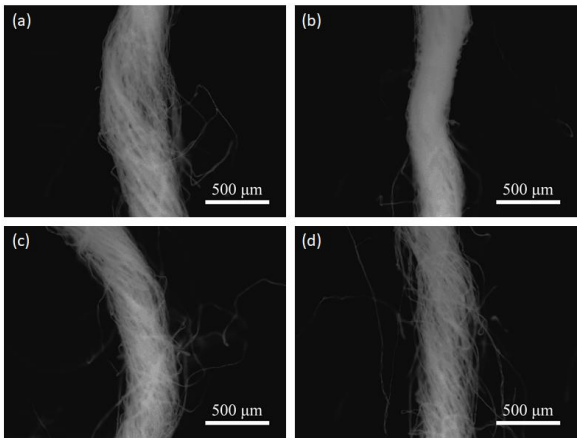

**Figure 9.** Optical microscope images of muslin fabric treated with the same NaOH solution. (a) 1st cycle (b) 2nd cycle (c) 3rd cycle (d) 4th cycle. Reaction conditions: NaOH concentration (1M 50 mL), temperature (35 °C), spinning speed (300 rpm).

Despite its low concentration, 1M NaOH still possesses toxicity. If possible, reusing the NaOH solution for multiple treatments can benefit the economics of this recycling method. To test the feasibility of reusing the same NaOH solution, muslin fabric samples are deweaved one after another in the same NaOH solution. A total of 4 cycles are tested, and the Young's modulus, tensile strength, and toughness of the muslin fabric samples are shown in Figure 7 and Figure 8. Although experimental conditions were kept constant for each cycle, the modulus and the tensile strength decrease after each cycle. The tensile strength of the 2nd cycle appears to be higher compared to the 1st cycle. However, due to the large error bars of these two cycles, this increasing trend is not significant and hence it is safe to conclude a decreasing trend for the tensile strength. This trend may be related to the accumulation of interfibers in the solution. During the spinning process, some interfibers break and detach from the fabric and remain in the solution. The accumulated interfibers provide resistance to the flow and interfere with the fabric surface. As shown in Figure 9d, there are more numbers of interfiber breakage and detachment from the fiber strand on the sample treated at the 4th cycle compared to the sample treated at the 1st cycle.

Despite the reduction in the Young's modulus and the tensile strength, the toughness of the muslin fabric samples remains relatively constant for each cycle, as shown in Figure 8. The relatively large error bars suggest a large variation in the fiber quality from each sample. However, the toughness of the samples averages around ~ 400 MPa, which agrees with the toughness of the muslin cotton fabric treated at 35 °C shown in Figure 4.

It is concluded that although the fiber quality decrease with each cycle, the toughness of the muslin fabric samples remain constant, therefore it is still feasible to reuse the same NaOH solution for treatment up to a certain number of cycles.

## 4. Conclusion

The proposed method of combining mechanical force (spinning) with a chemical agent (NaOH) to recycle cotton fabric through means of deweaval is shown to be achievable. Mercerization by NaOH improves the toughness of the muslin fabric. The optimum temperature for the process is determined to be 3 °C, with a 39.96 % retention in modulus, 77.56% retention in tensile strength, and a 215% increase in the toughness. The effect of NaOH solution temperature on the fiber quality is shown to be a positive correlation. Increasing the solution temperature improves the modulus, tensile strength, and toughness of the muslin fabrics. Reusing the same NaOH solution for reaction slightly reduces the young's modulus and tensile strength but has minimal effect on the toughness of the muslin fabric. It is safe to conclude that reusing the NaOH solution is feasible and our proposed method can be an environmentally friendly and economical alternative for fabric recycling. In terms of future research, scaling up and deweaving large muslin fabric will be the priority.

## 5. Acknowledgements

We would like to thank our mentor Dr. Taejin Kim for his guidance through this project. We would also like to thank Prof. Tannenbaum, Prof. Rafailovich, and Prof. Meng for providing us with the spectroscopic and microscopic instruments.

The authors acknowledge funding support from the National Science Foundation (NSF-CBET-1948422). This work was supported by the Ministry of Education of the Republic of Korea and the National Research Foundation of Korea (NRF 2019S1A5A2A03054508).

## 6. References


1. Advancing Sustainable Materials Management: 2018 Fact Sheet. United States Environmental Protection Agency, U.S. Government Printing Office: Washington, DC, 2020. p. 3.
2. Björquist, S. Separation for regeneration - Chemical recycling of cotton and polyester textiles. Master Thesis, The Swedish School of Textiles, June 2017.
3. Gustav Sandina, B.; Petersbc, G.M. Environmental impact of textile reuse and recycling – A review. *J Clean Product* **2018**, *184*, 353-365.
4. Wang, Y. Fiber and Textile Waste Utilization. *Waste Biomass Valor* **2010**, *1*, 135–143.
5. Wanassi, B., Azzouz, B., & Hassen, M. B. Value-added waste cotton yarn: Optimization of recycling process and spinning of reclaimed fibers. *Industrial Crops and Products* **2016**, *87*, 27–32.
6. Johnson, S., Echeverria, D., Venditti, R., Jameel, H., Yao, Y. Supply Chain of Waste Cotton Recycling and Reuse: A Review. *AATCC Journal of Research* **2020,** *7*, 19-31(13)
7. Wanassi, B., Azzouz, B., & Hassen, M. B. Industrial cotton waste: Recycling, Reclaimed fiber behavior and quality prediction of its blend. *TEKSTİL ve KONFEKSİYON* **2018**, 28(1)
8. Liu, W.; Liu, S.; Liu, T.; Liu, T.; Zhang, J.; Liu, H. Eco-friendly post-consumer cotton waste recycling for regenerated cellulose fibers. *Carbohydr. Polym.***2018,** *206*, 141–148.
9. Qi, H., Liebert, T., Yang. Q., Thomas Heinze, T., Zhang, L. The dissolution of cellulose in NaOH-based aqueous system by two-step process. *Cellulose* **2011,** *18*:237–245
10. Li, X., Hu, Y., Du, C., & Lin, C. S. K. (2018). Recovery of Glucose and Polyester from Textile Waste by Enzymatic Hydrolysis. *Waste and Biomass Valorization* **2019**. *10*, 3763–3772.
11. Gordon, S.; Hsieh, Y.-L. 1 - Chemical structure and properties of cotton. *Cotton: Science and Technology*; Woodhead Publishing: Cambridge, United Kingdom, 2007; pp. 3-34, ISBN 978-1-84569-026-7.
12. Davidson, G.F. The dissolution of chemically modified cotton cellulose in alkaline solutions. Part 1: in solutions of NaOH, particularly at T C below the normal. *J Text Inst* **1934**, *25*,174–196.
13. Davidson, G.F. The dissolution of chemically modified cotton cellulose in alkaline solutions. Part 2: a comparison of the solvent action of solutions of Lithium, Sodium, Potassium and tetramethylammonium hydroxides. *J Text Inst* **1936**, *27*:112–130.
14. Zhou, J.; Zhang, L. Solubility of cellulose in NaOH/Urea aqueous solution. *Polym J* **2000**, *32–10*, 866–870.
15. Ershova, O.; Costa, E.V.; Fernandes, A.J.S.; Domingues, M.R.; Evtuguin, D.V.; Sixta, H. Effect of urea on cellulose degradation under conditions of alkaline pulping. *Cellulose* **2012**, *19*, 2195-2204.
16. Zhang, S.; Wang, W.; Li, F.; Yu, J. Swelling and dissolution of cellulose in NaOH aqueous solvent systems. *Cellulose Chem. Technol.* **2013**, *47*, 671-679.
17. Santos, N.M.; Puls, J.; Saake, B.; Navard, P. Effects of nitren extraction on a dissolving pulp and influence on cellulose dissolution in NaOH–water. *Cellulose* **2013**, *20*, 2013-2026.
18. Lewin, M. Oxidation and aging of cellulose. *Macromol. Symp.* **1997**, *118*, 715-724.
19. Saloheimo, M.; Paloheimo, M.; Hakola, S.; Pere, J.; Swanson, B.; Nyyssonen, E.; Bhatia, A.;

Ward, M.; Penttila, M. Swollenin, a Trichoderma ressi protein with sequence similarity to the plant expansions, exhib-its disruption activity on cellulosic materials. *Eur. J. Biochem*. **2002**, *269*, 4202-4211.

20. Öztürk, H. and Bechtold, T. Effect of NaOH Treatment on the Interfibrillar Swelling and Dyeing Properties of Lyocell (TENCEL®) Fibres. *Fibres & Textiles in Eastern Europe* **2007**, *15*, 5-6 (64-65): 114-117.
21. Cuissinat, C.; Navard, P. Swelling and Dissolution of Cellulose Part II: Free Floating Cotton and Wood Fibres in NaOH–Water–Additives Systems. *Macromol. Symp* **2006**, *244*, 19-30.
22. Jin, H., Zha, C., Gu, L. Direct dissolution of cellulose in NaOH/thiourea/urea aqueous solution. *Carbohydrate Research* **2007**, *342(6,7)*, 851-858
23. Qi, H., Chang, C., Zhang, L. Effects of temperature and molecular weight on dissolution of cellulose in NaOH/urea aqueous solution. *Cellulose volume* **2008,** *15*, 779–787
24. Duchemin, B.J.C. Mercerisation of cellulose in aqueous NaOH at low concentrations. *Green Chem* **2015**, *17*, 3941-3947.
25. Khalifa. M.E. Mercerization of Cotton Yarn Fibers. Optimization of Caustic Soda Concentration via Degree of Mercerization, Dyability and Mechanical Properties. *International Journal of Textile Science* **2017**; *6(1)*: 15-19
26. Ji, Y., Peng, Y., Strand, A., Fu, S., Sundberg, A., Retulainen, E.A. Fiber evolution during alkaline treatment and its impact on handsheet properties. *BioResources* **2018,** 13(4)
27. Njoku, R. E.,Obikwelu, D. Swelling Characteristics and Tensile Properties of Natural Fiber Reinforced Plastic in Selected Solvents. *Nigerian Journal of Technology* **2008,** *27*(2)
28. Sameii, N., Mortazavi, S.M, Rashidi, A.S., Sheikhzadah-Najar, S. An Investigation on the Effect of Hot Mercerization on Cotton Fabrics Made up of Open-End Yarns. *Journal of Applied Sciences* **2008**. *8*
29. Kondo, T. The assignment of IR absorption bandsdue to free hydroxyl groups in cellulose. *Cellulose* **1997**, *4*, 281±292
30. Terpáková, E., Kidalová, L., Eštoková, A., Čigášová, J., Števulová, N. Chemical Modification of Hemp Shives and their Characterization. *Procedia Engineering* **2012,** *42*, 931-941
31. Hospodarova, V., Singovszka, E., Stevulova,N. Characterization of Cellulosic Fibers by FTIR Spectroscopy for Their Further Implementation to Building Materials. *American Journal of Analytical Chemistry*, **2018**, *9*, 303-310
32. Schwanningera, M., Rodriguesc, J.C., Pereirac, H., Hinterstoisser, B.Effects of short-time vibratory ball milling on the shape of FT-IR spectra of wood and cellulose. *Vibrational Spectroscopy* **2004,** *36*, 23–40
33. Oh, S.Y., Yoo, D.I., Shinb, Y., Seo, G. FTIR analysis of cellulose treated with sodium hydroxide and carbon dioxide. *Carbohydrate Research* **2005,** *340*, 417–428
34. Yang, Y.P., et al. Structural ATR-IR analysis of cellulose fibers prepared from a NaOH complex aqueous solution. 2017 IOP Conf. Ser.: Mater. Sci. Eng. 213, 012039
35. Zhai, R., Chi, F., and Zhou, X. (2016). "NaOH-thiourea aqueous solution treatment of cellulose fiber and its effects on bulk and softness," BioRes. 11(4), 8703-8719.
36. Oh,S.Y., Yoo,D.I., Shin, Y., Kim, H.C., Kim, H.Y., Chung, Y.S., Parkd, W.H., Youke, J.H. Crystalline structure analysis of cellulose treated with sodium hydroxide and carbon dioxide by means of X-ray diffraction and FTIR

spectroscopy. *Carbohydrate Research* **2005,** *340*, 2376–2391

37. Sze, G.M., Spruiell, J.E., White, J.L. The Influence of Drawing, Twisting, Heat Setting, and Untwisting on the Structure and Mechanical Properties of Melt-Spun High-Density Polyethylene Fiber. Applied Polymer Science 1976, 20(7), 1823-1847

# The Study of Nitric Oxide Oxidation Reaction using COMSOL

Joceline Gan [a], Feng Yi Guan [a], Chloe Martinez [a], Vincent Spiteri [a]

[a] *Department of Materials Science and Chemical Engineering, Stony Brook University, Stony Brook, NY 11794, USA*

**Abstract**

COMSOL Multiphysics is a finite element analysis simulation software, which includes a Chemical Reaction Engineering Module that can be applied conveniently to study different chemical reactions. One important reaction that can be effectively explored is the nitric oxide (NO) oxidation. This reaction was chosen due to its negative impact on the environment as various industrial processes produce this gaseous pollutant, which can be further oxidized to a more harmful compound, nitrogen dioxide ($NO_2$). It was reported that the NO oxidation reaction operates via a third order reaction scheme ($2NO + O_2 \rightarrow 2NO_2$, $r = 2k[NO]^2[O_2]$), which reduces to second order in excess oxygen ($r = 2k'[NO]^2$).

The main objective of this research is to investigate the viability of COMSOL in replicating experimental data and its ability to provide predictive modelling for the NO oxidation reaction. The simulated results produced by COMSOL were found to be in strong agreement with experimental data, encouraging extended research using the constant volume batch reactor simulation model. Since various literature data showed a wide range of rate constant (k) values (1,600-14,160 $dm^6\ mol^{-2}\ s^{-1}$), the COMSOL model predicted that a small error in the experimentally obtained concentrations can result in a large discrepancy in the derived k value.

*Keywords*: nitric oxide oxidation, rate constant, kinetics, COMSOL, simulation, predictive modelling

## 1. Introduction

### *1.1. COMSOL*

With recent technological advancements, COMSOL is a powerful modeling program used in areas of engineering, scientific research, and manufacturing to better understand and predict the outcomes of processes, develop new models, and optimize existing models. Specifically, the Chemical Reaction Engineering Module provided by COMSOL has been employed to study thermodynamics, mass/heat transfer, kinetics, and reactor types for many chemical processes [1-3]. Conveniently, COMSOL contains a database of the thermodynamic properties of commonly seen compounds, whereby chemical behaviors can be accurately simulated depending on the parameters the user specifies. Moreover, COMSOL applies various theoretical concepts and governing equations (e.g., fundamental rate law and ideal gas law) when computing results [1].

One of the main benefits COMSOL presents is the ability to alter reaction parameters and quickly simulate chemical reaction systems; thus, the impact the changed parameters have on a system can be predicted without having to perform experiments in a laboratory setting [4]. This provides a more economically and environmentally sustainable option for experiments that would be difficult or expensive to carry out in a lab. If needed, reactions can first be simulated in COMSOL to test their viability and with promising results, a real-world experiment can be conducted where the results may

be compared with the simulation results from COMSOL. Additionally, data from previous experiments can also be input into COMSOL to perform further analysis.

Reaction models created using COMSOL have been key elements in many recent engineering studies. For example, a study used COMSOL to model the $CO_2$ hydrogenation reaction to produce methanol in a packed-bed reactor [5]. In Adji et al.'s research, the simulation results were compared with experimental data under the same conditions to verify the validity of the model. Model verification is a key aspect one must consider when using COMSOL or any reaction simulation software before using the model for further applications, such as upscaling. This use of COMSOL can be applied to a plethora of chemical reactions. In addition, COMSOL provides a relatively easy approach that can compute the variations of outlet parameters corresponding to a given function and to tentative values of model constants [6]. Using a 2D model, catalytic reactions under unsteady-state conditions that include factors such as heat and mass transfer phenomena were investigated using COMSOL. This was done by measuring how the concentrations of one or more reactants affect the concentration of the products. Overall, the COMSOL Reaction Engineering Module can simulate many different types of reactions and reactor systems. The data derived from these simulations can be used to verify models, perform experiments under various conditions, and design scaled-up reactions.

*1.2. NO Oxidation Reaction*

The study of NO oxidation reaction is important because NO contributes to a wide range of environmental problems such as global warming, acid rain, photochemical smog, and many others [7-9]. Simply stated, it is a harmful gaseous pollutant that society aims to reduce. NO emissions are largely produced from processes of fuel combustions, which is crucial in vehicles and many industries [10, 11]. When exposed to a source of oxygen ($O_2$), NO is oxidized to nitrogen dioxide ($NO_2$) through the following fundamental third order reaction scheme [7, 10, 11]:

$$2NO + O_2 \rightarrow 2NO_2 \tag{1}$$

The rate equation (2) is derived in addition to its intermediate steps by employing the Pseudo Steady State Hypothesis (PSSH):

$$r = -\frac{d[NO]}{dt} = 2k[NO]^2[O_2] \tag{2}$$

where r is the reaction rate, k is the rate constant, t is time, and [NO] and [$O_2$] denote the concentration of nitric oxide and oxygen, respectively.

The integration of Equation 2 results in Equation 3, which can be used to find the concentration of NO at a certain time when k is known or to find k when the other variables are available.

$$\frac{1}{[NO]} - \frac{1}{\{NO]_0} = 2k[O_2]_0 t \tag{3}$$

However, when there is excess oxygen available, NO is the limiting reagent, therefore the reaction can be reduced to a pseudo second order equation [7]:

$$r = 2k'[NO]^2 \tag{4}$$

The product, $NO_2$, is also a harmful pollutant that imposes environmental hazards and can affect human health by causing irreversible damages to the respiratory system [7]. Therefore, much research has been done to investigate the kinetic mechanism of this NO oxidation reaction. With the readily available initial conditions needed to create a simulation model, the feasibility of COMSOL to reproduce previously documented results may be determined. Once significant agreement has been obtained, various parameters (rate constant and initial reactant concentrations) of the simulation can be altered to generate predictive models. Furthermore, deviation analysis between

experimental values and theoretically expected values can be performed by comparing experimental data to previously verified simulated results.

## 2. Methodology/Computational Details

The Chemical Reaction Engineering Module provided by COMSOL Multiphysics was utilized in this research. The Model Wizard was selected with 0 space dimension (0D) and a time dependent study, which led to a constant volume batch reactor. The simulation is computed based on user input parameters specified under Global Definition. This model uses reaction parameters found in published literature as shown in Table 1.

| Fig. | T | k | V | $[NO]_i$ | $[O_2]_i$ |
|---|---|---|---|---|---|
| 1 | 20 | 5590 | 0.4 | $7.36*10^{-6}$ | $1.41*10^{-2}$ |
| 2 | 20 | 5590 | 0.4 | ◇: $7.36*10^{-6}$ | $5.6*10^{-2}$ |
| 2 | 20 | 5590 | 0.4 | □: $8.49*10^{-6}$ | $5.6*10^{-2}$ |
| 2 | 20 | 5590 | 0.4 | △: $1.38*10^{-5}$ | $5.6*10^{-2}$ |
| 3 | 20 | 5590 | 0.4 | $1.38*10^{-5}$ | $5.6*10^{-2}$ |
| 3 | 20 | 1600-9600 | 0.4 | $1.38*10^{-5}$ | $5.6*10^{-2}$ |
| 5a | 25 | 5600 | 3 | $5.0*10^{-4}$ | $1.44*10^{-3}$ |
| 5b | 25 | 7200 | 3 | $5.0*10^{-4}$ | $1.44*10^{-3}$ |
| 5c | 25 | 9600 | 3 | $5.0*10^{-4}$ | $1.44*10^{-3}$ |

T: Temperature (°C)
k: Reaction Rate Constant ($dm^6\ mol^{-2}\ s^{-1}$)
V: Reactor Volume ($dm^3$)
$[NO]_i$: Initial NO Concentration ($mol\ dm^{-3}$)
$[O_2]_i$: Initial $O_2$ Concentration ($mol\ dm^{-3}$)

**Table 1.** Reaction parameters used in COMSOL under ambient conditions. No product present at the beginning of the reaction.

The NO oxidation reaction was input as an irreversible reaction, where the variables of rate constant (k), temperature (T), reactor volume (V), initial concentrations were entered in the respective location. To further enhance the accuracy of the simulation, the thermodynamic properties of the reaction species were specified. The thermodynamic properties of NO and $O_2$ were found in the COMSOL database, whereas the properties of $NO_2$ were user defined using instruction and data provided in the Dissociation in a Tubular Reactor model [12]. The system was assumed to be an ideal gas model.

Once the simulation model was completed by inputting the required reaction parameters, the concentration as a function of time results were studied. The units and length of study was easily adjusted in the Results section. The conversion equation was also conveniently inputted in the Definition section to compute and view the conversion results within COMSOL. Simulation data produced by COMSOL were also exported as Excel files to compile the data and perform further analysis.

## 3. Results and Discussion

### *3.1. Experimental vs. Simulated Results*

The black data points in Figures 1 and 2 were obtained from COMSOL, whereas the colored data points were extracted values from Skalska et al.'s experimental plots.

Using the conditions specified in Table 1, the constant volume batch reactor simulation built in COMSOL produced data that illustrates the progress of the NO oxidation to $NO_2$ shown in Figure 1. The (●) and (■) symbols represent $NO_2$ and NO, respectively. Even though a slight deviation can be seen in the black (simulation) and colored (literature) symbols, there is a good agreement between the simulated and literature data. The same trend is seen in Figure 1 for both simulated and experimental results, suggesting symmetry of NO consumption and $NO_2$ formation, represented by an exponential decrease and increase of NO and $NO_2$, respectively. The graph showed that both lines intersect after approximately 855 seconds at concentrations of

3.8* $10^{-6}$ mol $dm^{-3}$, which indicates that $NO_2$ does not undergo further oxidation.

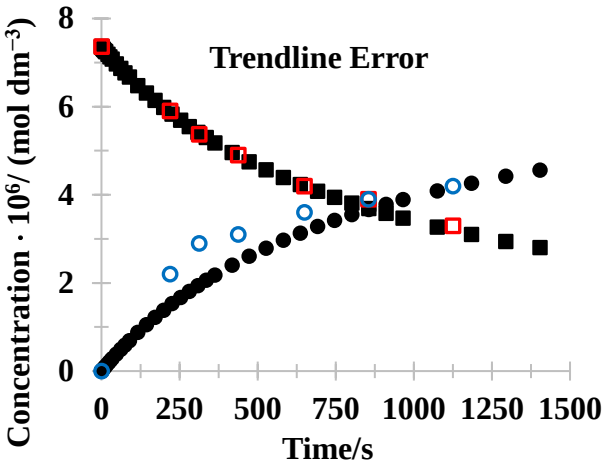


**Figure 1.** Concentration as a function of time using conditions specified in Table 1. $NO_2$ (●) formed as NO (■) was consumed. Black symbols were simulated data, whereas the colored symbols were data points extracted from Skalska et al.

In Figure 2, the initial NO concentrations were altered to observe the rate of change in NO concentration over time in fixed, excess $O_2$ concentration. The initial NO concentrations investigated were (◇) 7.36*$10^{-6}$ mol $dm^{-3}$, (□) 8.49*$10^{-6}$ mol $dm^{-3}$, and (△) 1.38*$10^{-5}$ mol $dm^{-3}$. Other reaction parameters such as temperature, reactor type, rate constant, and reactor volume remained unchanged. Both simulated and experimental data showed the same trend of exponential decrease for all NO concentrations. From the slope of the curves, it can be concluded that for systems which start with a higher initial NO concentration, it will experience a significant increase in the rate of NO consumption. Furthermore, the solid lines in Figure 2 follow the derived elementary rate law equations (Equation 3). The calculated data showed a strong fit with the COMSOL generated plots (black symbols) because the black symbols followed the exact trend line given by Equation 3. Therefore, this indicates the use of Equation 3 in COMSOL's program to simulate the results. Hence, COMSOL is noted as a reliable simulation software that is programmed based on theoretical equations as proven by Figure 2.

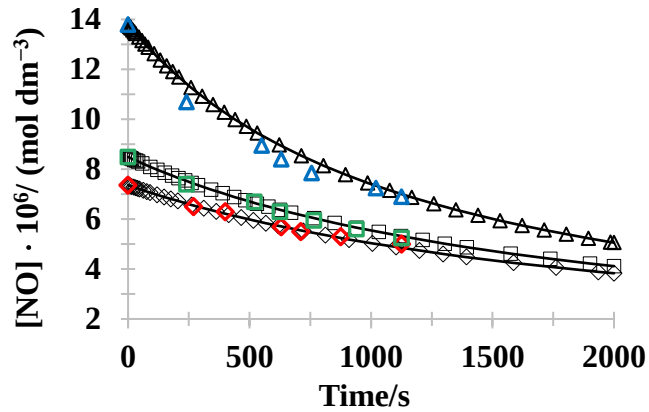


**Figure 2.** NO concentration as a function of time with excess initial $O_2$ concentration and varying initial NO concentrations as listed in Table 1. Solid lines denote theoretical NO concentrations calculated by Equation 3. Colored symbols represent data extracted from Skalska et al.'s plot.

Both Figures 1 and 2 showed identical trends between the experimental and simulated data points, as the data extracted (colored symbols) from Skalska et al.'s paper overlay with the COMSOL generated curves (black symbols). However, the slight deviation between these results could be due to the mismeasurement of extremely small concentrations, contributing greatly to experimental errors. Since the k values in literature were derived from experimentally obtained data, k could be erroneous as proportional to the error in concentration, which would explain the differences observed in Figures 1 and 2. Therefore, the sensitivity of k in the accepted range (1600-14160 $dm^6$ $mol^{-2}$ $s^{-1}$) as stated from previous literature should be determined [7, 10]. Overall, COMSOL's use of theoretical equations encouraged further exploration of the NO oxidation reaction using this built model.

*3.2. Extended Research*

Since various literature data showed a wide range of the rate constants (1600-14160 $dm^6$ $mol^{-2}$ $s^{-1}$), the COMSOL model was used for predictive modelling

to determine the sensitivity of k in this accepted range. Figure 3 displays the simulated data of NO concentration as a function of time in fixed NO and $O_2$ concentrations, while varying a range of k values found from literature. From this plot, the NO concentrations of the various k values at 2000 seconds were noted and plotted into a fitted 3rd order polynomial regression line in Figure 4.

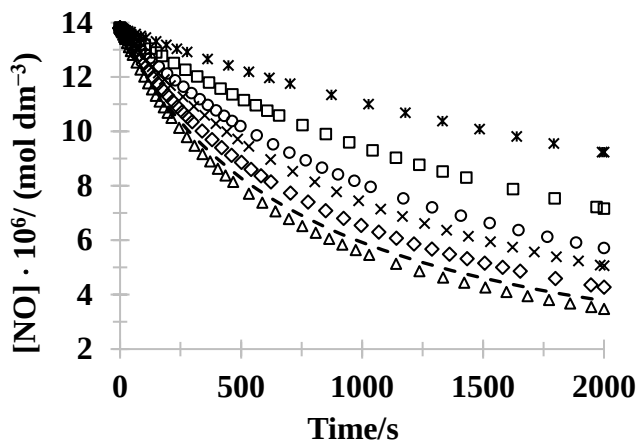


**Figure 3.** Simulated data: NO concentration as a function of time with fixed NO and $O_2$ concentration while varying a range of k values found in literature. k ($dm^6$ $mol^{-2}$ $s^{-1}$): (△) 9600, (-) 8600, (◇) 7200, (x) 5590, (○) 4950, (□) 3000, (*) 1600.

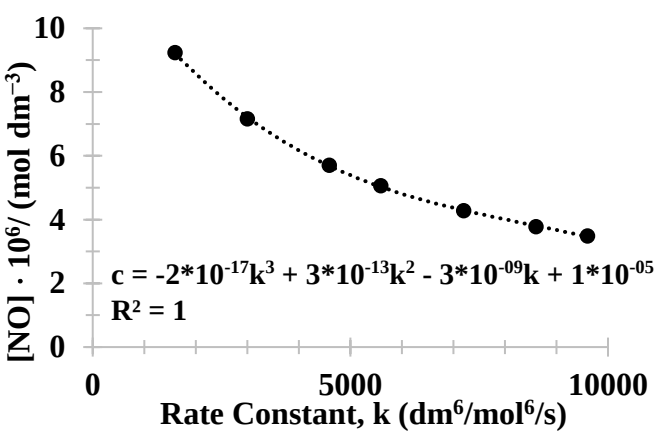


**Figure 4.** NO concentration as a function of rate constant at 2000 seconds, using values from Figure 3. The data were fitted with a 3rd order polynomial regression line.

Figures 3 and 4 indicate that as the value of k increases, its effect on the concentration of NO diminishes. In order to determine the sensitivity of k to the measured reactant concentrations, propagation of error is carried out on the fitted polynomial equation shown in Figure 4. When the cubic term is neglected due to its significantly low value, Equation 4 is obtained, with k representing the rate constant and c representing the reactant (NO) concentration:

$$dc = (6 * 10^{-13}k + 3 * 10^{-9}k)dk \qquad (5)$$

Equation 5 reveals an important and relevant result. For small changes in reactant concentration, the experimentally determined k value can vary greatly. For example, when k = 10,000 $dm^6$ $mol^{-2}$ $s^{-1}$, $dc = (10 * 10^{-8})dk$. This result highlights the importance of accurate experimental concentration measurements when attempting to calculate the rate constant for this reaction. Simulations performed in COMSOL rely on user-input reactant rate constants, so the accuracy of a model and its ability to produce valuable and reliable results is heavily dependent on the quality of the input parameters. Additionally, this result serves as a possible explanation for the large range of reported rate constants for this reaction at 25 °C.

Using the previously generated COMSOL model with constant initial concentrations and varying the input of k, the formation of $NO_2$ concentration as a function of time was explored. The k values that best match the data points extracted from the Smith et al.'s published data were investigated. Figure 5 shows that as k increases, the simulated and experimental curves become more closely matched.

These data from the simulation model suggest that the true rate constant for the reported initial concentration and the resulted [$NO_2$] curve in Smith et al.'s paper is approximately 9600 $dm^6$ $mol^{-2}$ $s^{-1}$, which differs significantly from the reported rate constant of 5600 $dm^6$ $mol^{-2}$ $s^{-1}$. While there is about a 4000 $dm^6$ $mol^{-2}$ $s^{-1}$ difference, the simulated rate constant falls within the reported range of rate constants for the nitric oxide oxidation reaction at 25 °C.

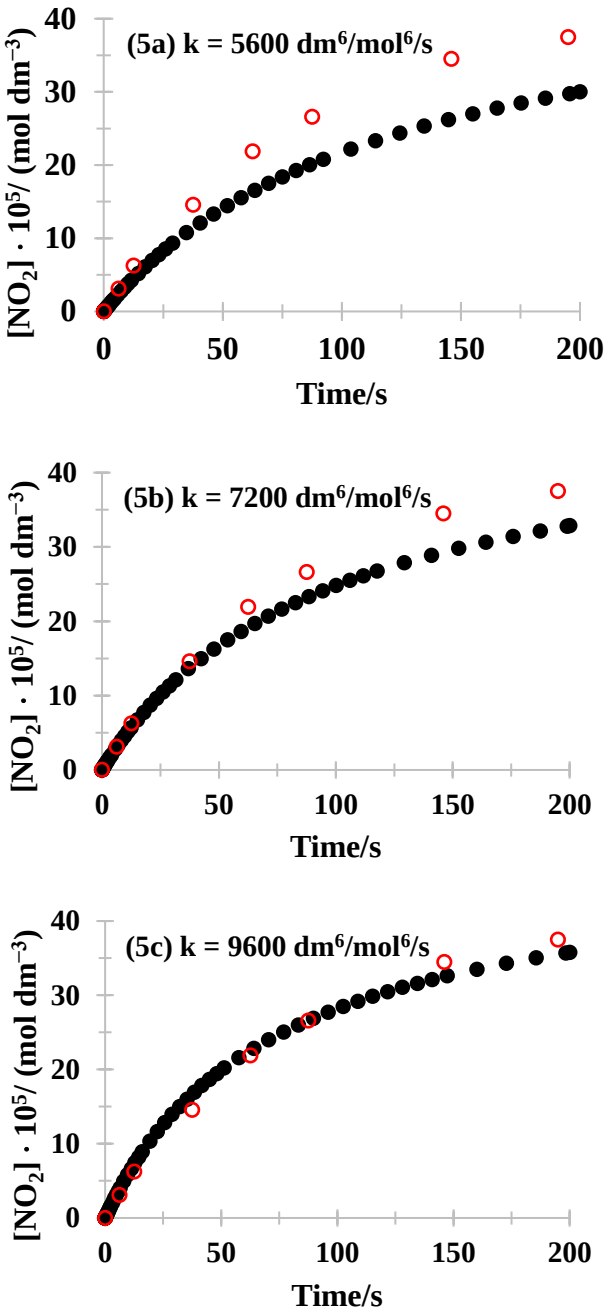


**Figure 5.** Simulated data: $NO_2$ concentration as a function of time with different rate constants for a (k = 5600 $dm^6/mol^6/s$), b (k = 7200 $dm^6/mol^6/s$), and c (k = 9600 $dm^6/mol^6/s$). Red circles are data extracted from Smith et al.'s experimental results.

## 4. Conclusion

Overall, this simulated model of the NO oxidation reaction indicated that COMSOL is a reliable simulation program that generates data based on theoretical equations. Therefore, researchers can avoid working with dangerous, expensive, time consuming, and impractical reaction conditions. The Reaction Engineering Module in COMSOL is a convenient tool when the chemicals used are readily available in the COMSOL database. However, when the chemical requires user-defined information, such as the manual inputs required for $NO_2$, it may lead to some inconveniences. Another shortcoming of COMSOL is its inability to predict completely new reactions, as it requires information such as the reaction rates that can only be experimentally obtained.

Even though there is strong agreement between experimental and simulated data, the slight deviation was possibly due to instrumental errors in measuring extremely low concentration; and since k values in literature were derived from experimentally obtained data, this could explain the discrepancy. The simulated result for a range of rate constant values found in literature showed that as the k value increases, the effect on the concentration of NO diminishes. This type of information is crucial, since COMSOL requires vast amounts of knowledge on the reaction being studied, where precise parameter inputs will determine the success of the simulation. A successful model allows for easy change in parameters (initial concentration, reaction constant, etc.) to conduct further studies on the reaction.

Ideally, a computer simulation is capable of producing/reproducing data from multiple reaction schemes/setups rapidly and with high accuracy. To further explore this reaction using COMSOL, other parameters such as reactor types (continuous stirred-tank reactor (CSTR), plug-flow reactor (PFR), etc.), initial concentrations, and temperature can be altered. Additionally, transport phenomena with different reactor geometries may be investigated in COMSOL's 3D feature.

## 5. Acknowledgements

The authors of this work would like to express appreciation to Dr. Taejin Kim, Dr. Steve Nitodas, and Dr. Miriam Rafailovich for providing us with advice and guidance throughout this research project.

## 6. References

1. COMSOL, "Chemical Reaction Engineering Module User's Guide", (2018).

2. M. Saleh, Y. Muharram, Y.S. Nugroho, Modeling of the crossing point temperature phenomenon in the low-temperature oxidation of coal, International J. Technology, (2017), 1, 104-113

3. H. Nouri, A. Ouederni, Experimental and modeling study of sulfur dioxide oxidation in packed-bed tubular reactor, International J. Innovation and Applied Studies, (2013), 3, 1045-1052

4. A. O. Brezmes, C. Breitkopf, Fast and Reliable Simulations of Argon Inductively Coupled Plasma Using COMSOL, Vacuum, (2015), 116, 65-72.

5. B. S. Adji, S. Kartohardjono, Y. Muharam, "Simulation of Methanol Synthesis from CO2 Hydrogenation in a Packed Bed Reactor using COMSOL Multiphysics", International Journal of Engineering Research and Technology 12 (2019), 2592-2599

6. S. Pietrzyk, F. Dhainaut, A. Khodakov, P. Granger, Catalytic Reactions under Unsteady-State Conditions. Modelling with COMSOL, (2006).

7. K. Skalska, J. Miller, S. Ledakowicz, Kinetics of nitric oxide oxidation, Chem. Pap, 64, 269–272 (2010).

8. C. England, W.H. Corcoran, The Rate and Mechanism of the Air Oxidation of Parts-per-Million Concentrations of Nitric Oxide in the Presence of Water Vapor, Ind. Eng. Chem., Fundam., (1975), 14, 55-63

9. P.G. Ashmore, M.G. Burnett, B.J. Tyler, Reaction of nitric oxide and oxygen, Trans. Faraday Soc., (1962), 58, 685-691

10. E. Neyrolles, J. Lara Cruz, G. Bassil, F. Contamine, P. Cezac and P. Arpentinier, Kinetic study of the nitric oxide oxidation between 288 and 323 K, under pressure, focus on the oxygen influence on the reaction rate constant, International Journal of Chemical Kinetics, (2020), 52, 329-340.

11. J. H. Smith, A Photo-Colorimetric Study of the Oxidation of Nitric Oxide at Low Pressures, J Am Chem Soc. (1943), 65:74-78.

12. COMSOL, "Dissociation in a Tubular Reactor." www.comsol.com/model/dissociation-in-a-tubular-reactor-221.

# Optimization of the MEA in Anion-Exchange Membrane Fuel Cells Using Ag Nanoparticles

Olias Christie [a], Vikash Persaud [a], Isaac Kim [a], Nathan Aragon [a]

[a] *Department of Materials Science and Chemical Engineering, Stony Brook University, Stony Brook, NY 11794, USA*

**Abstract**

Anion-exchange membrane fuel cells or alkaline membrane fuel cells (AEMFCs) are a promising alternative to the existing proton-exchange membrane fuel cells (PEMFCs), which currently lead in overall performance and cost efficiency. AEMFCs can circumvent some of the major downsides present in PEMFCs, which include the use of expensive platinum group metal (PGM) catalysts in the electrodes and CO poisoning. Major developments in AEMFCs revolve around the optimization of the oxidation reduction reaction (ORR) and hydrogen oxidation reaction (HOR) via improvements in the components of the membrane-electrode assembly (MEA). Non-PGM catalysts have the potential to be improved via controlled nanoparticle (NP) dispersion and then implemented into the AEMFCs to achieve the same or greater efficiency as current PEMFC technology. This can be accomplished by coating the membrane of the MEA in the AEMFC with non-PGM nanoparticles to reduce the regions where the anolyte adsorption can degrade the electrodes via the surface effect of the nanoparticles. Instead, a larger region will be maintained on the surface of the membrane which facilitates the catalytic reaction of the HOR and ORR [1-3]. Therefore, we propose that by using different thiol lengths to control the distribution and size of synthesized silver (Ag) nanoparticles that are deposited on the fuel cell membrane, an optimized MEA which utilizes significantly reduced amounts of platinum (Pt) can be developed. In this study, synthesized nanoparticles with thiol lengths of 6 (hexanethiol), 8 (octanethiol) and 10 (decanethiol) carbons are dispersed on a commercial Sustainion membrane via a Langmuir-Blodgett trough at different surface pressures: 2 mN/m, 5 mN/m, and 10 mN/m. The resulting power densities revealed a strong dependence of thiol length (i.e., NP size) and surface pressure (i.e., distance between the particles) on power output. The highest peak power densities were achieved at 10 mN/m, with the highest being C8 at 750.85 mW/cm$^2$ which was 69.4% greater than the power density of the commercial membrane and 25% less than the DoE's desired output of 1 W/cm$^2$.

*Keywords*: anion-exchange membrane fuel cell, silver nanoparticles, Sustainion membrane, membrane electrode assembly, Langmuir-Blodgett method, AEMFCs

## 1. Introduction

AEMFCs are an alternative design to the more common PEMFC which provide a variety of potential benefits such as the minimization of expensive Pt based catalysts and a less acidic environment to circumvent the corrosion of metallic components when compared to PEMFCs. As it stands, there are numerous challenges for AEMFCs to overcome to improve their viability over PEMFCs. Much of the research is focused around

optimizing the ORR and HOR in the MEA of the fuel cell to cut costs, whereas overall improvements in power output and durability remain the chief goals for facilitating the practical implementation of AEMFCs as a source of electricity generation [4]. The reactions which occur in the electrodes of an anionic cell utilizing hydrogen as the fuel have been shown in previous literature to be catalyzed by Ag [5,6]. These reactions are as follows:

**Anode (HOR):** $H_2 + 2OH^- \rightarrow 2H_2O + 2e^-$
**Cathode (ORR):** $O_2 + 2H_2O + 4e^- \rightarrow 4OH^-$

Currently, the Department of Energy (DoE) has set guidelines for the development of PGM-free AEMFCs, as well as goals it hopes to achieve in the coming years. DoE fuel cell test standards include a cell temperature of approximately 80°C and approximately 0.60-0.70 Pt loading on the 5 $cm^2$ electrodes. They aim to achieve a power density greater than 1 $W/cm^2$ and 600 $mA/cm^2$, as well as increased durability of up to 5,000 hours with only a 10% loss in performance [7,8]. To meet these expectations, improvements in the membranes and electrodes are imperative and there has been various developments to this end.

In the past, there has been a strong focus on dispersing different kinds of non-PGM nanoparticles on electrodes to improve power density [9]. Previous literature has also shown promising results from the utilization of carbon supported silver nanoparticles of 5.4 nm with 2-9 nm size distribution on the cathode of the AEM. Anode loading of 0.2 mg $Pt/cm^2$ and cathode loading of 1.0 mg $Ag/cm^2$ produced a power density of 190 $mW/cm^2$ compared to a power density of 247 $mW/cm^2$ for a reference AEM with the same anode loading and a cathode loading of 0.5 $mgPt/cm^2$ [10]. In another study, it was shown that a platinum on multi-walled carbon nanotube catalyst synthesized with dodecanethiol (average particle size, 3 nm) achieved a peak power density of 887 $mW/cm^2$, while the catalyst synthesized with octadecanethiol (average particle size, 2.2 nm) achieved 981 $mW/cm^2$ [11]. However, our novel approach involves coating the membrane in non-PGM nanoparticles as opposed to coating the electrodes and determining the role it plays in relation to power output.

In previous studies by Green et al., it was hypothesized that the substrate is an active participant in catalysis [1-3]. As the anolyte is absorbed to the catalyst support, the activation barrier of the catalytic reaction is depressed due to bond stretching, thereby increasing the efficiency of the catalyst. For this specific reaction, a platelet is the ideal catalyst geometry given that there is enough surface area for the anolyte to adsorb and that the particles are close enough such that the anolyte can migrate to the edge of the particle at the site of catalysis.

In the case of PEMFCs, enhancements in power and durability have been observed upon applying non-PGM nanoparticles onto the electrodes [12]. Analogous to the PEMFCs and the phenomena observed by Green et al., we hypothesize that the addition of non-PGM catalysts to the membrane of an AEMFC may enhance the catalytic activity and consequently increase power output. Here, we propose to synthesize Ag NPs and place them on Langmuir-Blodgett trough films to make platelets that will be lifted onto the anionic membrane. In the model of Green et al., two parameters are of primary importance. The synergy between the NPs and the substrate (i.e., the membrane) and the spacing between the NPs both must be considered. If the spacing between the NPs is too close, there will be insufficient area to facilitate the adsorption of the anolyte material. If the spacing is too far, the anolyte will desorb before it can migrate to the edge of the particle, leading to potential degradation of the catalytic support. Therefore, an optimal distance between the NPs must exist. In order to determine

this optimal region, synthesized nanoparticles with thiol lengths of 6 (hexanethiol), 8 (octanethiol) and 10 (decanethiol) carbons were dispersed on a commercial Sustainion membrane via a Langmuir-Blodgett trough at different surface pressures (2 mN/m, 5 mN/m, and 10 mN/m) to control the nanoparticle size and interparticle distance. To gauge the extent at which the NPs deposited onto the membrane influence the power output of the AEMFC, the power densities of all experimental samples were compared to that of the commercial Sustainion membrane without the addition of NPs.

## 2. Experimental Methods

### *2.1. Synthesis of Thiol-Stabilized Ag Nanoparticles*

The synthesis of thiol-stabilized Ag nanoparticles was conducted via a modified procedure of the two-phase method developed by Brust et al. and implemented in Wang et al. [12, 13]. A 0.028 M solution of silver nitrate ($AgNO_3$) in de-ionized water was reacted with a 0.05 M solution of tetroactlyammonium bromide (TOABr) dissolved in toluene. This solution was stirred for approximately 20 min (i.e., until the all the $Ag^-$ ions were in the organic phase of the solution) after which 200 μL of the desired thiol was added to the two-phase mixture. Then a 0.4 M solution of $NaBH_4$ in distilled water was freshly prepared and added slowly to the previous mixture and stirred vigorously for 3 hours. The organic phase of the solution was separated via filtration and rotary evaporation until 5 mL remained. 200 mL of ethanol was then added to the 5 mL solution, which was then kept at 4°C for approximately 16 hours, upon which a black precipitate formed. The precipitate was washed with ethanol and separated via centrifugation at 5,000 rpm, then dried in a vacuum desiccator for 2 days. This procedure was performed for synthesis of Ag nanoparticles with thiols of length hexanethiol (C6), octanethiol (C8) and decanethiol (C10).

### *2.2. Langmuir-Blodgett Trough Membrane Nanoparticle Deposition*

Similar to the methods implemented in previous studies, a KSV NIMA Langmuir–Blodgett trough from Biolin Scientific, as shown in Figure 1, was used to deposit the thiol-stabilized Ag NP onto a Sustainion membrane via computer control of the surface area [12]. Prior to the deposition of NPs onto the membrane, a 1 mg/mL solution of Ag NPs in toluene was prepared. After initializing the LB trough with a Wilhelmy Platinum Plate (Wetted Length of 39.24 mm) to confirm a surface pressure below 0.25 mN/m, the commercial Sustainion membranes were immersed into the water of the LB trough. A syringe was then used to drop 250 μL of the specific nanoparticle solution onto the water's surface. To ensure the evaporation of the toluene solvent, a 12-minute period was set aside prior to deposition of the NPs onto the membrane. After evaporation of the solvent, the trough barriers were set to compress the NPs on the water surface at 10 mm/min until the target surface pressure was achieved. The Sustainion membrane was then lifted at a speed of 2 mm/min to deposit the Ag NPs at the target surface pressure onto the membrane. Target surface pressures of 2 mN/m, 5 mN/m and 10 mN/m were used to deposit Ag NP (C6, C8, and C10) films onto the membranes.

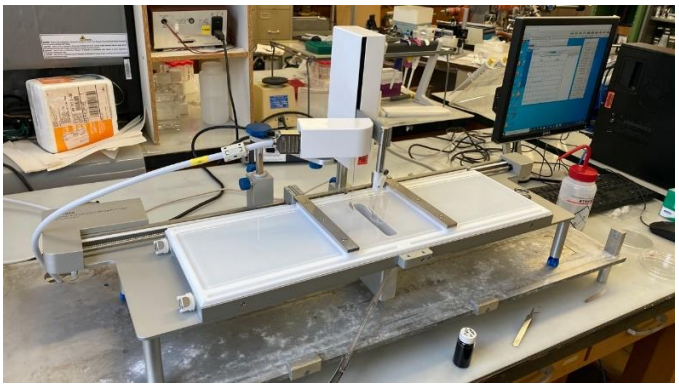

**Figure 1.** Langmuir-Blodgett trough experimental setup.

*2.3. Nanoparticle Characterization*

TEM samples were prepared during the LB process by immersing holey carbon TEM grids into the water subphase and lifting at the appropriate surface pressure intervals to collect Ag nanoparticles. The TEM grids were imaged at an acceleration voltage of 120 kV on a JEOL 1400 microscope similar to the methods in Wang et al. [12]. The TEM images for the various nanoparticles taken at 200 nm were analyzed using ImageJ with a ND plugin to determine average nanoparticle size distributions and interparticle distances. Images were taken after LB trough deposition at surface pressures of 2 mN/m, 5 mN/m and 10 mN/m to determine any morphological changes as a result.

*2.4. MEA Fabrication and Fuel Cell Tests*

A custom made SFC-TS Fuel Cell Technologies Inc. test bench was used to obtain polarization and power density curves from the fabricated membranes. Two 5 $cm^2$ Pt/C electrodes were sprayed with additional Pt in solution to achieve a Pt loading of 0.76 $mg/cm^2$ for use as the cathode and anode. The fuel cell MEA was assembled with the commercial Sustainion membrane between the two electrodes. The fabricated membrane with the Ag NP film deposited on its surface was pre-soaked with KOH for 1 hour prior to testing. Single cell tests were run with relative humidity set to 100%, cell temperature set to 60°C and electrode temperatures set to 58°C on the fuel cell test bench. Pure $H_2$ and $O_2$ gas were fed to the anode and cathode in a 1.5 to 3.0 stoichiometric ratio, respectively ($H_2$ at 500 ccm, $O_2$ at 1000 ccm). Software from LabVIEW was used to monitor and control the gas flow rates and obtain electricity results. Figure 2 details the fuel cell test bench with the MEA assembly. Tests were run for each nanoparticle sample and polarization and power density curves were obtained.

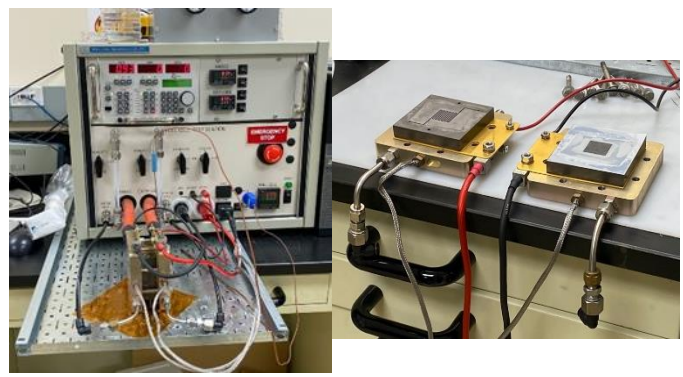

**Figure 2.** Fuel Cell test bench setup (left) and membrane electrode assembly (right).

## 3. Results and Discussion

*3.1. Ag Nanoparticles: Size Distribution and Interparticle Spacing*

To produce membranes uniformly coated with Ag nanoparticles, the LB method was implemented to assemble a Ag NP monolayer at the air-water interface. Surface tension facilitates the transfer of the particles onto the membrane, and the interparticle distance can be accurately controlled based on the surface pressure at which it is lifted. From the TEM images, the morphology of the Ag NPs was observed and assessed for the occurrence of agglomerations. The expected morphological structure of the NPs is of a spherical shape and an adequate particle density should be obtained. The diameters and interparticle

distances in Table 1 are shown to be in agreement with what is observed in the TEM images in Figure 3. Overall, the observed trend is that as the surface pressure increased, the interparticle spacing increased as well with no effect on the particle diameter. However, in the case of C8 at 5 mN/m there was a spike in the diameter and interparticle distance which may be attributed to the agglomeration of NPs. For the sample C10 at 5 mN/m, the resulting diameters and interparticle distances were smaller than the other C10 samples at 2 mN/m and 10 mN/m which can be attributed to an error in the lift off procedure for the TEM grids. As a result, the expected trends relating surface pressure and interparticle distance of the samples are not seen. However, their correlation to the power outputs that are observed in the power density curves (Figures 4-6) provide an accurate representation of the relationship of nanoparticle size and surface pressure to power output.

**Table 1.** Nanoparticle diameter and interparticle distance for C6, C8 and C10 at 2 mN/m, 5 mN/m and 10 mN/m.

| | **Diameter (nm)** | | | **Interparticle Distance (nm)** | | |
|---|---|---|---|---|---|---|
| **Π (mN/m)** | **C6** | **C8** | **C10** | **C6** | **C8** | **C10** |
| **2** | 4.1 ± 1.3 | 2.6 ± 0.2 | 3.9 ± 0.2 | 6.8 ± 1.3 | 5.4 ± 0.4 | 6.1 ± 0.3 |
| **5** | 2.9 ± 0.1 | 6.8 ± 3.2 | 2.2 ± 0.3 | 8.6 ± 0.5 | 11.4 ± 1.7 | 4.8 ± 0.2 |
| **10** | 2.9 ± 0.5 | 2.6 ± 0.3 | 3.9 ± 0.2 | 9.2 ± 0.6 | 6.5 ± 0.6 | 6.7 ± 0.9 |

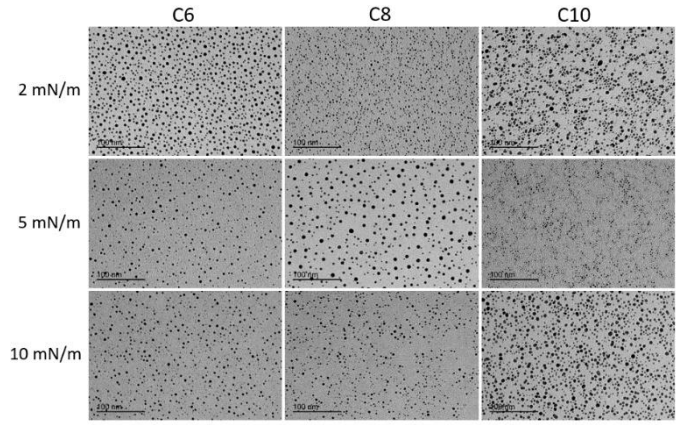


**Figure 3.** TEM micrographs of synthesized Ag nanoparticles at 100 nm for C6 at 2 mN/m, 5 mN/m and 10 mN/m, C8 at 2 mN/m, 5 mN/m and 10 mN/m, and C10 at 2 mN/m, 5 mN/m and 10 mN/m.

*3.2. Fuel Cell Test*

To assess the impact of interparticle distance on the Sustainion membrane anion transport and its resulting fuel cell power output, MEAs (5 $cm^2$) were prepared and tested at various surface pressures for each of the Ag NP samples and compared to that of a commercial Sustainion membrane without the addition of NPs. From Figure 4, increased power outputs were observed for all samples at 2 mN/m compared to the control; the peak power density for the control in all cases was observed to be 443.28 $mW/cm^2$. At 2 mN/m, the peak power density was achieved for C6 at 557.40 $mW/cm^2$ which equates to a 25.7% increase over the commercial membrane. When the fuel cell tests were performed for the Ag NP samples at 5 mN/m, the effect of sample integrity on power output became quite prominent. As seen in Figure 5, the power density for C6 had steadily increased by 5%, whereas C8 and C10 had decreased drastically by 21% and 10%, respectively. Despite these changes in power densities, the power outputs for C6 and C10 at 5 mN/m remained greater than that of the commercial membrane, however the C8 sample was observed to drop slightly below that of the control by 3.5%. At 5 mN/m, the peak power

density was achieved for C6 at 584.12 mW/cm$^2$, which is attributed to a 31.8% increase over the commercial membrane. During the last iteration of fuel cell tests at 10 mN/m, an overall increase in power outputs were observed again for all samples compared to the control (Figure 6). Here, the maximum power output increase across all samples was achieved by C8 at 750.85 mW/cm$^2$, followed by C6 at 624.90 mW/cm$^2$, and finally C10 at 608.52 mW/cm. This maximum increase in power density observed by the C8 sample resulted in an overall 69.4 % increase in power output over the commercial membrane.

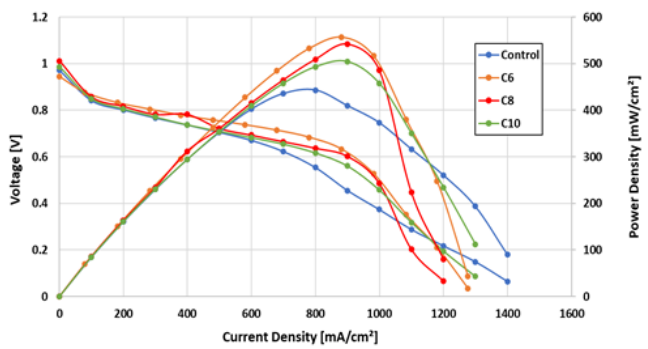


**Figure 4.** Power density and polarization curves for a commercial Sustainion membrane without Ag NPs and for Ag NPs deposited onto the Sustainion membrane at 2 mN/m.

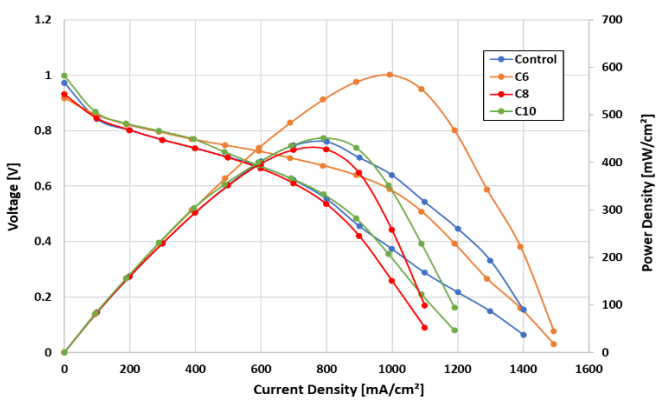


**Figure 5.** Power density and polarization curves for a commercial Sustainion membrane without Ag NPs and for Ag NPs deposited onto the Sustainion membrane at 5 mN/m.

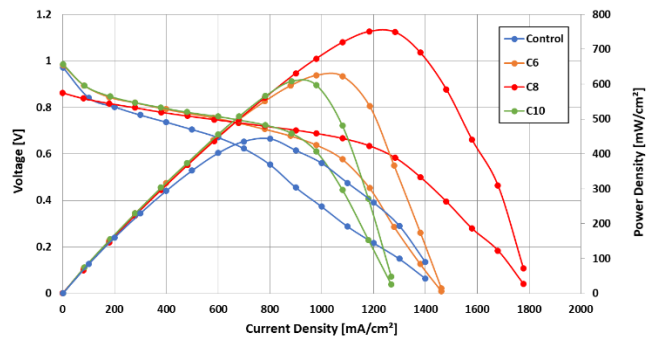


**Figure 6.** Power density and polarization curves for a commercial Sustainion membrane without Ag NPs and for Ag NPs deposited onto the Sustainion membrane at 10 mN/m.

The data presented in Figures 7 and 8 display the overall effects of surface pressure and thiol length on the peak power densities achieved. The expected trend is apparent in the figures despite dips in power at 5 mN/m which, as previously stated, may be attributed to lift off error in the coating of the membranes or nanoparticle agglomeration. For C8 at 5 mN/m, larger sized particles of maximum size 10 nm and large interparticle distances of 13.1 nm are seen in Figure 3 and Table 1 which naturally correlate to a low power density as expected. TEM images for C10 at 5 mN/m displayed particles that were disrupted due to the error in lift off procedure thus resulting in a lower power density. This indicates that the power output of the fuel cells is sensitive to the quality of the NP samples placed on the membrane. For C8 at 10 mN/m, the particles size was among the smallest being at a maximum of 2.3 nm, and also had a relatively small interparticle distance at approximately 6.5 nm. Nevertheless, the NP size and interparticle distances seen in the TEM images and Table 1 reflect the expected trends overall, with samples that include smaller sized particles and higher particle densities resulting in the greatest peak power densities overall. As shown in Figure 5, C8 at 5 mN/m had the lowest power density due to the aforementioned circumstances, and C8 at

10 mN/m performed the best as it had a much smaller average particle size and shorter, uniform interparticle distances. Therefore, a clear correlation of the effect of particle size and interparticle distance on power density was shown and is represented in Figure 7. These results prove the hypotheses predicted by Green et al., as the substantial increase in power output indicates that with high-quality particles in intimate contact, there exists an optimal region between the particles that will effectively facilitate anolyte adsorption. To improve upon this study, increasing the number of trials for the fuel cell testing should be implemented to provide a statistical significance to the results.

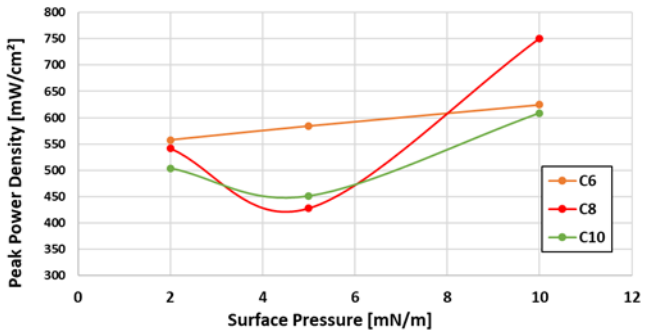


**Figure 7.** Comparison of corresponding peak power densities for AEMFCs with thiol-stabilized Ag NP coated membranes at increasing surface pressures.

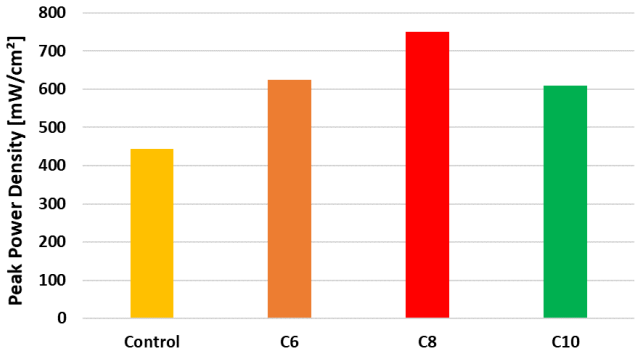


**Figure 8.** Comparison of maximum power outputs observed for each thiol length Ag nanoparticle compared to the control commercial Sustainion membrane without nanoparticles.

*3.3. Surface Phenomenon Hypothesis Validation*

To validate the synergistic effects between the membrane and the catalytic efficiency as predicted by Green et. al., it is important to determine whether the increase in power density is a result from an increase in the number of nanoparticles within the system, an increase in surface compression, or a membrane effect which contributes to the efficiency of the catalytic reaction. Regarding the potential dependence of power output on the number of particles, it was determined separately that at a surface pressure of 5 mN/m, 10 µg of C6 NPs had been deposited onto the Sustainion membrane. Given that there is a baseline of 3.8 mg of Pt on the electrodes of the fuel cell, incorporating 10 µg of Ag NPs into this system would account for a 0.3% increase in the total number of nanoparticles within the system. If it were the case that a direct relationship exists between the power output of the fuel cell and the number of nanoparticles within the system, then theoretically there should have been only a 0.3% increase in the power density for C6 at 5 mN/m. However, this was clearly not the case given that a 31.8% increase in power density was observed for C6 at this surface pressure. Additionally, this drastic increase in power output cannot simply be attributed to the catalytic behavior associated with Ag NPs since it is well known that Pt is a more efficient catalyst for the HOR and ORR reactions [5]. In regards to the potential dependence of power output on surface compression, the fuel cell test for the C10 sample was repeated with the NPs sprayed onto the membrane (in an amount estimated to be proportional to the particle density after being exposed to a surface pressure of 10 mN/m) as opposed to being coated using the LB trough. Under the assumption that there will be more Ag NPs on the membrane at 10 mN/m as opposed to 5 mN/m, 20 µg of C10 NPs were sprayed onto both sides of the membrane. If it were the case that the power output

was directly proportional to the surface pressure that the NPs were subjected to, then the expected power density for the C10 NPs sprayed onto the membrane should have been lower than that of C10 NPs that were deposited onto the membrane at 10 mN/m. However, as demonstrated in Figure 9, this was unsubstantiated as there was only a 2% difference in power density that was observed between the two tested samples. Therefore, these tests further support the predictions of Green et al. in regards to the membrane having a synergistic effect on efficiency of the HOR and ORR catalytic reaction.

The fuel cell test of the C10 sample being sprayed onto the membrane as opposed to being coated using the LB trough was also applied to confirm the dependence of power output on the geometry of the NPs. It was expected that the NPs platelet geometry consequent of using the LB trough would provide a greater power output in accordance with the effects predicted by Green et. Al. However, from the spray test seen in Figure 9, it was revealed that there was only a 2% difference in power density as a result of using the LB trough. It should be noted however, that the platelet geometry is assumed to have formed via the LB trough process. The TEM images alone are not enough to validate the actual geometry of the NPs, so further testing is required in order to confirm the formation of platelets. Despite this shortcoming, a platelet geometry was deemed unnecessary and an alternative optimal procedure to apply NPs onto the membrane can be determined in a future study.

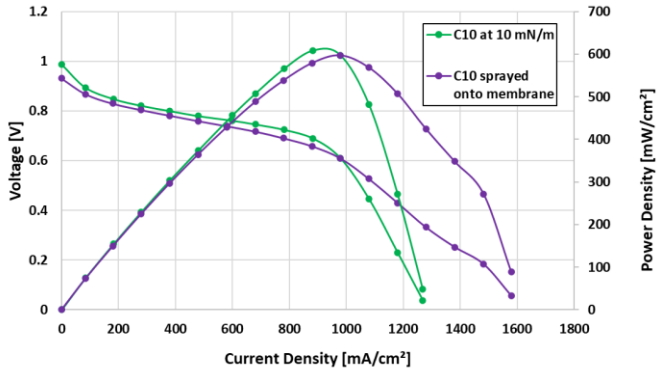


**Figure 9.** Comparison of the power density and polarization curves for C10 Ag NPs sprayed onto the Sustainion membrane as opposed to coating the membrane using the LB trough for C10 at 10 mN/m.

## 4. Conclusion

We have shown that Ag NPs placed directly on the membrane in an AEMFC can enhance the power output by up to 69.4%, which is ~75% of the desired standard output set by the DoE. A strong dependence of thiol length (i.e., NP size) and surface pressure (i.e., distance between the particles) on power output have been observed as predicted by Green et al. It was also demonstrated that an increase in power density is a surface phenomenon between the particles and the membrane, however an additional study is required to determine the aspect ratio of the particles. Furthermore, increasing the number of trials for all tests, increasing the surface pressure that the NPs were subjected to beyond 10 mN/m, as well as performing the validation tests for the Green et. al. predictions for various particle parameters are warranted to implement statistical analysis and provide a statistical significance to the results of this study. Future work must also be conducted to determine the mechanism by which the membrane operates and further confirm whether the mechanism predicted by Green et al. is truly in effect. Performing FIB electron microscopy will allow us to validate whether surface pressure is causing the nanoparticles to split apart and determine if an optimum surface

pressure exist. Additional tests, such as cyclic voltammetry, may be performed to analyze degradation of the MEA and assess whether the AEMFC meets the desired requirements set by the DoE. Ag alloys may be synthesized to protect the Ag from degradation and stabilize it to improve AEMFC durability. Lastly, Density Functional Theory (DFT) calculations can predict the effects of alloys, followed by durability testing to validate theoretical assumptions and confirm results.

## 5. Acknowledgements

We would like to thank Aniket Raut and Haoyan Fang for their guidance throughout this project, as well as Dr. Miriam Rafailovich for her mentorship. This research was supported by the Stony Brook Department of Materials Science and Chemical Engineering.

## 6. References

1. Green, I. X.; Tang, W.; Neurock, M.; Yates, J. T., Jr. Spectroscopic Observation of Dual Catalytic Sites during Oxidation of CO on a Au/$TiO_2$ Catalyst. *Science* **2011**, *333* (6043), 736–739.

2. Green, I. X.; Tang, W.; Neurock, M.; Yates, J. T., Jr. Insights into Catalytic Oxidation at the Au/TiO(2) Dual Perimeter Sites. *Acc. Chem. Res.* **2014**, *47* (3), 805–815.

3. Green, I. X.; Tang, W.; McEntee, M.; Neurock, M.; Yates, J. T., Jr. Inhibition at Perimeter Sites of Au/TiO2 Oxidation Catalyst by Reactant Oxygen. *J. Am. Chem. Soc.* **2012**, *134* (30), 12717–12723.

4. Gottesfeld, S.; Dekel, D. R.; Page, M.; Bae, C.; Yan, Y.; Zelenay, P.; Kim, Y. S. Anion Exchange Membrane Fuel Cells: Current Status and Remaining Challenges. *J. Power Sources* **2018**, *375*, 170–184.

5. Firouzjaie, H. A.; Mustain, W. E. Catalytic Advantages, Challenges, and Priorities in Alkaline Membrane Fuel Cells. *ACS Catal.* **2020**, *10* (1), 225–234.

6. Davydova, E. S.; Mukerjee, S.; Jaouen, F.; Dekel, D. R. Electrocatalysts for Hydrogen Oxidation Reaction in Alkaline Electrolytes. *ACS Catal.* **2018**, *8* (7), 6665–6690.

7. Hickner, M. A. Advanced anion exchange membranes with tunable water transport for platinum-group-metal-free anion exchange membrane fuel cells https://www.hydrogen.energy.gov/pdfs/progress19/fc_fc308_hickner_2019.pdf (accessed Mar 10, 2021).

8. Mustain, W. E.; Chatenet, M.; Page, M.; Kim, Y. S. Durability Challenges of Anion Exchange Membrane Fuel Cells. *Energy Environ. Sci.* **2020**. https://doi.org/10.1039/d0ee01133a.

9. Omasta, T. J.; Peng, X.; Miller, H. A.; Vizza, F.; Wang, L.; Varcoe, J. R.; Dekel, D. R.; Mustain, W. E. Beyond 1.0 W Cm−2Performance without Platinum: The Beginning of a New Era in Anion Exchange Membrane Fuel Cells. *J. Electrochem. Soc.* **2018**, *165* (15), J3039–J3044.

10. Xin, L., Zhang, Z., Wang, Z., Qi, J., & Li, W. (2013). Carbon supported Ag nanoparticles as high performance cathode catalyst for H2/O2 anion exchange membrane fuel cell. *Frontiers in chemistry*, *1*, 16. https://doi.org/10.3389/fchem.2013.00016.

11. Liu, X.; Villacorta, R.; Adame, A.; Kannan, A. M. Comparison of Pt/MWCNTs Nanocatalysts Synthesis Processes for Proton Exchange Membrane Fuel Cells. *Int. J. Hydrogen Energy* **2011**, *36* (17), 10877–10883.

12. Wang, L.; Zhou, Y.; Yang, Y.; Subramanian, A.; Kisslinger, K.; Zuo, X.; Chuang, Y.-C.; Yin, Y.; Nam, C.-Y.; Rafailovich, M. H. Suppression of Carbon Monoxide Poisoning in Proton Exchange Membrane Fuel Cells via Gold Nanoparticle/Titania Ultrathin Film Heterogeneous Catalysts. *ACS Appl. Energy Mater.* **2019**, *2* (5), 3479–3487.

13. Brust, M.; Walker, M.; Bethell, D.; Schiffrin, D. J.; Whyman, R. Synthesis of Thiol-Derivatised Gold Nanoparticles in a Two-Phase Liquid-Liquid System. J. Chem. Soc., Chem. Commun. 1994, 0, 801− 802.

# DNA Adsorption Onto PDMS and Transferal via Stamping to PAA – Preliminary Steps Toward an Ordered Fragmentation Method for Next Generation Sequencing

Austin Mohr [a]

[a] *Department of Materials Science and Chemical Engineering, Stony Brook University, Stony Brook, NY 11794, USA*

**Abstract**

Difficulty in determining the original order of DNA fragments generated from genomic DNA for Next Generation Sequencing (NGS) clonal template library preparation is a problem that often leads to errors during NGS and an inability to sequence repetitive genomic regions. Accordingly, the development of a fragmentation method that preserves information about fragments' long-range positional order in genomic DNA is warranted [1]. Fragmentation via transposases that can simultaneously fragment and label DNA ("tagmentation") not only with NGS adaptors and indices but also with information about original positional order is a potential solution. In preliminary steps toward the development of such a method, several solutions composed of λ-DNA and NaCl in tris-ethylenediaminetetraacetic acid (TE) buffer were prepared and used for testing DNA adsorption onto polydimethylsiloxane (PDMS, a proposed substrate for transposase attachment) via a timed, dip and slow withdrawal method using a customized apparatus equipped with a stepping motor. DNA adsorption onto PDMS was confirmed by fluorescence microscopy, with maximum DNA density found using a 6.25 μg/ml λ, 100 mM NaCl solution, while optimal densities for DNA library preparation were found using lower DNA concentrations. Variations in the linearity and uniformity of DNA stretching in numerous trials was observed and attributed, in part, to PDMS surface effects. Subsequent transferal of DNA from PDMS to a Si wafer coated with polyacrylic acid (PAA, a proposed surface for transposase activation), and successful desorption of DNA from the PAA were also confirmed by fluorescence microscopy in numerous trials.

*Keywords:* NGS, next-generation sequencing, DNA, adsorption, PAA, PDMS, tagmentation

## 1. Introduction

The celebrated and well-known Human Genome Project (HGP) is a landmark in the science of genetics. Begun in 1990 and completed in 2003 at a total cost of USD $3 billion [2], the HGP was a massive, international, cross-disciplinary effort to map and sequence the human genome. It involved hundreds of scientists and mathematicians and numerous institutions, and culminated in the creation of the first human reference genome.

Contrary to a widespread misconception, the HGP did not produce a complete reference genome. The early reference contained numerous gaps. In particular, highly repetitive chromosomal regions (the so-called, "repeatome") proved intractable to the sequencing methods in existence at the time. (DNA sequencing for the HGP was performed using a scaled-up version of the Sanger method, with numerous parallel capillary tubes employed for gel electrophoresis and radioactive or fluorescent labeling to identify base pairs incorporated by a polymerase.) In subsequent years, advances in sequencing technology and bioinformatics would lead to growth in the corpus of knowledge of human

genetics such that the latest human genome reference, GRCh38, contains fewer than 1000 gaps [3].

Despite these improvements, the repeatome has still not been comprehensively sequenced and, more problematically, the DNA used to create GRCh38 comes from just 20 donors, with over 70% coming from a single "individual who had a high risk of diabetes" [3]. Consequently, the reference does not sufficiently capture the allelic or, more generally, the genomic diversity of the human population. One of the primary applications of the reference is in analysis of reads obtained when sequencing an individual's DNA; as a result, the reference's deficiencies contribute, in part, to difficulty in identifying variations that may occur in DNA on an individual basis, such as structural variations (SVs). However, such information is of relevance from a medical standpoint: among the SVs that have been identified, many have been shown to be pathogenic [3]. Moreover, the repeatome has also been shown to play a role in disease, and is known to be mutation prone [4], factors which compound the problem.

In short, limitations in the present state of the art of DNA sequencing technology have led to deficiencies in reference genomes and the related problem of deficiencies in sequencing individual DNA (since individual sequencing both entails many of the same challenges as compiling a reference, as well as the aforementioned comparison to the reference as an inherent part of the sequencing process). Superior sequencing technology leading to a truly comprehensive genomic reference (both lacking gaps and representative of human genomic diversity) and the ability to rapidly, accurately, and affordably sequence individuals' genomes will, in turn, lead to the development of universal, genetically-tailored medicine, which promises to be a formidable tool in the prevention, diagnosis, and treatment of disease. Moreover, such technology would more generally contribute to our understanding of genetic phenomena such as the specific functionality of individual genomic elements, proteomics [2], and epigenetics.

Since their introduction approximately 13 years ago, the various high-throughput DNA sequencing technologies known by the umbrella term, "Next-generation sequencing," (NGS) have led to vast improvements in the speed and massive reductions in the cost of DNA sequencing relative to the older, low-throughput, and expensive Sanger method, and are responsible for advances toward the development of individualized sequencing and the improvements in genomic references discussed previously [5]. However, all NGS technologies entail a complex DNA clonal template library preparation process, still produce error rates as high as 15% [5], and are limited to short, 10-15 kbp read lengths (or less), making DNA fragmentation a prerequisite for their use [6]. Errors during NGS include incorrect nucleotide substitution, cross-talk stemming from overlapping of absorption and emission spectra (amongst either adjacent nucleotides or adjacent clusters), dimming of fluorescent readouts, and phasing (unsynchronized sequencing within a cluster) [7]; these problems can originate during any step of the NGS workflow (e.g., as a result of DNA damage) [8].

The comparatively huge size of human chromosomes (47-249 Mbp) relative to NGS read lengths leads to the difficulty sequencing repetitive regions (whence, in part, the gaps in the reference genome), and problems such as the inability to distinguish genes from pseudogenes [9]. Furthermore, of special relevance to individual genomic sequencing, the short read lengths lead to the difficulties identifying SVs and performing haplotype phasing [9]. Complex data analysis, computational methods, and bioinformatics work utilizing the reference genomes are required to attempt *de novo* genomic DNA reassembly using NGS [5,6], and the process is failure prone (see Fig.1).

1. Library preparation.

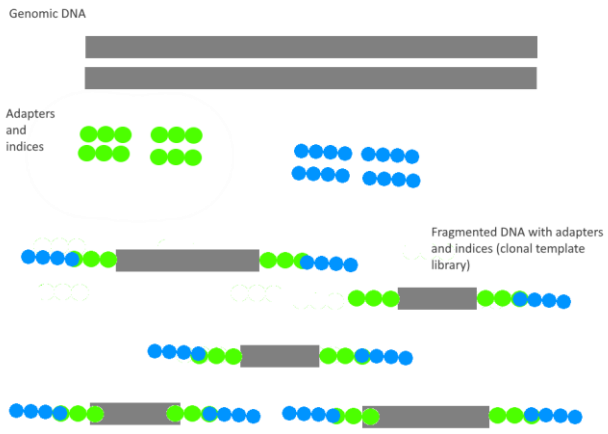


2. Cluster amplification.

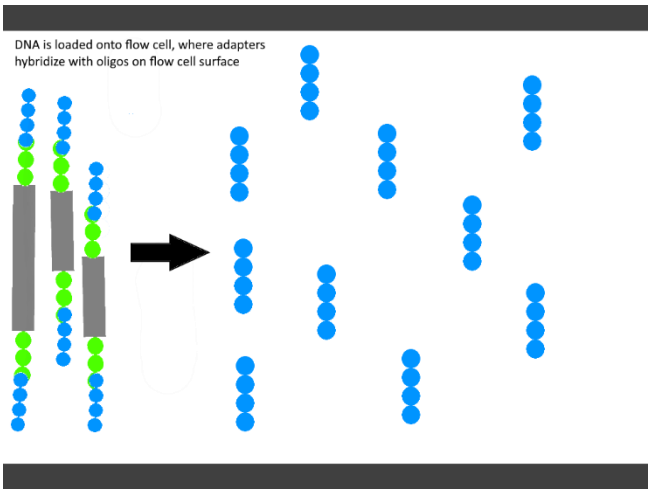


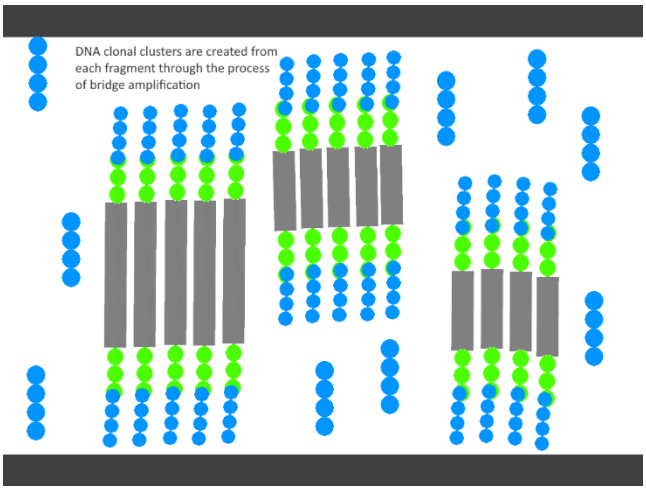


3. Sequencing.

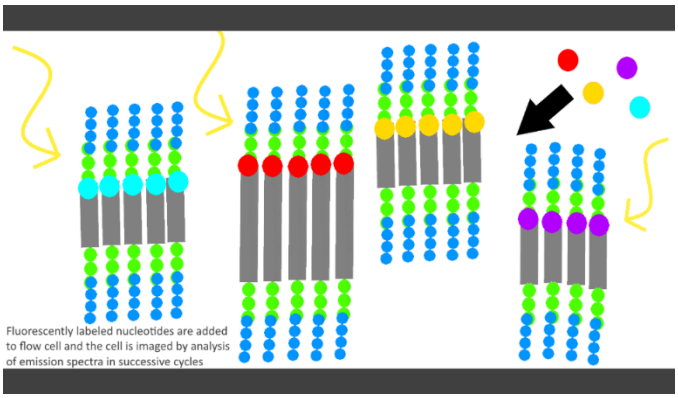


4. Data analysis:

In the data analysis step, reads are compared to the reference genome:

**Reads:**

ATGGCATTGCAATTTGACT
GCAATTTGAC
GGCATTGC
CATTGCAAT
TGCAATTT
ATGGCATTG
GGCATTGC

**Reference:**

AGATGGTATTGCAATTTGACAT

Fig. 1 NGS – Sequencing by synthesis (SBS) via the Illumina platform is one of the most widely used NGS technologies. DNA is first fragmented and adaptors and indices are attached. Next, DNA is loaded onto a flow cell carrying a “lawn” of oligonucleotides that bind to the adaptors on the fragments. Bridge amplification (a variation of PCR) is performed, ultimately leading to strands which are then sequenced as fluorescently-labeled, dideoxynucleotides are incorporated by DNA polymerase, the sample is imaged, and incorporated base pairs are identified by emission spectra. At the end of each imaging cycle, the labels are removed, the hydroxide groups on dideoxynucleotides are restored, and elongation is continued. After completion of sequencing, reads (many of which are redundant / overlapping, as depicted) are compared to a reference genome. The method lacks an effective way of determining where the fragments came from within genomic DNA if they cannot be reconciled during alignment and data analysis. This is especially problematic when sequencing DNA from the repeatome, dealing with fragments derived from regions containing SVs or pseudogenes, or attempting to perform haplotype identification.

A fundamental challenge inherent in NGS is loss of awareness of the spatial-relatedness of the numerous DNA fragments created during the preliminary fragmentation of genomic DNA. The problem of piecing together millions of amplified DNA fragments might be likened to trying to solve a jigsaw puzzle with only one specific solution (the original genome), but millions of pieces that are either indistinguishable (e.g., if they are fragments from the repeatome), unidentifiable (if they are fragments corresponding to regions containing SVs or pseudogenes, or are otherwise unable to be reconciled to the reference), too numerous (e.g., if a certain starting fragment was over amplified due to bias), or simply absent (e.g., if a certain starting fragment was insufficiently amplified). Accordingly, the objective of this work is to contribute to the development of an improved NGS DNA library preparation method which is simple to perform, affordable, and contributes to error reduction and process streamlining by preserving information about the spatial-relatedness of DNA fragments via an ordered fragmentation process.

Sokolov et.al. have previously demonstrated that DNA immobilization on a polymethyl methacrylate (PMMA) coated silicon wafer [1,6] and subsequent fragmentation by targeted delivery of the DNA-cleaving enzyme DNase I with a lithographically-patterned stamp of polydimethylsiloxane (PDMS) or reservoir apparatus with microfluidic channels for DNase I delivery [1] are plausible. However, fragmentation by an enzymatic method precludes labeling or barcoding of the fragments in a manner facilitating the preservation of their long-range positional order in genomic DNA. Benke, et. al. investigated DNA adsorption on PDMS and proposed a phenomenological model to describe it [10]. Inspired, in part, by this work, it is hypothesized that DNA can be immobilized on a solid, lithographically-patterned substrate (PDMS) for transposase attachment and subsequently transferred via stamping to a poly-acrylic acid (PAA) coated silicon wafer (a suitable surface for transposase activation), before, finally, being removed by desorption for NGS. PDMS is an ideal substrate for such an application as it has been demonstrated that it can be used for immobilization and linear, uniform stretching of DNA [10]. PDMS is also readily patternable by soft-lithography, which may facilitate transposase attachment: if DNA is adsorbed on PDMS perpendicular to grooves created on the PDMS by soft-lithography, it is possible that transposases can be attached to the DNA by introducing a solution containing them via microfluidic flow through the grooves. PAA, on the other hand, has not been demonstrated to be effective for linear, uniform stretching of adsorbed DNA, but it possesses useful properties such as reversible solubility in water [11], which may be exploitable for activation of transposases and easy DNA desorption. Accordingly, the primary objective of the work reported here was to demonstrate the feasibility of a DNA adsorption, stamping, and desorption procedure using surfaces without a pattern as preliminary steps toward confirming this hypothesis.

## 2. Experimental Methods

### *2.1 Preparation of PDMS Stamps*

Sylgard 184 (PDMS, Dow Corning) and curing agent were thoroughly mixed in a ten to one ratio by weight, respectively, and approximately 8 g of the resulting mixture were transferred to a Petri dish (Sarstedt 83.3902) and vigorously mixed with a disposable plastic stirrer for approximately ten minutes. Most air bubbles resulting from the incipient curing process were permitted to rise from the mixture, after which the dish was transferred to a vacuum desiccator to eliminate any remaining bubbles and, finally, placed on heater and left to cure for four hours at 65° C. The resulting solid, circular piece of PDMS was then removed from the Petri dish and carefully cut into rectangles of approximately one centimeter squared total area using a razor blade.

The stamps were then transferred to a custom machined, Teflon tray that had been previously subjected to ultrasonic cleaning in DI water and soaked in ethanol (Pharmco 111000200, 200 proof) overnight, after which they were again subjected to vacuum desiccation overnight to remove the ethanol.

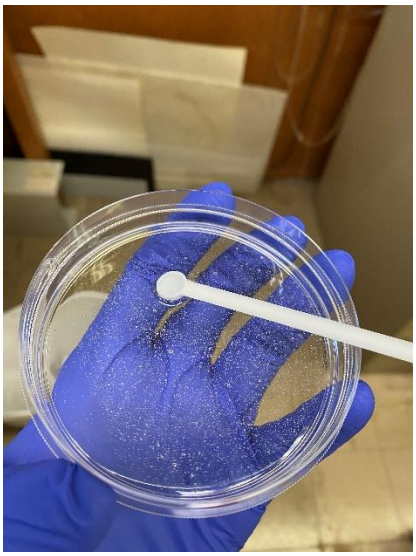

**Figure 2**. PDMS stirring in Petri dish during curing

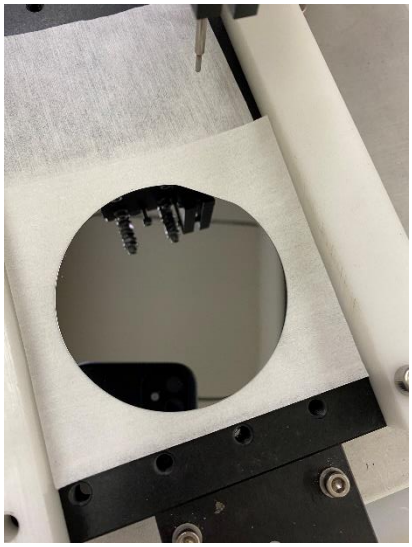

**Figure 3**. Silicon wafer, prior to coating

*2.2 Preparation of PAA-coated, Si Wafers*

PAA-coated, silicon wafers were prepared by spin-casting. Polyacrylic acid (MW ~50,000, 25 wt% solution in water, Polysciences, Inc. 00627-50) was diluted to 1.25% with DI water and filtered. 2-5 mL of the solution was then deposited on a silicon wafer of approximately two inches in diameter and mounted on a spin-caster (Headway PWM32). Spin-casting was performed for 30 seconds at 2500 rpm to produce a uniform PAA-coating.

*2.3 Preparation of DNA Solutions*

λ-DNA (NEB, N3011S or Takara 3010) was selected due to its low cost and simple genome (a convenience for initial sequencing experiments planned in the near future). Solutions were prepared in tris-ethylenediaminetetraacetic acid (TE) buffer (1X, Sigma 93283-100ML) with SyBr Gold dye (Thermo Fisher Scientific S11494) stock solution diluted 10X, and varying amounts of 1 M NaCl (aqueous dilution of 5M, Sigma 59222C-500ML) as indicated in Table 1.

| Solution | λ-DNA (µl) | SyBr Gold (µl) | 1 M NaCl (µl) | TE (µl) | Heating Prior to Dipping PDMS |
|---|---|---|---|---|---|
| 6.25 µg/ml λ, 100 mM NaCl | 20 | 10 | 160 | 1410 | none |
| 6.25 µg/ml λ, 50 mM NaCl | 20 | 10 | 80 | 1490 | none |
| 6.25 µg/ml λ, 50 mM NaCl | 20 | 10 | 80 | 1490 | 60° C, 30 min |
| 6.25 µg/ml λ, 0 NaCl | 20 | 10 | 0 | 1570 | none |
| 3.12 µg/ml λ, 25 mM NaCl | 20 | 10 | 80 | 3190 | none |
| 3.12 µg/ml λ, 25 mM NaCl | 20 | 10 | 80 | 3190 | 60° C, 30 min |
| 3.12 µg/ml λ, 0 NaCl | 20 | 10 | 0 | 3000 | none |
| 1.56 µg/ml λ, 25 mM NaCl | 20 | 10 | 160 | 6210 | none |
| 1.56 µg/ml λ, 12.5 mM NaCl | 20 | 10 | 80 | 6290 | none |
| 1.56 µg/ml λ, 12.5 mM NaCl | 20 | 10 | 80 | 6290 | 60° C, 30 min |
| 1.56 µg/ml λ, 0 NaCl | 20 | 10 | 0 | 6370 | 60° C, 30 min |
| 2 µg/ml λ, 0 NaCl | 20 | 10 | 0 | 4970 | none |

**Table 1**. DNA solutions.

DNA concentrations were varied with the objective of obtaining optimal adsorbed DNA density and morphology (minimal overlapping, moderate DNA coverage, and absence of branching or curling) for the proposed goal of transposase attachment. The solutions were prepared according to the following procedure: firstly, in all cases, 20 µl λ-DNA, 10 µl SyBr gold stock solution diluted 10X, and 170 µl of TE were pipetted into a PCR tube, vortexed for 30 seconds, and left to incubate for one hour. Then, the appropriate quantities of TE and NaCl solution were added to the tube to achieve the compositions described in the table above, and the

solutions were vortexed for an additional 30 seconds. When necessary, solutions were heated as indicated.

*2.4 DNA Adsorption on PDMS, Stamping onto PAA, and Desorption*

Dipping of PDMS for DNA adsorption and analysis by fluorescence microscopy was performed with one PDMS stamp at a time. 770 µl of the solutions were individually transferred to custom-machined, Teflon wells that served as a solution repository during dipping. A customized apparatus equipped with Teflon tweezers to hold a PDMS stamp, a stepping motor, linear drive stage, and computerized control were used to vertically lower the stamps into the solution wells and then slowly retract them after a 30 second incubation period (See Fig. 4, 5). The samples were then transferred to a clean Petri dish and examined and photographed using fluorescence microscopy (Leica Confocal/Fluorescence Microscope TCS SP2) with 63X magnification and a water lens. Nuclease-free water (Qiagen 129115) was used for viewing with the water lens. In many cases, solution was preserved in the well for several hours and used for multiple PDMS stamp dips, with care taken to cover it between dips in order to prevent entry of dust or other contamination.

Stamping was performed by affixing PAA-coated silicon wafers to a custom-machined, Delrin board with nylon screws to hold them in place. A previously-dipped, PDMS stamp was then placed on the wafer with the leading edge of the dip (the end that went first into the solution during the dipping process) hanging slightly off the edge (about 1 mm) to facilitate its later removal with tweezers. A brass weight of 50 g was placed on top of the sample and manual force was applied for about one minute to transfer DNA from the PDMS to the PAA (See Fig. 6). The PDMS and PAA were then both examined and photographed to assess DNA transfer, again using fluorescence microscopy. 63X magnification and a water lens was used for the PDMS. For the PAA, either the same lens and magnification were used or, alternatively, a 40X oil lens was also used on some occasions. To prevent desorption of the DNA and dissolution of the PAA coating during use of the water lens, a glass slide was positioned between the lens and the sample when examining the PAA, and care was taken to avoid infiltration of water by capillary action between the slide and the sample.

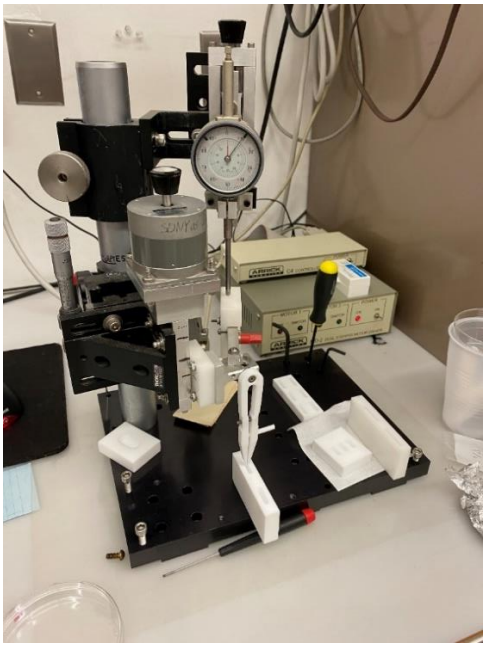

**Figure 4**. Custom apparatus for dipping PDMS stamps in DNA solution. Note Teflon tweezers (to hold PDMS) and well (to hold solution for dipping).

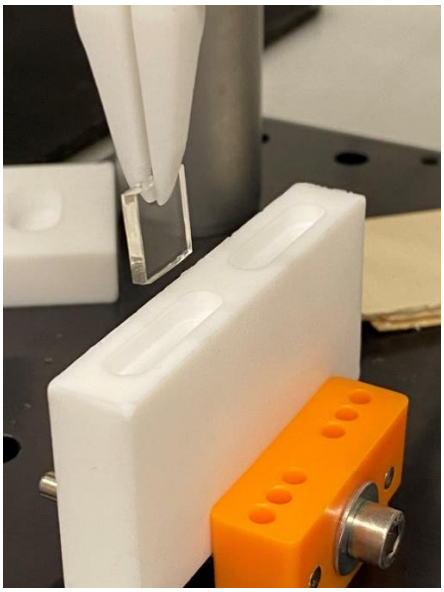

**Figure 5**. Close-up view of tweezers and PDMS stamp immediately prior to dipping in λ solution.

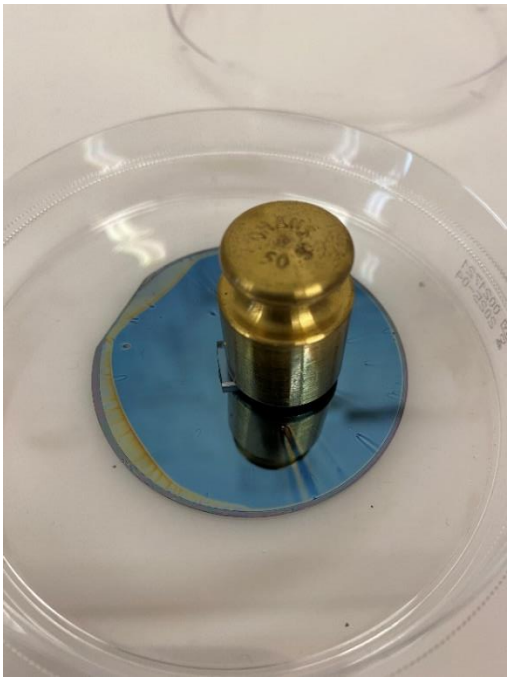

**Figure 6**. PDMS being stamped on a PAA wafer.

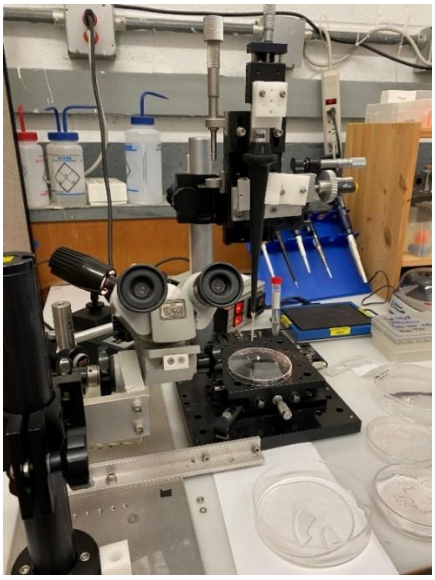

**Figure 7**. Customized apparatus for precise, small volume droplet deposition

Desorption of DNA from PAA was tested with an optimal density sample according to the following procedure. A PAA-coated silicon wafer with DNA stamped on its surface was affixed as described previously to a Delrin board and placed under a custom-designed, mechanical apparatus (Fig. 7) designed to hold a pipette and deposit extremely small volume drops of liquid (≈1 μl) with high precision. The pipette was loaded with 1 M NaCl solution and several carefully positioned droplets were placed on the PAA surface in regions where the presence of DNA was previously confirmed by microscopy. The sample was then reexamined at 63X magnification with a water lens (again employing a slide to avoid wetting of the PAA/uncontrolled DNA desorption) to check for evidence of DNA desorption.

## 3. Results and Discussion

A general trend of increasing adsorbed DNA density on PDMS stamps was observed with increasing concentrations of λ in the solutions that

stamps were dipped into. Moderate densities of cleanly stretched DNA were frequently observed at 3.12 μg/ml λ, 2 μg/ml λ, and 1.56 μg/ml λ concentrations (Fig. 8), though in some cases, the 1.56 μg/ml λ in particular yielded extremely low densities (scattered strands of DNA that were difficult to detect by fluorescence microscopy by virtue of their scarcity on the stamp, Fig. 9). Higher densities of adsorbed λ were usually observed with 6.25 μg/ml λ or 3.12 μg/ml λ solutions, with the highest found using 6.25 μg/ml λ and 100 mM NaCl. Branching of adsorbed DNA – rather than clean, linear stretching – was usually observed with 6.25 μg/ml λ solutions and frequently observed with 3.12 μg/ml λ solutions (Figs. 10, 13). It was also less frequently observed at concentrations of 1.56 μg/ml λ when NaCl was added. The branching effect was usually more pronounced at higher NaCl concentrations. In some cases, particularly with higher DNA concentration solutions, adsorbed DNA was found to be curled into a chromatin-like state and neither stretched nor branched (Fig. 11). Most PDMS stamps (regardless of which solution they were dipped into) exhibited notable variation in the density and character of the adsorbed DNA (Fig. 12). With higher DNA concentration solutions, successive dipping of different PDMS stamps into the same well often produced a noticeable decline in the amount of DNA that was adsorbed. The effect of heating solutions on DNA adsorption on PDMS was inconclusive, with similar variations in adsorbed DNA morphology and density detected when both unheated and heated solutions were used, and no suggestive trends.

Stamping onto PAA resulted in an apparent failure to transfer DNA from PDMS approximately 50% of the time in numerous trials. However, successful transfer by stamping was confirmed on several occasions, both by observation of DNA on PAA (Figs. 13, 14, 17) and reexamination of PDMS subsequent to its being used for stamping, where a delineation between areas that still exhibited adsorbed DNA and others which did not was sometimes detected (Fig. 15). The transfer efficiency, assessed qualitatively, varied. In some cases, an efficiency evidently approaching 100% was detected, with a sharp delineation between the area of the PDMS that did not contact the PAA (and therefore retained DNA) and that which did (and, concordantly, did not exhibit any adsorbed DNA) (Fig. 16). In other stamping trials, in areas of PDMS that contacted PAA, an irregular DNA distribution on PDMS was observed post-stamping, with an apparent diminution in the overall density and a disruption in the observed character of the DNA (relative both to images of the exact sample prior to stamping, and DNA still visible on areas of the PDMS that were not placed over the PAA, since, as described previously, the stamp was left hanging off the PAA to facilitate its removal) (Fig. 17).

Several examples of PAA that exhibited the moderate DNA densities considered ideal for the overarching, future goal of transposase attachment and activation for NGS library preparation were selected for desorption tests. Deposition of a droplet of NaCl solution was found to be successful at removing DNA, with the areas within the droplet exhibiting a distinct absence of DNA relative to the areas adjacent to the droplet (where adsorbed DNA was still visible) (Fig. 18).

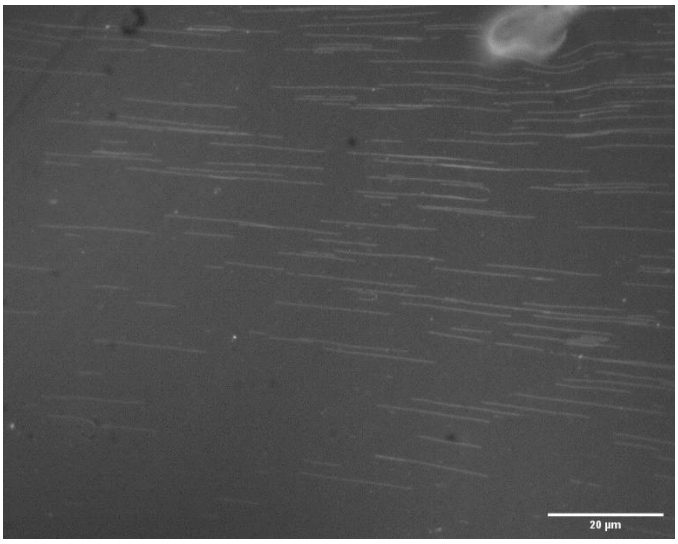


**Figure 8**. λ-DNA on PDMS subsequent to dipping in 2 µg/ml λ-DNA with 0 NaCl. Note moderate density and clean stretching of DNA. This is considered optimal and was only observed with some 3.12 µg/ml λ-DNA 25 mM or 0 NaCl, 2 µg/ml λ-DNA 0 NaCl, and 1.56 µg/ml λ-DNA 12.5 mM NaCl solutions.

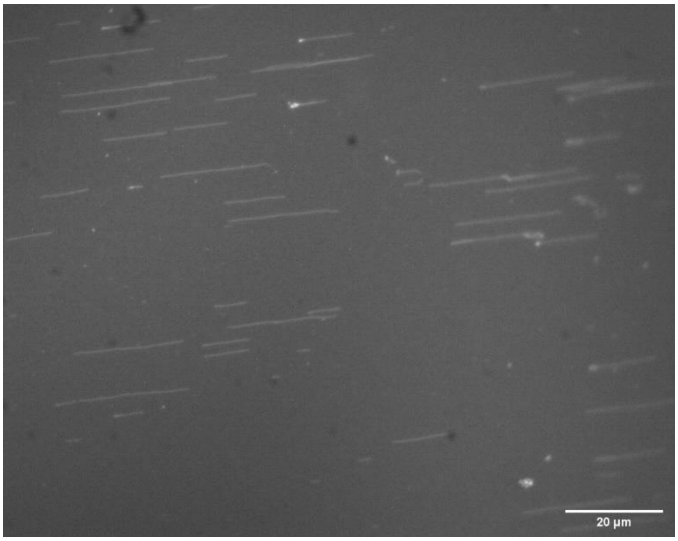


**Figure 9**. λ-DNA on PDMS. 2 µg/ml λ, 0 NaCl dip solution. Very sparce DNA adsorption. Unsuitable for transposase attachment by an ordered means.

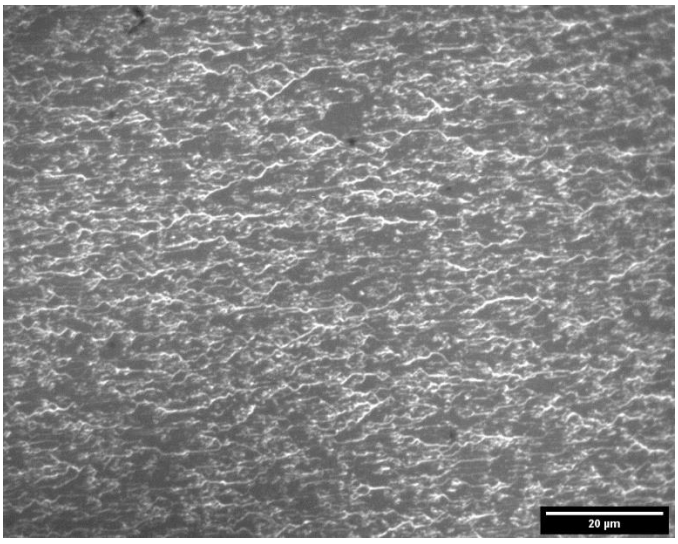


**Figure 10**. λ-DNA on PDMS. 6.25 µg/ml λ, 50 mM NaCl dip solution. Marked example of branching (unsuitable for stamping and transposase attachment by an ordered means).

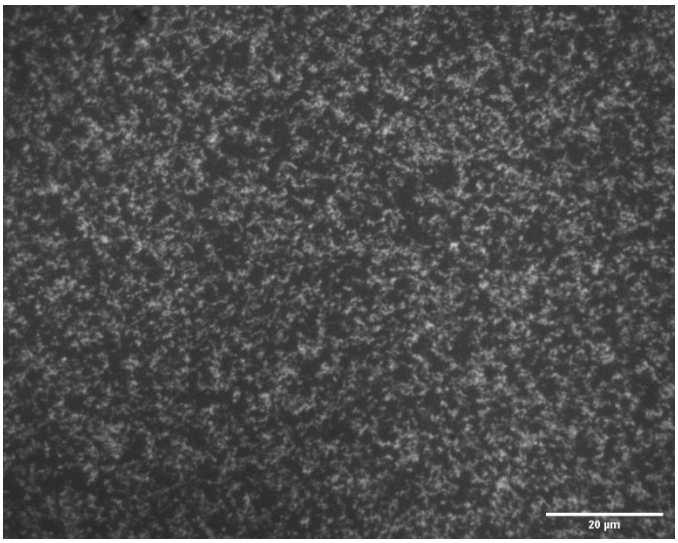


**Figure 11**. λ-DNA on PDMS. 6.25 µg/ml λ, 50 mM NaCl dip solution. Marked example of curling into chromatin-like state (similarly unsuitable for stamping and transposase attachment by an ordered means).

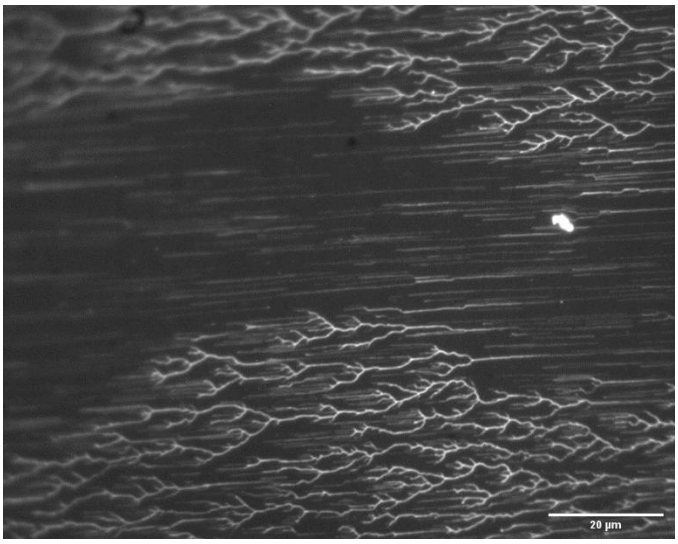


**Figure 12**. λ-DNA on PDMS. 6.25 µg/ml λ, 50 mM NaCl dip solution. Note inconsistency. Excessive density and branching in some areas, clean stretching in others. These characteristics warrant more investigation and may be attributable, at least in part, to PDMS surface effects.

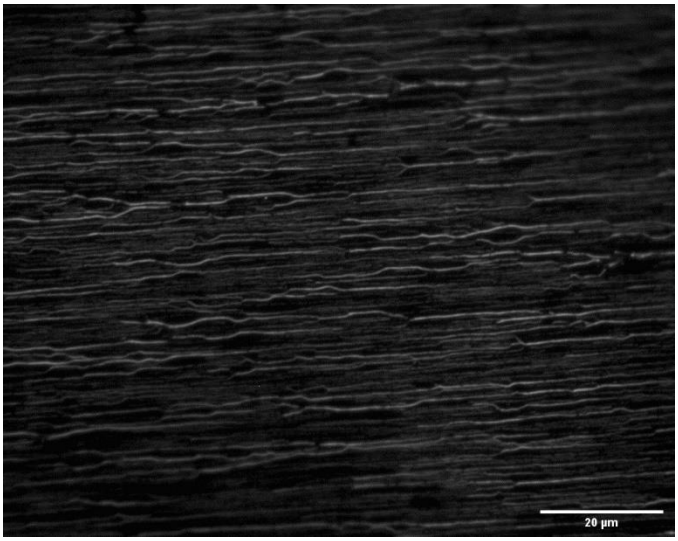


**Figure 13**. λ-DNA on PDMS. 6.25 µg/ml λ, 50 mM NaCl dip solution. High density and branching, visible here, were commonly observed when using this solution and also with 3.12 µg/ml λ solutions.

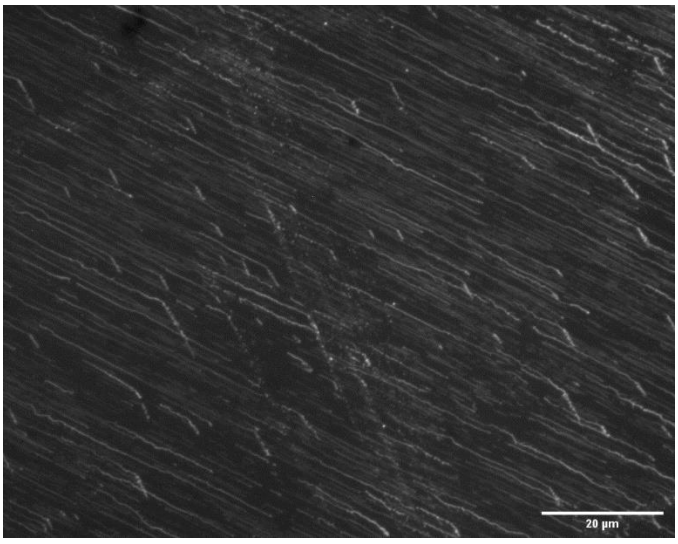


**Figure 14**. λ-DNA on PAA subsequent to stamping. This DNA was stamped to PAA using the exact PDMS stamp appearing in Fig. 13. This is an example of efficient transfer, with a density that resembles that on the PDMS and similarities in the pattern. (This was an early test of stamping that was carried out at higher density despite the undesirability of excessive density.)

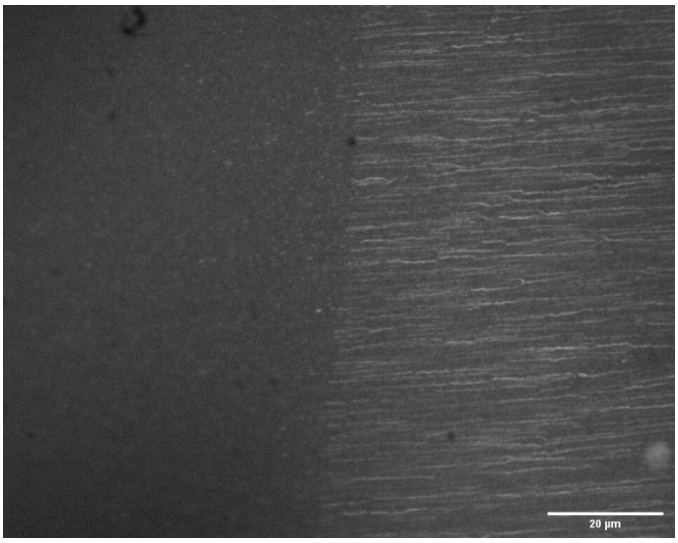


**Figure 15**. λ-DNA on PDMS subsequent to PAA stamping, reexamined at border of stamped region. Note the sharp delineation at the border between the stamped and unstamped areas, suggestive of high efficiency in this example.

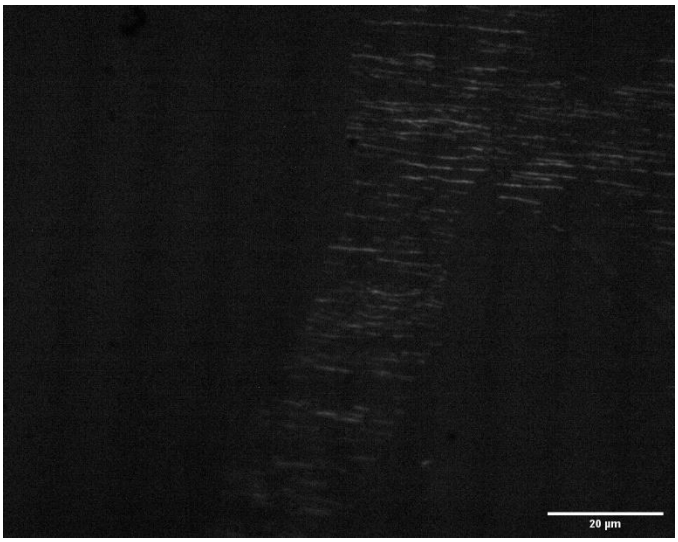


**Figure 16**. λ-DNA on PDMS subsequent to PAA stamping, reexamined near the border of stamped region. Note the presence of a swath of adsorbed DNA beyond the border of the stamped area, indicative of poor transfer efficiency.

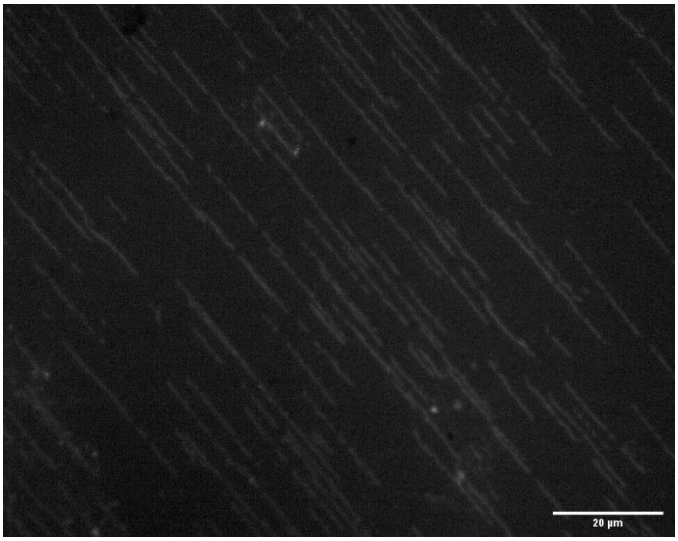


**Figure 17**. λ-DNA on PAA subsequent to stamping. Original PDMS stamp dipping solution was 3.12 µg/ml λ, 25mM-NaCl.

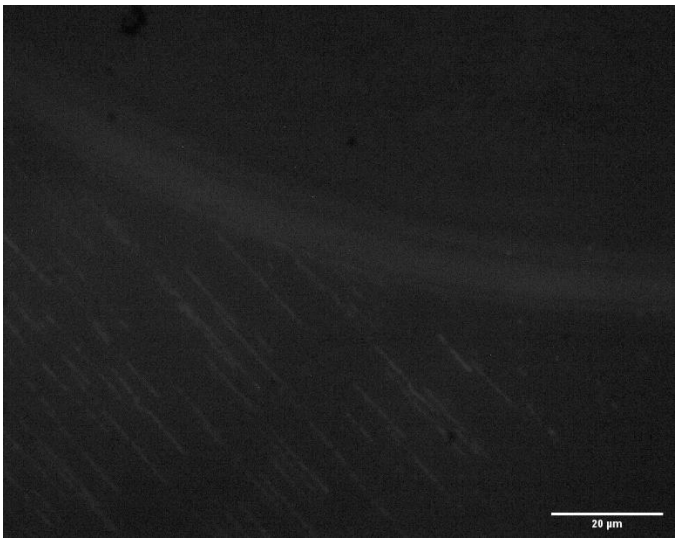


**Figure 18**. Desorption of DNA from the PAA sample appearing in Fig. 17. Note removal of DNA within NaCl solution droplet.

The general trend of increase in the adsorbed DNA density with increasing dip solution DNA concentration was predictable and intuitive. Fine tuning of the solutions so that an optimal, moderate density for the future goal of transposase attachment and activation is consistently reproducible in a future NGS library preparation method is required. If DNA is too sparsely adsorbed on PDMS, there may be an insufficient quantity to work with for NGS. Conversely, if the adsorbed DNA is too dense, the process will be inefficient and wasteful. Additionally, if branching is present, attachment of transposases will be rendered more difficult (less controllable and inefficient). Results here suggest that an optimal density is most consistently attained with a 2 µg/ml λ solution and 0 NaCl or 1.56 µg/ml λ solution with 12.5 mM NaCl.

The apparent reduction in the amount of adsorbed DNA observed at higher densities when successive stamp dips were performed into the well suggests that depletion of DNA in the well is a potential issue. A quantitative, rather than purely qualitative assessment of the DNA adsorption is warranted to assess and confirm this. Using identical

PDMS stamps with a known surface area as a control, and measuring adsorbed DNA surface densities during successive dip trials, followed by comparison of the quantity of the DNA removed thereby to the known original DNA content in the dip solution would be a straightforward approach.

That solutions with zero NaCl concentration regularly produced high densities of DNA adsorption on PDMS conflicts with results of Benke et. al., who reported low DNA adsorption on PDMS at zero NaCl concentration [10]. Benke et. al. also reported a substantial impact of pH on DNA adsorption on PDMS, with the highest density at a pH of 4, a trend of higher density but reductions in stretching as pH values were decreased, and a trend of reduction in density at higher pH values [10]. Some experimental results reported here, such as curling of DNA and low densities, were also detected by Benke et. al. when adsorbing DNA on PDMS with low pH solutions [10], which suggests that solution pH may have been a factor. Additional, systematic experimentation incorporating pH as a variable in our method is warranted. Branching and coiling were likely attributable to overly strong adhesion of DNA to the PDMS [10].

Experimentation here did not include any attempt to assess the extent to which the frequently encountered variation in the quality of DNA adsorbed on PDMS was attributable to surface effects. It is possible that irregularities in the PDMS surface (such as deformation resulting from shearing forces exerted when cutting the PDMS into stamps with a razor blade, roughness created during the curing process due to trapped air bubbles, or roughness on the surface of the Petri dish in which the PDMS was cured) could have been responsible for changing both the morphology and density of adsorbed DNA. More investigation and thorough characterization of PDMS stamp surfaces prior to dipping is warranted.

The absence of any discernable trend or impact stemming from heating of the solutions warrants further investigation. Heating was employed with the belief that it might reduce branching and DNA concatenation due to the presence of sticky ends, as well as promote binding of the dye to the DNA, thereby improving image brightness. (Dimness during fluorescence microscopy was a frequent issue.)

Variations in the efficiency of DNA transferal from PDMS to PAA were likely attributable to several distinct factors. Firstly, as mentioned in the procedure, the stamping was performed by applying force by hand; by its nature, this is obviously not precisely controllable or quantifiable. Application of a greater and more uniform force than that supplied by a human hand might induce more complete contact between the PDMS and PAA during stamping and, thereby, improve transfer efficiency (provided that the force is not so great that it crushes the silicon wafer). Residual amounts of aqueous solution on the PDMS may have also been responsible for transfer efficiency variations (despite attempts to dry the PDMS stamps after viewing under the microscope water lens, trace amounts sufficient to wet and partially dissolve the surface of the PAA to the detriment of the transferal process may have been present). Additionally, shearing forces experienced by the DNA during removal of the PDMS from PAA after stamping may have disturbed the DNA. (PDMS stamp removal from PAA after stamping was performed as carefully as possible using Teflon tweezers, with an attempt to limit any lateral sliding of the stamp along the surface of the PAA that would produce shear force; nevertheless, this procedure suffers from the limitations of human fine motor control.)

For incorporation into a future NGS clonal template library preparation method, it is envisaged that this procedure could be expanded by performing DNA adsorption on a PDMS stamp created by soft-lithography. As mentioned previously, a PDMS stamp containing grooves created by soft-

lithography was used by Sokolov, et. al., to deliver the DNA-cleaving enzyme DNase1 to DNA immobilized on a PMMA-coated silicon wafer. An alternative use for such a patterned PDMS stamp might be to carry out DNA adsorption according to the method reported here, and take advantage of DNA segments spanning grooves in the PDMS to deliver a solution containing transposases by microfluidics. Subsequently, the DNA could possibly be stamped onto PAA where a magnesium ion solution could be used for transposase activation. Additional work is required to ultimately develop an effective procedure along these lines.

DNA desorption from PAA was performed using an NaCl solution which apparently dissolved the PAA while removing the DNA. While sufficient to demonstrate a basic proof of concept that DNA can be removed from PAA, this is unlikely to be an ideal approach for the end application. PAA was selected as substrate for stamping, in part, due to its reversible solubility [11]. In the presence of small concentrations of divalent cations such as $Ca^{2+}$, easily obtainable by using, for example, a solution of $CaCl_2$, PAA becomes water insoluble due to cross-linkage of the polymer [11], a characteristic that may be of use for transposase delivery and activation, as well as desorption. It will likely be necessary to perform some or all of those actions on DNA adsorbed on PAA, where dissolution of the PAA would present a serious complication.

## 4. Conclusion

Adsorption of DNA onto PDMS and subsequent transferal via stamping to a PAA-coated, silicon wafer were demonstrated, with adsorbed DNA density on PDMS depending, in part, on solution DNA and NaCl concentrations, and variability in both the reproducibility and efficiency of DNA transferal from PDMS to PAA observed during multiple trials. Such methods of handling DNA could be incorporated into a future method of DNA clonal template library preparation for NGS, provided that suitable methods of transposase attachment and activation (possibly involving surfaces with a grating structure and microfluidics) or another means of rendering the original, genomic positional order of fragments identifiable can be devised. More work to investigate and explain the nature of both surface effects on DNA adsorption on PDMS and PAA and properties such as temperature and pH are warranted.

## 5. Acknowledgements

Special thanks are owed to Professor Jonathan Sokolov, PhD, of the State University of New York at Stony Brook for his guidance and encouragement.

## 6. References

[1] Budassi, J., Cho, N., Del Valle, A., Sokolov, J. Microfluidic delivery of cutting enzymes for fragmentation of surface-adsorbed DNA molecules. Bulletin of the American Physical Society 2019 64(2).

[2] Hood, L., Rowen, L. The Human Genome Project: Big Science Transforms Biology and Medicine. Genome Medicine 2013 5(9).

[3] Ballouz, S., Dobin, A., Gillis, J.A. Is it time to change the reference genome? Genome Biology 2019 20, Article 159.

[4] Hannan, A. J. Tandem repeats mediating genetic plasticity in health and disease. Nature Review Genetics 2018 19(5), 286-298.

[5] Goodwin, S., McPherson, J.D., McCombie, W.R. Coming of Age: Ten Years of Next-Generation Sequencing Technologies. Nature Reviews, Genetics. 2016 17.

[6] Cho, N., Goodwin, S., Budassi, J., Zhu, K., McCombie, W.R., Sokolov, J. Fragmentation of Surface Adsorbed and Aligned DNA Molecules using Soft Lithography for Next-Generation Sequencing. Journal of Biosensors & Bioelectronics 2017 8(3).

[7] Pfeiffer, F., Gröber, C., Blank, M. et al. Systematic evaluation of error rates and causes in short samples in next-generation sequencing. Sci Rep 2018 8, 10950.
[8] Ma, X., Shao, Y., Tian, L. et al. Analysis of error profiles in deep next-generation sequencing data. Genome Biol 2019 20, Article 50.
[9] Mantere, T., Kersten, S., Hoischen, A. Long-Read Sequencing Emerging in Medical Genetics. Frontiers in Genetics 2019 10, Article 426.
[10] Benke, A., Mertig, M., Pompe, W. PH- and Salt-dependent Molecular Combing of DNA: Experiments and Phenomenological Model. Nanotechnology 2011 22(3).
[11] Linder, V., Gates, B.D., Ryan, D., Parviz, B.A., Whitesides, G.M. Water-Soluble Sacrificial Layers for Surface Micromachining. Small 2005 1(5).

# Optimization of Operating Parameters on Proton Exchange Membrane Fuel Cells for Efficiency

Jacky Jiang [a], Sarjeel Zaman [a], Abdulhazeez Adeniji [a], Hillary Wong [a]

[a] *Department of Materials Science and Chemical Engineering and Institute of Gas Innovation and Technology, Stony Brook University, Stony Brook, NY 11794, USA*

**Abstract**

As researchers begin to focus on overcoming the effects of climate change, there is a growing interest in the search for alternative and sustainable clean energy sources. The use of proton exchange membrane fuel cells (PEMFC) is a developing technology that produces clean energy from hydrogen and oxygen, with fresh water and heat as the only byproduct and has a wide range of practical applications. The successful operation of a PEMFC with high efficiency and power output is dependent on all sub-systems of the fuel cell such as the flow field design, catalysts, membrane, and operating parameters. This study focuses specifically on the operating parameters: cell temperature, relative humidity (RH), and back pressure. While several studies have been conducted on the effects of individual operating parameters on the performance of PEMFC, our study takes a comprehensive approach to optimize the operating parameters, evaluating the influence of each parameter individually and collectively, simultaneously. The fuel cell performance was characterized using polarization curves, along with comprehensive power density curves for each specified operating conditions. Based on the results, higher operating temperatures at higher relative humidity levels led to greater fuel cell performance, whereas higher operating temperature at lower relative humidity levels resulted in adverse effects on performance. Increased relative humidity was found to have a positive effect on performance at higher operating temperatures due to reduced risks of flooding at higher temperatures. Higher back pressure was found to beneficial for fuel cell performance. The power density measurements suggest that the most significant parameter is operating temperature.

*Keywords*: Proton Exchange Membrane Fuel Cell, Operating Conditions, Optimization, Performance, Power Output, Polarization Curve, Temperature, Pressure, Relative Humidity,

## 1. Introduction

The use of fossil fuels in energy generation has led to a concerning increase in carbon dioxide ($CO_2$) emissions that is accelerating global climate change. The reduction of $CO_2$ and other greenhouse gases, combined with the shift to clean forms of energy, has become paramount in the energy sector. As the most abundant element on Earth, hydrogen may act as a solution for the growing demand for clean energy. Fuel cell technologies are based on the utilization of hydrogen gas as an energy storage. Proton exchange membrane fuel cells, also known as PEMFCs, offer great advantages such as the ability to produce large amounts of energy with its small and compact volume, high conversion efficiency, and low operating temperatures [1]. This low temperature

operation, along with fast startup time and ideal power-to-weight ratio, makes PEMFCs ideal for use in practical transportation applications [2].

During fuel cell operation, hydrogen fuel is transported to the anodic side, while oxygen from air is fed to the cathodic side. The hydrogen oxidation reaction (HOR) and oxygen reduction reaction (ORR) that occur at their respective electrodes are typically slow reactions that require a catalyst, typically platinum, to accelerate the reaction kinetics [3]. The polymer electrolyte membrane is semi-permeable with only proton passage allowed, preventing gas crossover. An electrical current is generated as the electrons travel along an external circuit to the cathode. The half reactions that occur at each electrode are shown in Equations 1 and 2. Figure 1 illustrates the schematic diagram of a PEM fuel cell operation.

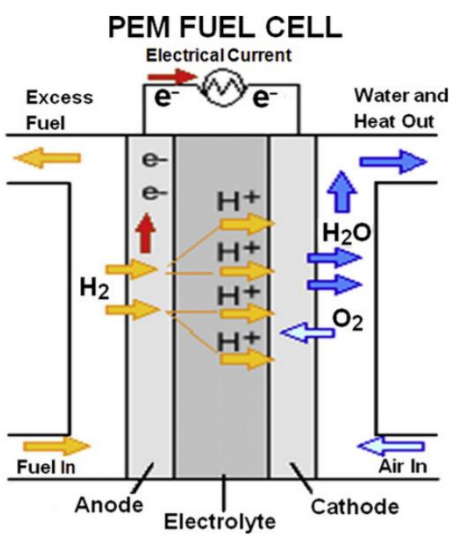


**Figure 1.** Schematic of PEM fuel cell [1].

$$\text{Anode: } 2H_2 \rightarrow 4H^+ + 4e^- \quad (1)$$

$$\text{Cathode: } O_2 + 4H^+ + 4e^- \rightarrow 2H_2O \quad (2)$$

$$\text{Overall: } 2H_2 + O_2 \rightarrow 2H_2O \quad (3)$$

The success of a PEMFC for high efficiency and power output is dependent on several components, such as the flow field design, choice of catalyst and membrane, and operating conditions. Many fundamental studies have explored the individual effects of operating parameters, namely operating temperature, pressure, and relative humidity). In a study conducted by Ozen et al. [4], it was established that an increase in the relative humidity and temperature of inlet gases, and operating temperature of a fuel cell enhances the fuel cell performance. The study shows that the polymer membrane should have adequate moisture for high-efficiency performance as proton transport is accompanied by water, but an excess amount of water could also result in membrane flooding, which could limit the activity of the catalyst, thus lowering the performance of the PEMFC. Operating temperature influences the performance of a PEMFC as both mass transport and the conductivity of the membrane are enhanced at elevated operating temperature. However, at significantly higher operating temperatures, the performance of the fuel cell was found to be lower, which attributed to inadequate hydration. This explains the importance of water management and the selection of operating temperature of the PEMFC. In another study by Wang et al. [5], the results showed enhanced fuel cell performance with increasing back pressure. This increase was caused by the rise in the exchange current and density and reactant gas partial pressure.

In this study, a holistic approach is adopted to the optimization of the operating parameters, evaluating the influence of each parameter individually and collectively. This work aims to determine which operating parameter has the most significant effect on enhancing the performance of the PEMFC. The performance of the PEMFC was evaluated by individually varying each of the three operating conditions (temperature, pressure, and relative humidity) while keeping the other two operating conditions fixed. Multiple trials for each varying operating condition were performed at different levels of fixed operating parameters, defined as low, medium, and high. A detailed

description of all the variations of operating conditions is shown in Table 1. This study chose to work with a range of operating conditions typically found in practical real-life applications, such as front loaders. The novelty of this study is emphasized through the comprehensive and holistic approach, evaluating, and understanding the performance of the fuel cell throughout the entire range of each operating conditions from low to high.

The experimental results are presented in polarization and power density curves. Polarization curves are useful for tracking the performance and behavior of a fuel cell under specific testing conditions. The polarization curves and peak power density measurements were used as a metric for defining performance and to determine the most influential operating parameter on fuel cell performance.

## 2. Experimental Methods

### *2.1. Equipment and Specifications*

In this study, the Scribner Model 850e Fuel Cell Test System was used to collect the polarization curves. A single cell fuel cell fixture, consisting of a Nafion™-212 membrane, gold-plated current collectors, anodized aluminum end plates and an active cell area of 5 $cm^2$ with a platinum loading of 0.3 $mg/cm^2$ for the anode and cathode, was used. The Scribner 850BP unit was used to manually control the back pressure of the anodic and cathodic sides.

### *2.2 Operating Conditions*

**Table 1.** Variation of Operating Conditions.

| Varying Operating Condition | Low Fixed Operating Conditions | Medium Fixed Operating Conditions | High Fixed Operating Conditions |
|---|---|---|---|
| **Cell temperature: 50°C, 62°C, 74°C** | 5 psi, 25% RH | 15 psi, 55% RH | 25 psi, 75% RH |
| **Back pressure: 5 psi, 15 psi, 25 psi** | 50°C, 25% RH | 62°C, 55% RH | 74°C, 75% RH |
| **Relative humidity (RH): 25%, 55%, 75%** | 50°C, 5 psi | 62°C, 15 psi | 74°C, 25 psi |

### *2.3 Methodology*

To obtain the polarization curves, the Scribner 885 Potentiostat was used to acquire voltage and current measurements by linear sweep voltammetry. Voltage was swept from open circuit voltage (OCV) to 0.1 V in intervals of 0.05 V. The voltage was measured over a full current density range at different operating conditions to construct the polarization curve. The reactant humidification temperature was changed in accordance with the cell temperature to achieve the desired relative humidity. A stoichiometric ratio of 3:2 was used for air and hydrogen, respectively. Periodical purging of water from the system was done after every run.

## 3. Results and Discussion

### *3.1. The Effects of Operating Temperature on Performance*

To understand the effects of operating temperature on a PEM fuel cell performance, the polarization curves, shown in Figures 2, 3, and 4, were analyzed. The temperature effects on performance were studied at different fixed relative humidity levels and different fixed back pressures. The polarization curves showed that an increase in temperature had a positive effect on fuel cell performance with an exception to this trend, shown

in Figure 2. The exception occurred at the low fixed operating parameters (5 psi, 25% RH), where a decrease in performance was observed as temperature increased from 62 and 74°C. This phenomenon likely occurred due to operation at low RH. The water content at 25% RH did not provide sufficient membrane hydration at this high operating temperature, hence reducing the membrane conductivity and suffering greater ohmic losses due to an increase in ionic resistance to charge flow. Therefore, it is crucial that an increase in cell temperature is followed with an increase in humidification temperature to ensure proper hydration for optimal performance at elevated temperatures.

In Figures 3 and 4, there was a slight performance increase at the medium current density regions, indicating small improvements in ohmic loss with increasing temperature. Esfeh et al. [8] studied the effects on temperature on concentration over-potential and concluded that an increase in temperature led to a decrease in concentration over-potential. This finding correlates with the experimental data, explaining the improvement in mass transport losses. For medium and high fixed operating parameters, the fuel cell performance increased consistently with increasing temperature. This is due to an increase in proton mobility and improved electrode kinetics for the oxygen reduction (ORR) and the hydrogen oxidation (HOR) [4]. The fixed medium and high relative humidity levels ensured that the membrane would not become dehydrated when the temperature was increased to 74°C, unlike the case at low relative humidity. However, increasing operating temperature is limited by the membrane material limits as well. The membrane will eventually begin to degrade at a certain elevated temperature which will have an adverse effect on performance. By comparing the effects of operating temperature at low, medium, and high fixed operating parameters, it was observed that the best performance was achieved at a temperature of 74°C with fixed operating parameters of 25 psi and 75% RH. The highest power density output of 0.66 mW/cm$^2$ was observed at 74°C, 25 psi, and 75% RH.

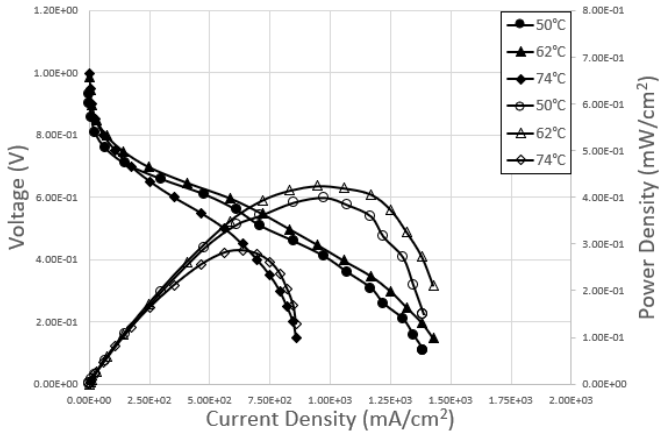


**Figure 2.** Polarization and power density curves for different cell temperatures at low fixed operating parameters of 5 psi and 25% RH.

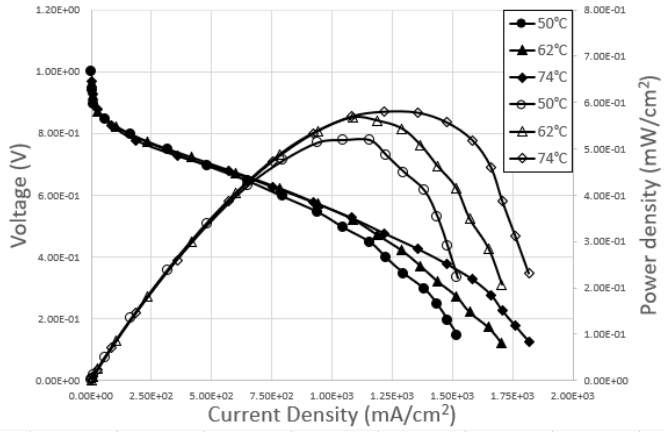


**Figure 3.** Polarization and power density curves for different cell temperatures at medium fixed operating parameters of 15 psi and 55% RH.

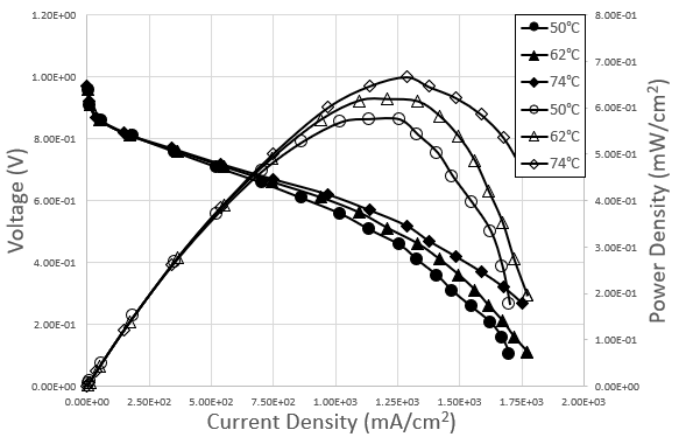


**Figure 4.** Polarization and power density curves for different cell temperatures at high fixed operating parameters of 25 psi and 75% RH.

*3.2. The Effects of Back Pressure on Performance*

To investigate the back pressure effects on fuel cell performance, polarization curves were scanned at different back pressures as shown in Figures 5, 6, and 7. To reiterate, this optimization approach studies the effects of back pressure at different levels of fixed relative humidity and operating temperature. Based on the polarization curves, it is evident that increasing back pressure had a positive effect on fuel cell performance in all levels of fixed operating parameters (low, medium, high). The performance increase with increasing back pressure was consistent throughout the entire voltage sweep, showing increased performance in all current density regions. According to a study done by Zhang et al. [9], it was established that higher back pressure resulted in faster electrode kinetics due to lower charge transfer resistance, overcoming activation losses. This is attributed to higher partial pressures of the reactant gases with increasing back pressure. The study also performed AC impedance spectroscopy at different back pressures, it was found that mass transfer resistance decreased as back pressure increased, indicating that higher back pressures led to reduced mass transport losses. Increased operating pressure is, however, limited by gas crossover through the membrane, which can decrease the performance of the fuel and raise safety concerns in terms of hydrogen-oxygen mixture.

The highest power density was apparent at high back pressure operation of 25 psi. Comparing the pressure effect experiments at different fixed relative humidity and temperature, the highest power density measurement was found to be 0.647 mW/cm$^2$ at 25 psi, 74°C, and 75% RH. This finding indicated that a high back pressure (25 psi), along with high relative humidity and high operating temperature, exhibited the greatest power output and performance.

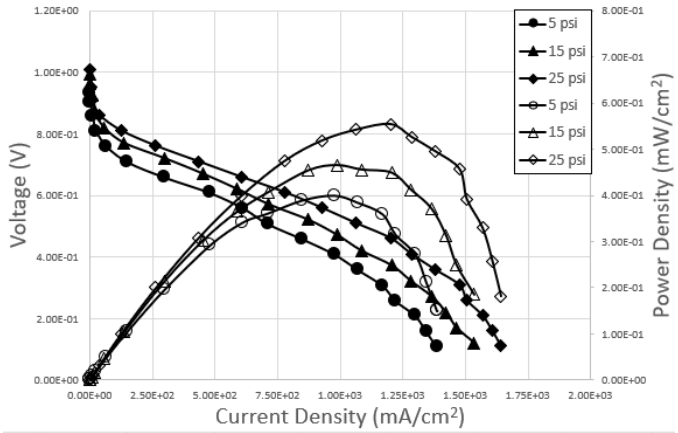


**Figure 5.** Polarization and power density curves for different back pressures at low fixed parameters of 50°C and 25% RH.

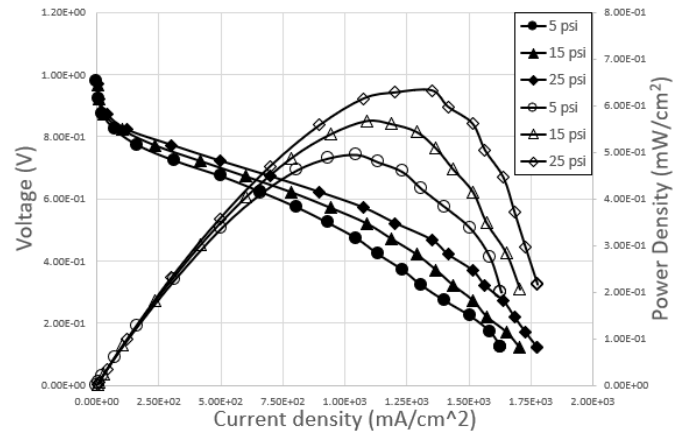


**Figure 6.** Polarization and power density curves for different back pressures at medium fixed parameters of 62°C and 55% RH.

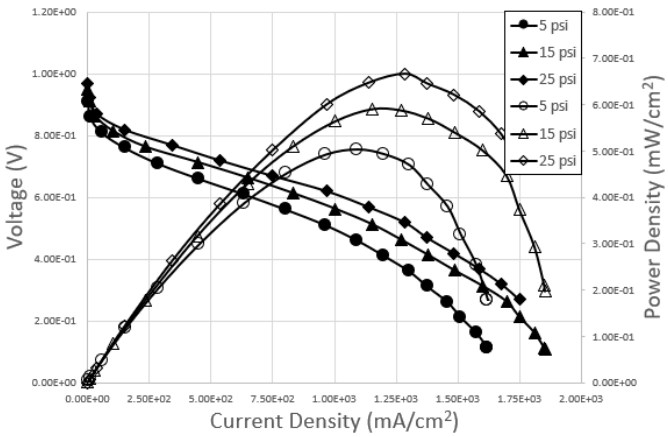


**Figure 7.** Polarization and power density curves for different back pressures at high fixed parameters of 74°C and 75% RH.

### *3.3. The Effects of Relative Humidity on Performance*

The influence of relative humidity on fuel cell performance at different operating temperatures and back pressures was explored using the polarization curves shown in Figures 8, 9, and 10. At low and medium fixed operating temperature and pressure, fuel cell performance increased significantly with increasing RH until high current density regions. At medium current density, the increase in RH led to better hydration in the membrane which improved membrane conductivity, allowing better proton transport through the membrane. In addition, the active surface area of the catalyst layer in the membrane electrode assembly (MEA) increased as a result of the increased hydration levels [5]. Consequently, reaction kinetics are enhanced, leading to improved performance. At high current density, reaction kinetics increases, causing higher water production. The combination of higher water production and higher relative humidity levels led to excess water retention in the membrane, effectively decreasing the porosity of the membrane due to flooding. More importantly, hydration has been known to increase the active surface area of the catalyst layer, but excessive hydration can inadvertently flood the active sites of the catalyst layer. As a result, there were adverse effects on performance with increasing RH at high current densities at low and medium fixed temperature and pressure.

In comparison to the relative humidity effects on performance at high fixed temperature, the flooding effects of water in the membrane was mitigated which is shown with the overall increase in performance with increasing RH in Figure 10. This phenomenon is likely a result of the high operating temperature and greater water evaporation, which prevented flooding in the membrane. Hence, there is decreased mass transport losses and enhanced performance with increasing RH. Based on these results, increasing relative humidity is limited by water management issues in the fuel cell, such that flooding of water in the cell becomes an issue at some point. The most optimal operating conditions in these set of experiments was found to be 75% RH, 25 psi, 74°C with the highest power density of 0.66 mW/cm$^2$.

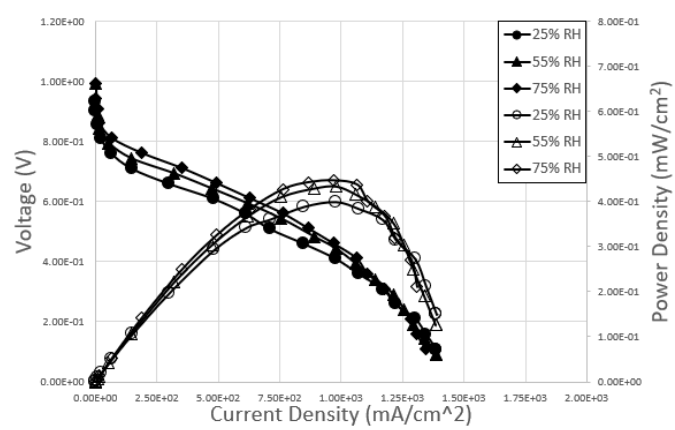


**Figure 8.** Polarization and power density curves for different RH at low fixed parameters of 50°C and 5 psi.

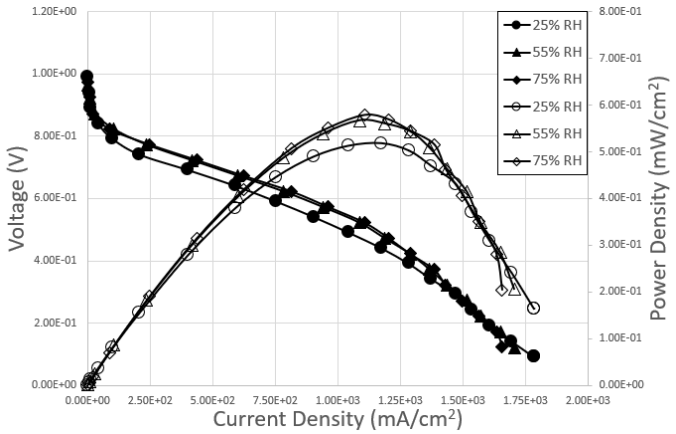


**Figure 9.** Polarization and power density curves for different RH at medium fixed parameters of 62°C and 15 psi.

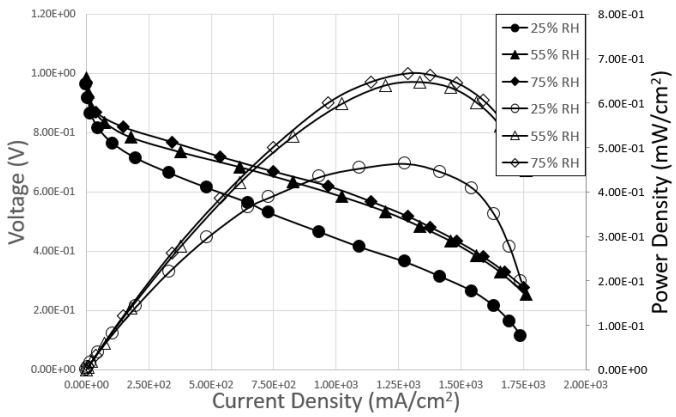


**Figure 10.** Polarization and power density curves for different RH at high fixed parameters of 74°C and 25 psi.

*3.4 Summary of Data*

To summarize the effects of each operating condition on fuel cell performance, the maximum power density was plotted as a function of each operating condition, shown in Figures 11, 12, and 13. To determine the most influential operating parameter, a ratio was developed between the percentage change in maximum power density divided by the percentage change of the varying operating parameter. This ratio is an unitless indicator of the operating parameter's degree of influence on fuel cell performance.

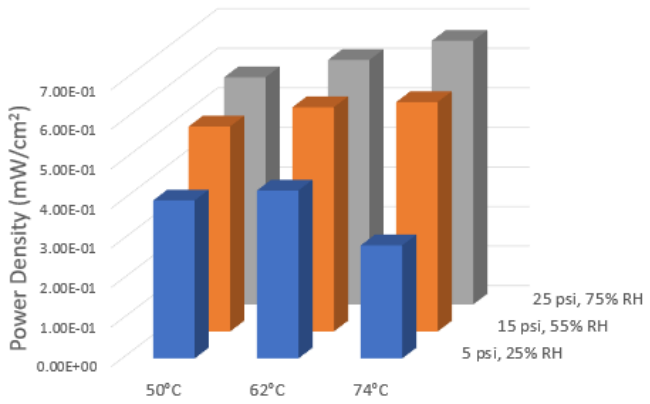


**Figure 11.** Maximum power density as a function of operating temperature.

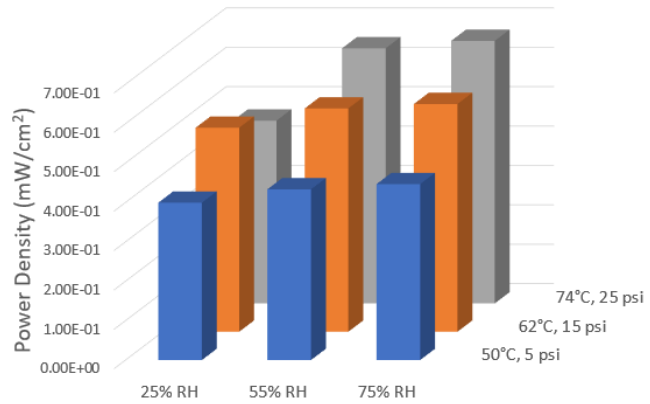


**Figure 12.** Maximum power density as a function of relative humidity.

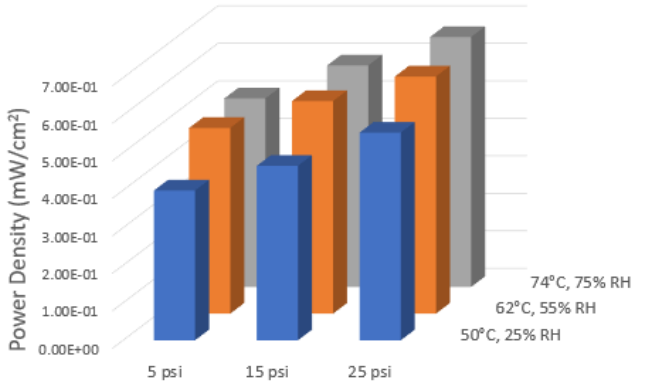


**Figure 13.** Maximum power density as a function of back pressure.

The degree of influence for each operating parameter (temperature, back pressure, relative humidity) on fuel cell performance is shown in Tables 2, 3, and 4. A positive degree of influence indicates an increase in performance with an increase in the operating condition, whereas a decrease in performance is denoted by a negative degree of influence. Operating temperature was found to have the highest degree of influence, indicating that operating temperature is most influential parameter on fuel cell performance.

**Table 2.** Degree of influence of operating temperature on fuel cell performance for each level of fixed operating conditions.

| Degree of Influence (unitless) of Temperature | |
|---|---|
| 5 psi, 25% RH | -0.590 |
| 15 psi, 55% RH | 0.249 |
| 25 psi, 25% RH | 0.333 |

**Table 3.** Degree of influence of back pressure on fuel cell performance for each level of fixed operating conditions.

| Degree of Influence (unitless) of Back Pressure | |
|---|---|
| 50°C, 25% RH | 0.058 |
| 62°C, 55% RH | 0.058 |
| 74°C, 75% RH | 0.218 |

**Table 4.** Degree of influence of relative humidity on fuel cell performance for each level of fixed operating conditions.

| Degree of Influence (unitless) of Back Pressure | |
|---|---|
| 50°C, 5 psi | 0.097 |
| 62°C, 15 psi | 0.069 |
| 74°C, 25 psi | 0.081 |

## 4. Conclusion

In this study, the performance of a PEM fuel cell has been evaluated and optimized for varied operating conditions using the Scriber Model 850e fuel cell test system. Experimentation with various combinations of operating conditions have been conducted to observe and analyze the effects of operating temperature, relative humidity, and back pressure at low, medium, and high fixed operating parameters. The results garnered from the experimental runs have shown consistent increase in fuel cell performance with increasing back pressure. Increasing relative humidity seemed to have increased fuel cell performance with the exception at high current densities and low/medium temperatures, where performance drops due to excess water. Higher temperature was found to reduce the flooding effects of higher RH at high current densities. Fuel cell performance is generally enhanced as cell temperature increases, but there is a decrease in fuel cell performance when temperature increases from 62°C to 74 °C at low pressure and low relative humidity primarily due to dehydration of the membrane at higher temperatures and low humidity levels, causing reduced membrane conductivity and greater ohmic losses. Overall, the greatest influential parameter to PEMFC performance was determined to be the operating temperature. Nevertheless, relative humidity and back pressure still have significant effects on the fuel cell performance as well. It was found that the optimal range of operating conditions is at the higher end of the spectrum for each parameter where the power outputs, shown by the power density curves, was highest at 74°C, 25 psi, and 75% RH. The results will be used as a baseline to evaluate modified membranes to further enhance the fuel cell efficiency in future works.

## 5. Acknowledgements

The authors would like to thank our principal investigator, Dr. Devinder Mahajan, and PhD student, Gozde Ustuner, for their mentorship and technical assistance for this project. We would also

like to thank Dr. Hazem Tawfik for extending his knowledge and experience to us in the field of PEM fuel cell. This research was supported by the Institute of Gas Innovation and Technology (I-GIT) at Stony Brook University.

## 6. References

[1] Zhang, Jianlu, et al. "PEM Fuel Cell Fundamentals." *PEM Fuel Cell Testing and Diagnosis*, 2013, pp. 1–42., doi:10.1016/b978-0-444-53688-4.00001-2.

[2] *Types of Fuel Cells*. Office of Energy & Renewable Energy, www.energy.gov/eere/fuelcells/types-fuel-cells.

[3] Holton, Oliver T., and Joseph W. Stevenson. "The Role of Platinum in Proton Exchange Membrane Fuel Cells." *Platinum Metals Review*, vol. 57, no. 4, 2013, pp. 259–271., doi:10.1595/147106713x671222.

[4] Ozen, Dilek Nur, et al. "Effects of Operation Temperature and Reactant Gas Humidity Levels on Performance of PEM Fuel Cells." *Renewable and Sustainable Energy Reviews*, vol. 59, 30 Jan. 2016, pp. 1298–1306., doi:10.1016/j.rser.2016.01.040.

[5] Wang, L. "A Parametric Study of PEM Fuel Cell Performances." *International Journal of Hydrogen Energy*, vol. 28, no. 11, 8 Mar. 2003, pp. 1263–1272., doi:10.1016/s0360-3199(02)00284-7.

[6] Esfeh, Hamid Kazemi, and Mohd. Kamaruddin Hamid. "Temperature Effect on Proton Exchange Membrane Fuel Cell Performance Part II: Parametric Study." *Energy Procedia*, vol. 61, 2014, pp. 2617–2620., doi:10.1016/j.egypro.2014.12.261.

[7] Zhang, Jianlu, et al. "Effect of Operating Backpressure on PEM Fuel Cell Performance." *ECS Transactions*, vol 19, Jan. 2009, pp. 65-76., doi:10.1149/1.3271363.

# Wildfire Prevention Using an RDP-APP-based Fire Retardant

Andrew Busch [a], Michael Denning [a], Rosario Grasso [a], Jason Zhuang [a]

[a] *Department of Materials Science and Chemical Engineering, Stony Brook University, Stony Brook, NY 11794, USA*

**Abstract**

The abundance of recent wildfires has caused a great need for fire retardants to prevent such disasters. Many fire-retardant mixtures exist, but a broad category of them are too toxic for the environment or are not applicable to our range of use to have wildfire-preventive practicalities. Halogenated flame retardants, usually containing bromine as the halogen, is one of such categories with great potency in preventing fires. It is usually not chemically bound to the coated material, which can lead to leakage to the environment and the potential to bioaccumulate within organisms and ultimately known to have adverse health effects in literature. As such, many studies have turned to safer alternatives such as phosphorus-based flame retardants. These compounds can act in the solid phase, causing the coated material to char to inhibit fueling of the flame or act in the gas phase, producing radicals that cool down the system. This paper highlights a phosphorus-based mixture that acts in the solid and gas phase along with results of several proposed mixtures that performed poorly in flameproofing the samples. The first mixture contained resorcinol (bis)-diphenyl phosphate (RDP), starch, xanthan gum (XG), and water. This produces a thick solution that was difficult to spray and had poor longevity as the samples were partially consumed when burnt after drying. The final mixture contained RDP, ammonium polyphosphate (APP), and (3S)-cis-3,6-dimethyl-1,4-dioxane-2,5-dione lactide monomer (LM). This solution has low viscosity, exhibiting strong flame retardant performance even when dried. Pine branches and bushes were the primary samples for this experiment, and both control samples and coated samples were burned. The samples were additionally analyzed with Fourier-transform infrared spectroscopy (FTIR) to deduce the potential wettability of the mixture onto the surfaces after drying and burnt.

*Keywords:* flame retardant, resorcinol (bis)-diphenyl phosphate (RDP), ammonium polyphosphate, lactide monomer, charring, gas-phase inhibition, cellulose

## 1. Introduction

California has experienced unprecedented wildfire activity in the past decade, with some of the state's largest recorded fires occurring in 2017 and 2018 [2]. Wildfires have the capability to inflict substantial health and economic damage. In the year 2018, 106 people were killed, $32.2 billion were spent on health costs, and an additional $116 billion were lost both directly and indirectly from wildfire damage [9].

Flame retardants (FRs) are a mixture of compounds that can be applied onto combustible materials to render the material fireproof or at minimum hinder the spread of flames if the fire proves to be too powerful. Halogenated flame retardants, which used to see a variety of uses in

everyday life, are composed of reactive elements from Group 17, particularly bromine, as they form potent flame retardants. However, these chemicals are getting phased out in the recent decades due to their ability to bioaccumulate in organisms that breathe within the vicinity of the FR coated objects. The extensive damages of halogenated flame retardants are known to cause adverse health effects such as acting like endocrine disruptors or affecting reproduction and child development [7].

Distinguished under different categories, chemical composition of a flame retardant can range from having high toxicity to mild toxicity, with immense research being funded into developing novel mixtures with low toxicity to the environment.

A major indication of success in a fire retardant acting in the solid-phase, alongside the self-extinguishment of the flames, is the formation of a char layer on the sample. This char layer both blocks combustion reactions and acts as a heat barrier between the flame and the sample, keeping the flame from getting the fuel it needs to continue burning and preventing further degradation of the material [1]. On the other hand, gas-phase mechanisms work by releasing inert gases that dilute the concentration of fuel and oxygen, cooling down the system through endothermic decomposition, and producing compounds that trap flame-propagating radicals [4].

For this experiment, ammonium polyphosphate was used. This particular agent aids in char layer formation by linking phosphates to the ester group. The bonds present in an FTIR analysis show that these agents are active in char layer formation [5]. In addition, the compounds containing phosphorus must be active during sample combustion in order for the char layer to form. These phosphorus-containing compounds are generally required to be volatile for this to occur. [6]

In a study conducted by He et al, it was proposed that wood impregnated with RDP and lactide monomer was able to create a material that was 14x stronger than the control wood and provided the highest flame retardant rating of V-0, performed according to UL-94 Vertical Flame Test standards [3]. Additionally, in a study conducted by Szolnoki et al, the proposition of RDP, a mainly gas-phase reagent, and APP, a solid-phase reagent, having synergistic effects when combined was tested and confirmed [8]. Having ingredients working in two phases appears to enhance the flame retardant mixture. This paves the way to our final successful mixture, which is the combination of RDP, APP, and lactide monomer dissolved in a water solution. Moreover, a previous non-published study conducted by a high school group under the mentorship of our current mentor, Miriam Rafailovich, produced a hydrogel containing RDP, starch, xanthan gum and water that was made for application on human skin to protect against fire. This mixture was believed to also have potential fire retardant properties on plants and as such, the batch was remade and tested for its effectiveness and compared to our final solution.

## 2. Materials and Methods

### *2.1. Preparation of RDP-Starch-XG Mixture*

The mixture of resorcinol (bis)-diphenyl phosphate (RDP) -starch-xanthan gum (XG) was prepared by measuring RDP and starch at a 3:7 ratio and separately measuring RDP and xanthan gum at a 3:7 ratio with a mass balance. The two mixtures were thoroughly mixed within a Thinky Planetary Centrifugal Bubble-free Mixer at 2000 rpm in 15 minute intervals with manual grinding with a mortar and pestle between each session for a total of 3 intervals. 10 g of the RDP/starch mixture and 5 g of the RDP/XG mixture were then added into a beaker and filled to 500 mL with water. Heat was applied through a hot plate at 80 °C until fully dissolved. The final resultant mixture was 10% RDP/starch, 1% RDP/xanthan gum, 89% water. This solution was

thick with a viscosity similar to that of paint and was white and opaque.

### *2.2. Preparation of RDP-APP-LM Mixture*

The mixture of RDP-APP-LM was prepared by using a ratio of 87 wt% distilled water, 5 wt% RDP, 5 wt% APP, and 3% lactide monomer. The lactide monomer and water were mixed into a 600 mL beaker with heat applied through a hot plate until the solid lactide monomer fully dissolved (approximately 60 minutes). The mixture was periodically stirred. After all of the lactide monomer was dissolved, the RDP and APP were added, and the final solution was sonicated for 30 minutes. It should be noted that the initial plan for this mixture consisted of lower concentrations of RDP and APP, but these failed in the burn tests, so the concentration of the active flame retardant ingredients was raised to the values listed above. The overall weight percentages of the original mixture were 1% RDP, 1% APP, and 3% LM. This solution was prepared in the same way as the higher concentration solution. The components of the RDP-APP-LM mixture were completely miscible, producing a low viscosity fluid close to water that was white and almost clear.

### *2.3. Application Method*

Branch samples were cut from potted pine trees and had an average length of 25 cm. Bush samples were cut from potted bushes, and they had an average length of 20 cm. The bushes were burned in the dirt they were purchased in and were cut after burning. The fire retardant mixtures were applied to branch and bush samples by being sprayed with a YATTICH YT-191 paint sprayer until the samples were entirely covered by the mixture.

### *2.4. Burn Tests*

Burn tests were conducted according to ASTM standard E3082-20 on several samples under different conditions: pine branches coated on the same day, coated branches dried overnight, and coated branches dried for several days. Bush samples were burned a day after coating, with one coated sample and one control. The effectiveness of the fire retardant was based on how well it visually resisted the flame and the speed at which the flames self-extinguished after the burner's flame was removed. In addition, after the fire was put out, the samples were inspected to observe if a char layer was formed. Quantitatively, self-extinguishing was defined as the flames on the sample extinguishing within approximately two minutes, with the fire noticeably getting weaker as time passed. Consequently, the samples that needed to be put out with water or were completely consumed were not self-extinguishing.

The mechanisms of the burn tests included lighting the samples in the same spot and holding the flame there for 12 seconds. Once the 12 seconds had elapsed, the flame was removed and the branch was left to burn until it had self-extinguished, been consumed or water was used to put out the fire. Most of these tests were performed within a fume hood, with the larger samples being tested outside. Samples tested outside were placed in an aluminum tray to keep the flames contained. Samples that retarded the flames effectively, were saved to use in the Fourier Transform Infrared Spectroscopy tests.

### *2.5. Fourier Transform Infrared Spectroscopy (FTIR)*

Several pine branch samples, as well as the bush samples, were analyzed under a Thermo Scientific Nicolet 6700 spectrometer to characterize any chemical changes that may occur before and after the burn tests. The samples used were uncoated

pine, coated pine, and coated bush, with both burnt and unburnt sections of each sample for comparison. Samples were ground into powder, using a mortar and pestle. The powder was then placed on the oculus of the FTIR spectrometer. Once placed, the program to operate the FTIR spectrometer was initiated. This process was repeated with all available samples.

## 3. Results

### *3.1. Burn Tests*

Burn tests were performed over the course of several months. Many tests failed which led to new solutions being experimented with. A burn test was considered to have succeeded if the following criteria were met: the flame stopped spreading when the sample was removed from the flame, the sample stopped burning within 10 seconds of removal of the sample from the flame source, and the flames did not spread more than 1 inch from the area in contact with the flame. The original solution of RDP-starch-XG was determined to be inconsistent at protecting the samples, which can be seen in Figure 1, requiring thick coatings of solution and inability to maintain complete fire retardancy after drying.

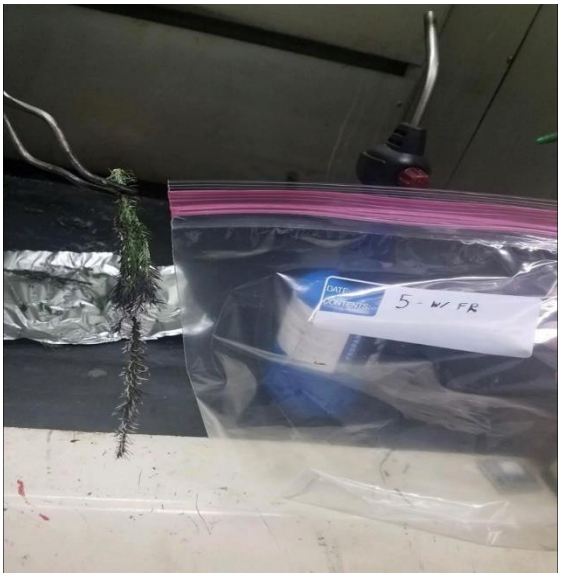


**Figure 1.** Burnt sample coated with RDP/starch/XG solution

Likewise, the burn tests performed with the 1% RDP/1% APP/3% LM mixture proved to be ineffective on branches, although it worked well on cotton balls. However, results differed when using the 5% RDP/5% APP/3% LM mixture. The mixture was first tested on pine branches that had the fire retardant applied only a short time before the test. The test itself involved both the coated sample and a control sample. The control sample was consumed completely. The coated sample, in contrast, self-extinguished almost immediately and formed a small char layer in the place where the flame came in contact with the branch.

The second test using the 5% RDP/5% APP/3% LM mixture was performed on pine branches that had the fire retardant applied several days prior to the actual test, long enough for the fire retardant to dry onto the branch. The test used both the coated branch and a control branch. Figure 2 shows the results of this test where the left side depicts the control branch after the test, having been completely consumed, and the right side depicts the coated sample, which self-extinguished almost immediately and was only lightly charred after being pulled away from the flame. The dried pine branch had a noticeably larger amount of char when compared to the wet sample.

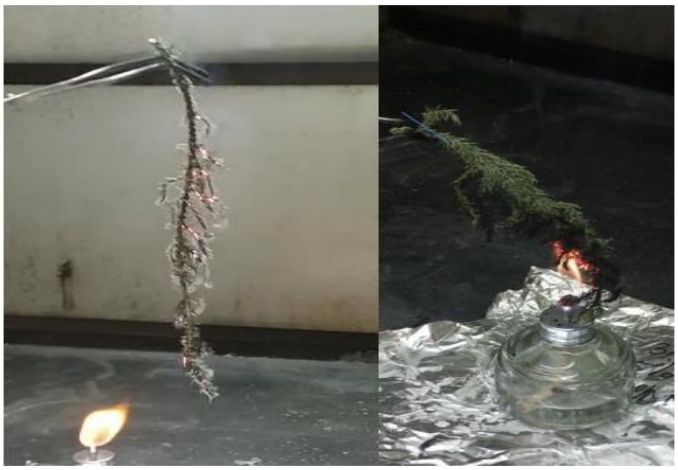

**Figure 2.** Burnt branch sample without FR coat (left) and burnt branch sample with FR coat (right).

The next big test using the 5% RDP/5% APP/3% LM mixture was performed on bushes that had been coated in the fire retardant a few days before the test. This test was performed outside and used both a control and a coated bush sample. The results of this test are depicted in Figure 3. Figure 3(A) depicts the control shortly after the flame was removed. Figure 3(B) depicts the control shortly before water was used to eliminate the flames, keeping the fire under control. Figure 3(C) depicts the coated bush shortly after the flame was removed. Figure 3(D) depicts the coated bush shortly after it self-extinguished. In this test, the control was completely consumed, whereas the bush that was coated in fire retardant self-extinguished after about 10 seconds, leaving only a small char layer on the bush near where the flame was applied and where the flame spread before it self-extinguished.

.

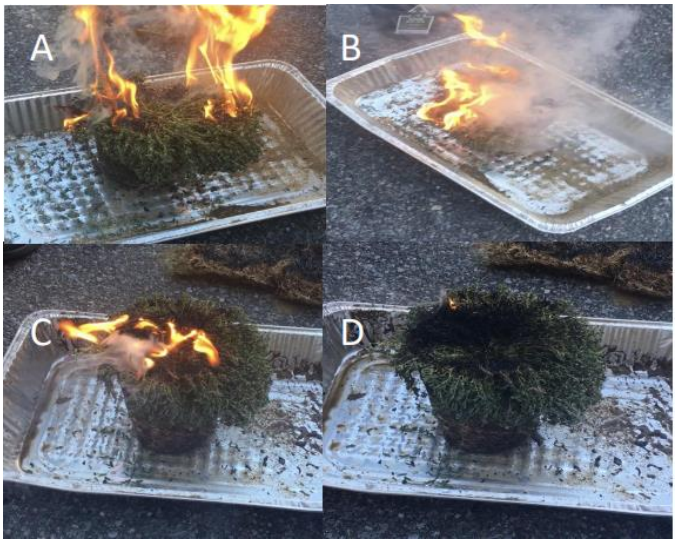


**Figure 3.**
A. Burnt bush sample without fire retardant (control) soon after ignition.
B. Burnt bush sample without fire retardant (control) just before being extinguished with water.
C. Burnt bush sample that was sprayed with fire retardant soon after ignition
D. Burnt bush sample that was sprayed with fire retardant after self-extinguishing.

*3.2. FTIR*

The results from the FTIR can be found on Figure 4. Many leaves are naturally hydrophobic as a result of their chemical structure and composition. As such, wettability is a major factor in ensuring that the mixture can coat the leaves effectively. From the IR spectra of all four samples, there is a strong P-O double bond peak at the 960 $cm^{-1}$ region as a result of the RDP and APP along with an enhanced peak in the 3200-3600 $cm^{-1}$ indicating the potential for hydrogen bonding between the RDP and the cellulose from the plant. From this data, we can deduce that there is strong intermolecular adhesion between the active flame retardant ingredients and the plants. Furthermore, there is a more pronounced spike around 1000-1200 $cm^{-1}$ range present in both the red and cyan lines, which are the burnt samples. These enhanced spikes possibly suggest that more phosphorus-oxygen bonds are formed during combustion and the potential mechanism and structure of the char formation, which could be phosphate ester-based.

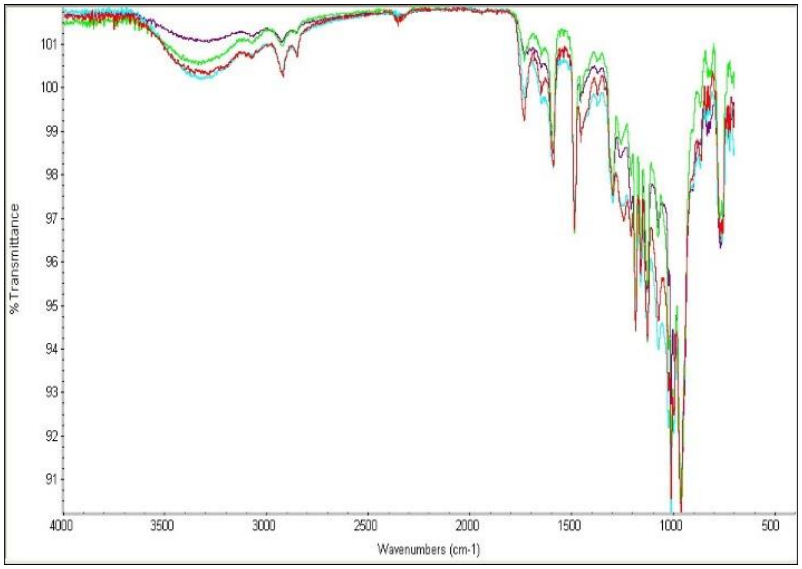


**Figure 4.** FTIR analysis of pre-burn and post-burn FR coated samples.
Red and cyan lines were of burnt samples.
Green and purple were of unburnt samples.

## 4. Discussion

Analysis of the burns tests indicates that at a concentration of 5% APP/5% RDP/3% RDP, the resultant solution is able to most effectively fireproof trees and plants. It was able to self-extinguish the burning plant samples after being dried overnight at ambient room conditions. Unsurprisingly, all of the produced solutions were most effective when the samples were burnt immediately after coating with a FR.

According to the Material Safety Data Sheet (MSDS) for Fyrolflex RDP, the aquatic toxicity of RDP in water for fish is >100 mg/L, or >0.1 g/L. The solution used in this experiment uses 5 grams per 100 mL, or 50 g/L. This means that this particular concentration is too high to be sprayed into waterways, but is still acceptable for use over forests, as potential fire retardant runoff will be significantly diluted to minimally impact aquatic life if it ever reaches a river or pond. In regard to material toxicity, RDP is readily biodegradable, meaning that it poses no threats to soil. Ammonium polyphosphate contains nitrogen and phosphorus, making it an effective fertilizer and is already being used as the primary flame retardant ingredient in the commercial product, Phos-Chek. Lactide is an enhancement additive and considered to be non-toxic and harmless.

From the commercial perspective, the final mixture has potential to be superior to Phos-Chek as they use only APP as the primary flame retarding reagent along with several miscellaneous additives that are trade secrets. The synergistic effect of adding RDP, which acts in the gas-phase, allows for two phases of preventative action together with APP, which acts in the solid-phase, against an impending flame. Additionally, for the manufacturer, the simplicity in making the solution, which only includes one stage of heating and one stage of sonication to dissolve the ingredients makes it viable to produce at the industrial scale and ultimately only includes three ingredients with the fourth being water for dilution.

## 5. Conclusion

In this study, we investigated the effectiveness of two different fire retardant mixtures on preventing the spread of fire on branches and bushes. From our tests, it was determined that the RDP-APP-LM mixture was a successful fire retardant. The concentration was likely higher than necessary for a successful test. As such, lower concentrations of the fire retardant components can be tested to figure out an optimal balance. The RDP-starch-XG solution was not consistent enough to be considered successful for widespread usage, while the RDP-APP-LM solution produced the desired char layer on the burnt samples and meets the environmental standards for an ideal wide-use fire retardant solution.

Future experiments could investigate the effects of the fire retardants on plant growth. Additional thermal tests, such as thermogravimetric analysis (TGA) or finding the Limiting Oxygen Index (LOI), and scanning electron microscope imaging can also be performed to augment the data. Optimization of the ratios in the flame retardant to minimize material waste and finding additives that can further enhance the effectiveness of the flame retardant is always beneficial. Finally, comparative results with the commercial product, Phos-Chek, would provide valuable insight on how well our composition holds up against what is already on the market.

## 6. Acknowledgements

We would like to thank Yiwei Fang for his guidance throughout this project, as well as Dr. Miriam Rafailovich for her mentorship. This research was supported by

the Stony Brook Department of Materials Science and Chemical Engineering.

## 7. References

[1] Gan, W.; Chen, C.; Wang, Z.; Song, J.; Kuang, Y.; He, S.; Mi, R.; Sunderland, P. B.; Hu, L. Dense, Self-formed char layer enables a fire-retardant wood structural material. *Advanced Functional Materials* **2019**, 29.

[2] Goss, M.; Swain, D. L.; Abatzoglou, J. T.; Sarhadi, A.; Kolden, C. A.; Williams, A. P.; Diffenbaugh, N. S.; Climate Change is increasing the likelihood of extreme autumn wildfire conditions across California. *Environmental Research Letters* **2020**, 15.

[3] He, S.; Guo, Y.; Stone, T.; Davis, N.; Kim, D.; Kim, T.; Rafailovich, M. Biodegradable, flame retardant wood-plastic combination via in situ ring-opening polymerization of lactide monomers. *Journal of Wood Science* **2017**, 63, 154-160.

[4] Howell, B. Development Of Additives Possessing Both Solid-Phase And Gas-Phase Flame Retardant Activities. *Polymer Degradation and Stability* **2008**, 93, 2052-2057.

[5] Kishore, K.; Mohandas K. Mechanistic studies on the action of ammonium phosphate on polymer fire retardancy. *Combustion and Flame*, 43 **1981**, pp. 145-153.

[6] Schartel, B. Phosphorus-based Flame Retardancy Mechanisms—Old Hat or a Starting Point for Future Development? Materials **2010**, 3, 4710–4745.

[7] Shaw, S. D.; Blum, A.; Weber, R.; Kannan, K.; Rich, D.; Lucas, D.; Koshland, C. P.; Dobraca, D.; Hanson, S.; Birnbaum, L. S. Halogenated Flame Retardants: Do the Fire Safety Benefits Justify the Risks? *Reviews on Environmental Health* **2010**, 25, 261-305.

[8] Szolnoki, B.; Bocz, K.; Marosi, G.; Toldy, A. Flame Retardancy of Sorbitol Based Bioepoxy via Combined Solid and Gas Phase Action. *Polymers* **2016**, 8, 322.

[9] Wang, D.; Zhu, S.; Kinnon, M. M.; Geng, G.; Zhang, Q.; Zheng, H.; Lei, T.; Shao, S.; Gong, P.; Davis, S. J. Economic footprint of California wildfires in 2018, *Nature Sustainability* **2020**, 4, 250-260.